

ISSN: 2687 - 4539

CHAOS

THEORY AND APPLICATIONS

IN APPLIED SCIENCES AND ENGINEERING



VOLUME 5, ISSUE 2, JULY 2023

AN INTERDISCIPLINARY JOURNAL OF NONLINEAR SCIENCE

CHAOS

THEORY AND APPLICATIONS IN APPLIED SCIENCES AND ENGINEERING

Chaos Theory and Applications (CHTA)

Volume:5- Issue No:2 (July 2023)

<https://dergipark.org.tr/en/pub/chaos/issue/77246>

Honorary Editorial Board

Otto E. ROSSLER, University of Tuebingen, GERMANY, oeross00@yahoo.com

Julien C. SPOTT, University of Wisconsin-Madison, USA, csprott@wisc.edu

Guanrong CHEN, City University of Hong Kong, HONG KONG, eegchen@cityu.edu.hk

José A. Tenreiro MACHADO, Polytechnic Institute of Porto, PORTUGAL, jtm@isep.ipp.pt

Ravi P. AGARWAL, Texas A&M University, USA, Ravi.Agarwal@tamuk.edu

Editor-in-Chief

Akif AKGUL, Hitit University, TURKEY, akifakgul@hitit.edu.tr

Associate Editors

Miguel A. F. SANJUAN, Universidad Rey Juan Carlos, SPAIN, miguel.sanjuan@urjc.es

Chunbiao LI, Nanjing University of Information Science & Technology, CHINA, goontry@126.com

Dumitru BALEANU, Cankaya University, TURKEY, dumitru.baleanu@gmail.com

Yeliz KARACA, University of Massachusetts Chan Medical School, USA, yeliz.karaca@ieee.org

J. M. MUÑOZ PACHECO, Benemérita Universidad Autónoma de Puebla, MEXICO, jesusm.pacheco@correo.buap.mx

Martin BOHNER, Missouri University of Science and Technology, USA, bohner@mst.edu

Nikolay V. KUZNETSOV, Saint Petersburg State University, RUSSIA, n.v.kuznetsov@spbu.ru

Sifeu T. KINGNI, University of Maroua, CAMEROON, stkingni@gmail.com

Fahrettin HORASAN, Kirikkale University, TURKEY, fhorasan@kku.edu.tr

Vinod PATIDAR, Sir Padampat Singhania University, INDIA, vinod.patidar@spsu.ac.in

Hijaz AHMAD, International Telematic University, ITALY, hijaz555@gmail.com

Eyyüp Ensari ŞAHİN, Nigde Omer Halisdemir University, TURKEY, ensarisahin@ohu.edu.tr

Editorial Board Members

Jun MA, Lanzhou University of Technology, CHINA, hyperchaos@lut.edu.cn

Herbert Ho-Ching LU, The University of Western Australia, AUSTRALIA, herbert.iu@uwa.edu.au

Alexander PHELINTSEV, Tambov State Technical University, RUSSIA, pchelintsev.an@yandex.ru

Wesley Joo - Chen THIO, The Ohio State University, USA, wesley.thio@gmail.com

Mustafa Zahid YILDIZ, Sakarya University of Applied Sciences, TURKEY, mustafayildiz@sakarya.edu.tr

Anastasios (Tassos) BOUNTIS, University of Patras, GREECE, anastasios.bountis@nu.edu.kz

Marcelo MESSIAS, São Paulo State University, BRAZIL, marcelo.messias1@unesp.br

Sajad JAFARI, Ton Duc Thang University, VIETNAM, sajadjafari83@gmail.com

Jesús M. SEOANE, Universidad Rey Juan Carlos, SPAIN, jesus.seoane@urjc.es

G. Cigdem YALCIN, Istanbul University, TURKEY, gycalcin@istanbul.edu.tr

Marcelo A. SAVI, Universidade Federal do Rio de Janeiro, BRAZIL, savi@mecanica.coppe.ufrj.br

Christos K. VOLOS, Aristotle University of Thessaloniki, GREECE, volos@physics.auth.gr

Charalampos (Haris) SKOKOS, University of Cape Town, SOUTH AFRICA, haris.skokos@uct.ac.za
Ihsan PEHLIVAN, Sakarya University of Applied Sciences, TURKEY, ipehlivan@sakarya.edu.tr
Olfa BOUBAKER, University of Carthage, TUNUSIA, olfa_insat@yahoo.com
Karthiekeyan RAJAGOPAL, Defence University, ETHIOPIA, rkarthiekeyan@gmail.com
Binoy Krishna ROY, National Institute of Technology Silchar, INDIA, bkr_nits@yahoo.co.in
Jacques KENGNE, Université de Dschang, CAMEROON, kengnemozart@yahoo.fr
Fatih KURUGOLLU, University of Derby, UK, F.Kurugollu@derby.ac.uk
Denis BUTUSOV, Petersburg State Electrotechnical University, RUSSIA, butusovdn@mail.ru
Iqtadar HUSSAIN, Qatar University, QATAR, iqtadarqau@qu.edu.qa
Irene M. MOROZ, University of Oxford, UK, Irene.Moroz@maths.ox.ac.uk
Serdar CICEK, Tarsus University, TURKEY, serdarcicek@gmail.com
Zhouchao WEI, China University of Geosciences, CHINA, weizhouchao@163.com
Qiang LAI, East China Jiaotong University, CHINA, laiqiang87@126.com
Viet-thanh PHAM, Phenikaa University, VIETNAM, pvt3010@gmail.com
Jay Prakash SINGH, Rewa Engineering College, INDIA, jp4ssm@gmail.com
Yilmaz UYAROĞLU, Sakarya University, TURKEY, uyaroglu@sakarya.edu.tr
Shaobo HE, Central South University, CHINA, hshaobo_123@163.com
Esteban Tlelo CUAUTLE, Instituto Nacional de Astrofísica, MEXICO, etlelo@inaoep.mx
Dan-gheorghe DIMITRIU, Alexandru Ioan Cuza University of Iasi, ROMANIA, dimitriu@uaic.ro
Jawad AHMAD, Edinburgh Napier University, UK, jawad.saj@gmail.com
Engin CAN, Sakarya University of Applied Sciences, TURKEY, ecan@subu.edu.tr
Metin VARAN, Sakarya University of Applied Sciences, TURKEY, mvaran@sakarya.edu.tr
Sadaqat Ur REHMAN, Namal Institute, PAKISTAN, engr.sidkhan@gmail.com
Murat TUNA, Kirklareli University, TURKEY, murat.tuna@klu.edu.tr
Orhan Ozgur AYBAR, Piri Reis University, TURKEY, oaybar@pirireis.edu.tr
Mehmet YAVUZ, Necmettin Erbakan University, TURKEY, mehmetyavuz@erbakan.edu.tr

Editorial Advisory Board Members

Ayhan ISTANBULLU, Balıkesir University, TURKEY, ayhanistan@yahoo.com
Ismail KOYUNCU, Afyon Kocatepe University, TURKEY, ismailkoyuncu@aku.edu.tr
Fatih OZKAYNAK, Firat University, TURKEY, ozkaynak@firat.edu.tr
Sezgin KACAR, Sakarya University of Applied Sciences, TURKEY, skacar@subu.edu.tr
Ugur Erkin KOCAMAZ, Bursa Uudag University, TURKEY, ugurkocamaz@gmail.com
Erdinc AVAROĞLU, Mersin University, TURKEY, eavaroglu@mersin.edu.tr
Ali DURDU, Social Sciences University of Ankara, TURKEY, ali.durdu@asbu.edu.tr
Hakan KOR, Hitit University, TURKEY, hakankor@hitit.edu.tr

Language Editors

Muhammed Maruf OZTURK, Suleyman Demirel University, TURKEY, muhammedozturk@sdu.edu.tr
Mustafa KUTLU, Sakarya University of Applied Sciences, TURKEY, mkutlu@subu.edu.tr
Hamid ASADI DERESHGI, Istanbul Arel University, TURKEY, hamidasadi@arel.edu.tr
Emir AVCIOGLU, Hitit University, TURKEY, emiravcioglu@hitit.edu.tr

Technical Coordinator

Muhammed Ali PALA, Sakarya University of Applied Sciences, TURKEY, pala@subu.edu.tr
Murat Erhan CIMEN, Sakarya University of Applied Sciences, TURKEY, muratcimen@sakarya.edu.tr
Harun Emre KIRAN, Hitit University, TURKEY, harunemrekiran@hitit.edu.tr
Berkay EMİN, Hitit University, TURKEY, berkayeminn@gmail.com

CHAOS

THEORY AND APPLICATIONS

IN APPLIED SCIENCES AND ENGINEERING

Chaos Theory and Applications (CHTA)

Volume:5–Issue No:2 (July 2023)

<https://dergipark.org.tr/en/pub/chaos/issue/77246>

Contents

Author(s), Paper Title	Pages
Zeynep KELEŞ, Güray SONUGÜR, Murat ALÇIN. "The Modeling of the Rucklidge Chaotic System with Artificial Neural Networks." (Research Article)	59-64
David GARNER , Shouyan WANG, Ashley RAGHU, Vitor VALENTI, Tipu AZİZ, Alexander GREEN. "Monitoring Blood Pressure Variability via Chaotic Global Metrics using Local Field Potential Oscillations." (Research Article)	65-77
Hüseyin Serdar YALÇINKAYA, Nizamettin BAŞARAN. "Investigation of the Relationship Between Chaos Data and €/ \$ Exchange Rate Index Data with RQA Method." (Research Article)	78-89
Sarker Md Sohel RANA. "Bifurcation Analysis and 0-1 Chaos Test of a Discrete T System." (Research Article)	90-104
Ömer Faruk AKMEŞE, Hüseyin ÇİZMECİ, Selim ÖZDEM, Fikri ÖZDEMİR, Emre DENİZ, Rabia MAZMAN, Murat ERDOĞAN, Esmâ ERDOĞAN. "Prediction of Gender and Age Period from Periorbital Region with VGG16." (Research Article)	105-110
Erdem ERKAN, Yasemin ERKAN. "Ocular Artifact Removal Method Based on the Wavelet and ICA Transform." (Research Article)	111-117
Rameshbabu RAMAR. "Design of a New Chaotic System with Sine Function: Dynamic Analysis and Offset Boosting Control." (Research Article)	118-126
Abdullah GÖKYILDIRIM . " Dynamical Analysis and Electronic Circuit Implementation of Fractional-order Chen System." (Research Article)	127-132

The Modeling of the Rucklidge Chaotic System with Artificial Neural Networks

Zeynep Keles ¹, Guray Sonugur ² and Murat Alcin ³

*Mechatronics Engineering, Faculty of Technology, Afyon Kocatepe University, Afyonkarahisar, Türkiye.

ABSTRACT Chaotic systems are nonlinear systems that show sensitive dependence on initial conditions, and an immeasurably small change in initial value causes an immeasurably large change in the future state of the system. Besides, there is no randomness in chaotic systems and they have an order within themselves. Researchers use chaotic systems in many areas such as mixer systems that can make more homogeneous mixtures, encryption systems that can be used with high security, and Artificial Neural Networks (ANNs) by taking the advantage of the order in this disorder. Differential equations in which chaotic systems are expressed mathematically are solved by numerical solution methods such as Heun, Euler, ODE45, RK4, RK5-Butcher and Dormand-Prince in the literature. In this research, Feed Forward Neural Network (FFNN), Layer Recurrent Neural Network (LRNN) and Cascade Forward Backpropagation Neural Network (CFNN) structures were used to model the Rucklidge chaotic system by making use of the MATLAB R2021A and Neural Network (NN) Toolbox. By comparing the results of different activation functions used in the modeling, the ANN structure that can best model the Rucklidge chaotic system has been determined. The training of the compared ANNs was carried out with the values obtained from the Euler numerical solution method, which can get satisfactory and fast results.

KEYWORDS

Rucklidge
chaotic system
Euler algorithm
Artificial neural network

INTRODUCTION

Chaotic systems were discovered in 1960 by a meteorologist named Edward Norton Lorenz based on the meaningful results he obtained when he changed the initial values in the system he used to make weather forecasts by very small proportions. Lorenz's work proves that chaotic systems change unpredictably within certain limits, and one can only know within which probabilities they may act. After Lorenz's studies, many chaotic systems have been presented to the literature and improvements have been made on the systems by working on chaotic systems (Alcin *et al.* 2019; Avaroğlu *et al.* 2015; Liu *et al.* 2020; Prakash *et al.* 2020; Rajagopal *et al.* 2019; Ramakrishnan *et al.* 2022; Vaidyanathan *et al.* 2018).

Chaotic systems have been widely used in the design of chaotic oscillators (Tuna *et al.* 2019a), True Random Number Generators

(Koyuncu *et al.* 2020a; Tuna *et al.* 2019b) and Pseudo Random Number Generators (Koyuncu *et al.* 2021; Tuna 2020); the modeling using ANNs (Koyuncu *et al.* 2020b), Image Encryption (Boyras *et al.* 2022; Kiran *et al.* 2022; Ullah *et al.* 2022), synchronization.

Lee *et al.* studied the problem of continuous synchronization of a master-slave chaotic system in a sampled data environment by

considering both intermittent coupling and continuous coupling situations. They used the Euler approximation technique to analyze a continuous-time chaotic oscillator containing a nonlinear function. Their experiments with neurons show that using these neurons, ANNs can be implemented rapidly in hardware and the design time can be significantly reduced (Lee *et al.* 2010).

Azzaz *et al.* have presented to the literature a 3 dimension (3D) chaotic system created with automatically switched numerical resolution of new multiple 3D continuous chaotic systems. The designed chaotic system provides complex chaotic attractors and can automatically change their behavior through a chaotic switching rule. At the same time, some complex dynamic behaviors were investigated and analyzed in the study. The originality of the proposed architecture is that it allows to solve the problem

Manuscript received: 11 December 2022,

Revised: 10 March 2023,

Accepted: 23 March 2023.

¹ zeynepkeles.aku@gmail.com

² gsonugur@aku.edu.tr

³ muratalcin@aku.edu.tr (Corresponding Author)

of finite sensitivity due to digital implementation, while providing a good trade-off between high security, performance and hardware resources (low power and cost) (Azzaz et al. 2013).

Çavuşoğlu et al. argue that chaotic systems are an alternative to the standard broad spectrum communication systems in the literature, since they can spread the spectrum of information signals to be transmitted over a wide area, simultaneously encode notification signals and perform these operations with simple and inexpensive chaotic circuit mechanisms. They carried out the signal masking application by considering the Lorenz chaotic system (Cavusoglu 2014).

According to the work of Koyuncu et al. in 2017, the digital implementation of the hardware and the experimental results of the Field Programmable Gate Array (FPGA) circuit show that a promising technique can be applied in efficient embedded cryptographic communication systems. ANN-based Rössler system was created to demonstrate the effectiveness of using neurons in fast realization of ANNs in embedded systems (Koyuncu et al. 2017).

In 2018, Koyuncu and colleagues, who added the numerical modeling of the new 3-D Jerk chaotic system with the fifth-order Runge-Kutta-Butcher algorithm to their work on Matlab, trained a multi-layered feed-forward ANN with the data set obtained from the modeling and analyzed the results obtained from this network. The weights and bias values taken as reference from the numerical solution are used for the design and implementation of the ANN-based 3-D New Jerk Chaotic oscillator on FPGA (Koyuncu et al. 2020b).

In the continuation of 2018, Koyuncu et al. argued that the most basic structure used in chaos-based applications such as cryptology, secure communication, industrial control, ANN, Random Number Generators (RNGs) and image processing is a chaotic oscillator structure that generates the chaotic signal, and they performed an oscillator design that has not been presented in the literature before on FPGA in 32-bit IEEE-754-1985 floating point number standard (Koyuncu et al. 2020b).

In this study, different ANN structures of the Rucklidge Chaotic System and different activation functions in these structures were trained by using them. Success results of each training were compared and ANN structures that could best model the system were presented.

In Section 2, information is given about the Euler method used in this study, and the time series and phase portraits obtained from the solution of the Rucklidge Chaotic System with the Euler method are presented. In Section 3, general information about ANN structures and activation functions is given. In Section 4, the results of different ANN structures and the trainings performed using different activation functions in these structures are presented. In the conclusion part, the success results of the trainings are compared and discussed.

MATERIAL AND METHODS

Rucklidge Chaotic System

The Rucklidge system is a model of a double convection process in which motion is limited to long thin coils that models convection in an applied vertical magnetic field and a smoothly rotating fluid layer (Dong et al. 2021). The second-order nonlinear Rucklidge chaotic system is defined by the following equations.

$$dx/dt = -ax + by - yz \quad (1)$$

$$dy/dt = x \quad (2)$$

$$dz/dt = y^2 - z \quad (3)$$

a and b, which are in the differential equation sets of the Rucklidge chaotic system, are the system parameters. Besides, x, y and z represent the dynamic variables of the system. The system parameters based on this study are $a = 2$ and $b = 6.7$ and the initial conditions are $x_0 = 2, y_0 = 2, z_0 = 2$ and the system shows a chaotic behavior. In addition, since this system is an Ordinary Differential Equation (ODE), this equation can also be solved using MATLAB function libraries.

Euler Method

Euler's method is one of the methods used in the numerical solution of differential equations. Given first-order ODE as follows: $y' = f(x, y)$ and initial values $y(x_0) = y_0$ and trying to solve this equation in the range of x-values $[x_0, x_n]$, our goal is to get a $P = [x_0, x_1, x_2, \dots, x_n]$ is to approximate the value of the $y(x)$ solution at each of the x values. Given $y(x)$, the first value we have to guess is $y(x_1)$. The symbol y' represents the derivative of the function f, where x is the independent variable and y the dependent variable. When expressed by Taylor's theorem:

$$y(x_1) = y(x_0) + y'(x_0)(x_1 - x_0) + \frac{y''(c)}{2}(x_1 - x_0)^2 \quad (4)$$

Since $c \in (x_0, x_1)$, $y'(x_0) = f(x_0, y(x_0))$

$$y(x_1) = y(x_0) + f(x_0, y(x_0))(x_1 - x_0) + \frac{y''(c)}{2}(x_1 - x_0)^2 \quad (5)$$

Here, $\frac{y''(c)}{2}(x_1 - x_0)^2$ is a small error value and may not be taken into account. Then, the Equation 6 is obtained.

$$y(x_1) \approx y(x_0) + f(x_0, y(x_0))(x_1 - x_0) \quad (6)$$

Similarly, for $k = 1, 2, \dots, n - 1$, $y(x_{k+1})$ can be calculated approximately.

$$y(x_{k+1}) \approx y(x_k) + f(x_k, y(x_k))(x_{k+1} - x_k) \quad (7)$$

Here $y(x_k)$ will be known from previous calculations. As with numerical integration methods, it is practical to take the division to consist of sub-intervals of equal width. If we express it in this way, our equation will be as it is expressed in Equation 8.

$$(x_{k+1} - x_k) = \Delta x = \frac{(x_n - x_0)}{n} \quad (8)$$

In the study of numerical methods for differential equations, this quantity is usually denoted by h. Here is our general relationship

$$y(x_{k+1}) \approx y(x_k) + f(x_k, y(x_k))\Delta x \quad (9)$$

If we show our approximations for y, y_0, y_1, \dots, y_n values, x_0, x_1, \dots, x_n , ($y_0 = y(x_0), y_1 \approx y(x_1), etc.$), then approximately $y(x)$ can be calculated iteratively in the P part.

$$y_{k+1} = y_k + f(x_k, y_k)\Delta x \quad (10)$$

The reason why the Euler method is preferred in this study is to obtain good results in a short time by reducing the processing load in modeled ANNs. The time series and the phase portraits obtained from the solution of the Rucklidge chaotic system by Euler's method are shown in Fig.1 and Fig. 2, respectively.

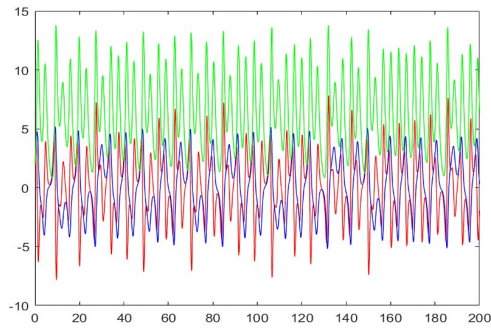


Figure 1 The time series of Rucklidge chaotic system using Euler's numerical solution.

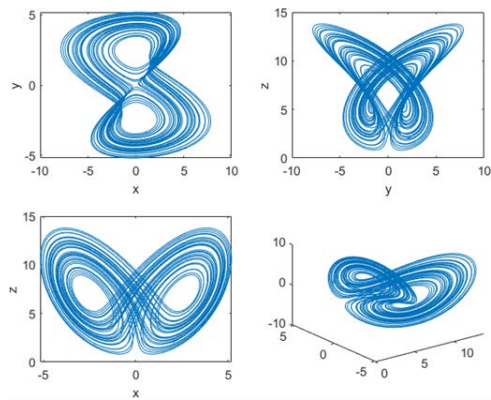


Figure 2 The phase portraits of Rucklidge chaotic system using Euler's numerical solution.

ARTIFICIAL NEURAL NETWORKS (ANNs)

Artificial Neural Network (ANN), is a computer algorithm inspired by the neuron system in order to imitate the process of producing new information with learning in the human brain. It has been developed so that machines can recognize the desired pattern in complex data and generally performs better than other algorithms when recognizing audio, image or video segments. An ANN consists of inputs (X), weights (W), addition function, activation function (Tansig, Purelin, Satlins etc.) and outputs. In ANN modeling, the relationship between Inputs (X) and Outputs (Y) is $Y = f(X) + b$. Here Weight (W) information is used to reduce the error (b).

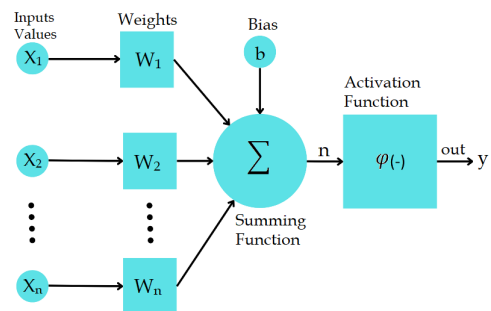


Figure 3 Artificial Neuron Structure

ANNs can also consist of one hidden layer or more than one hidden layer, and different activation functions can be used in these hidden layers. In this project, multi-layer ANNs were studied and single-layer ANNs were excluded. In ANNs, there is no certain rule such as how many hidden layers will be found or how many neurons will be used, zthey are usually created according to the needs of the problem and the best model is tried to be reached by using trial and error method.

In this network structure, the information received from the inputs is transmitted to the hidden layer and has a one-way working principle. The output value is determined by processing the information in the hidden layers and the output layer. ANNs can be created in various structures such as FFNN, LRN, and CFBN. Since MATLAB R2021A program has functions that allow the modeling of the above-mentioned ANNs, the MATLAB R2021A program was used in this study and various variations of the specified ANNs were created and the results were compared.

Feed-Forward Back-propagation Neural Network (FFNN)

In this network structure, the information received from the inputs is transmitted to the hidden layer and has a one-way working principle. The output value is determined by processing the information in the hidden layers and the output layer.

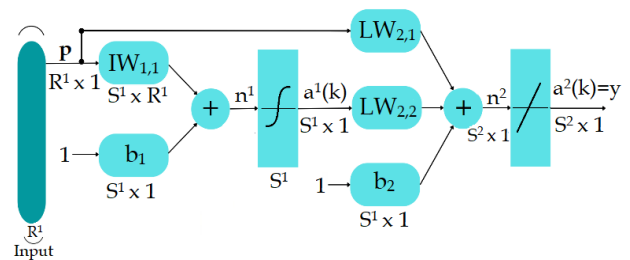


Figure 4 The structure of Feed-Forward Backpropagation Neural Network

Layered-Recurrent Neural Network (LRN)

In Layered-Recurrent Neural Networks, the outputs in the hidden layers and the output layers are also fed back as inputs. Thus, it has a bidirectional working principle. Since there is feedback, this type of ANNs have memory. It is shown in Fig 5

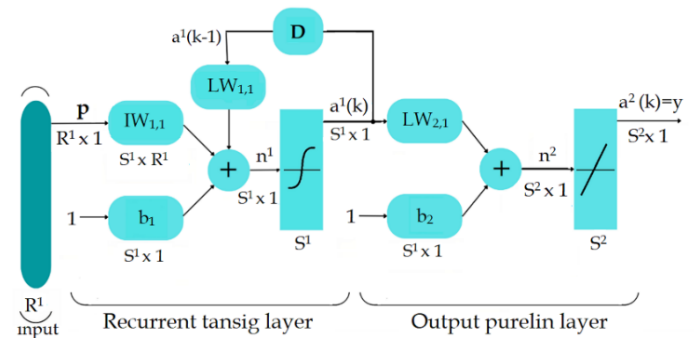


Figure 5 The structure of Layered-Recurrent Neural Network

Cascade Forward Back-propagation Neural Network (CFNN)

Cascade Forward Back-propagation Neural Networks are similar to feed-forward networks. The difference is that the data from the input contains a link to each hidden layer.

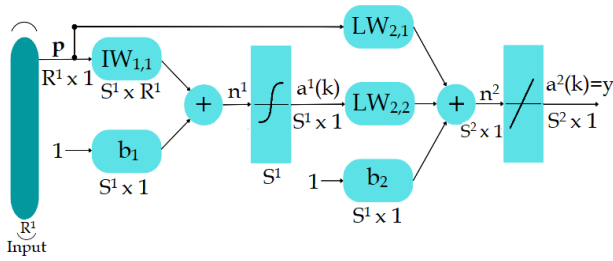


Figure 6 The structure of Cascade Forward Back-propagation Neural Network

In this research, the solution values produced by applying the Euler numerical solution algorithm were given as input to the modeled ANNs, and the ability to model the Rucklidge chaotic system of FFNN, LRN, CFBN were analyzed and the results obtained are presented.

Activation Functions

Activation Functions are used to decide whether neurons will be active or not by processing the information from the summing function. For this reason, it is important to choose an appropriate activation function for the solution of the problem. In this study, the most suitable activation function options for the problem were determined by using different activation functions.

Hyperbolic Tangent Sigmoid Activation Function (tansig)

Hyperbolic tangent sigmoid activation function is an S-shaped activation function that compresses the input values in the infinite space range to the range of -1 and 1 and is expressed mathematically as follows:

$$f(n) = \frac{2}{1 + e^{-2\pi}} - 1 \quad (11)$$

The input-output relationship of the hyperbolic tangent sigmoid transfer function is demonstrated in Fig. 7, where n is the input value and a is the output value for this activation function.

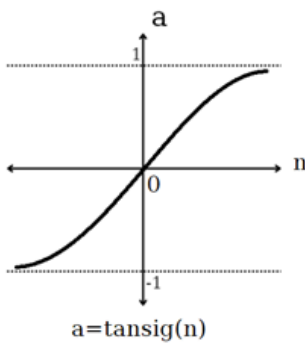


Figure 7 Hyperbolic Tangent Sigmoid Activation Function

Linear Activation Function (Purelin)

Purelin is a linear transfer function used by neural networks and it is mathematically expressed as follows:

$$f(n) = n \quad (12)$$

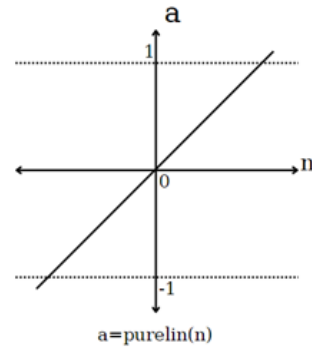


Figure 8 Purelin Activation Function.

Symmetric Saturating Linear Activation Function (Satlins)

The Satlins function is an inverse Z-shaped activation function that transmits to the output in the space interval $[-1, 1]$, gives an output of -1 for values between -1 and infinity, and gives an output of 1 for values between 1 and infinity. This function is mathematically expressed as follows:

$$f(n) = \begin{cases} -1, & n \leq -1 \\ n, & -1 < n < 1 \\ 1, & n \geq 1 \end{cases} \quad (13)$$

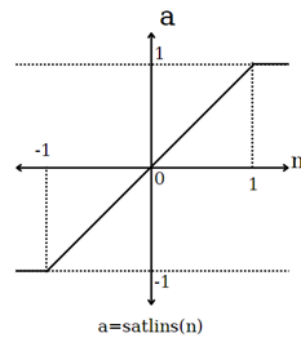


Figure 9 Satlins Activation Function.

In this study, 70% of the $3 \times 10,000$ data obtained by the Euler method of the Rucklidge chaotic system was reserved for training, 15% for validation and 15% for testing, and was used in network training of 14 different ANNs. These ANN structures, Trainlm, Trainbr, Trainscg training functions; Various hidden layer numbers and sequences of Tansig, Purelin, Satlins activation functions have been created on different ANN types such as FFNN, LRN, and CFBN.

■ **Table 1 Training results on modeling the Rucklidge chaotic system with different ANN structures**

No	Network Dimension	Model	Training Function	1 st Activation Function	2 nd Activation Function	3 rd Activation Function	Best Performance
1	8x8x3	CFNN	Trainlm	Tansig	Purelin	Satlines	15.2867
2	8x5x3	CFNN	Trainbr	Tansig	Purelin	Purelin	1.57x10 ⁻¹¹
3	8x5x3	CFNN	Trainlm	Tansig	Purelin	Purelin	4.4519x10 ⁻¹⁵
4	8x3	CFNN	Trainlm	Tansig	Purelin	-	5.13x10 ⁻¹²
5	8x5x3	FFNN	Trainbr	Tansig	Purelin	Satlines	0.0012001
6	5x3	FFNN	Trainlm	Tansig	Purelin	-	6.6562x10 ⁻⁹
7	5x5x3	FFNN	Trainlm	Tansig	Satlines	Purelin	4.3206x10 ⁻⁹
8	5x5x3	FFNN	Trainlm	Tansig	Purelin	Satlines	16.3083
9	8x3	FFNN	Trainlm	Tansig	Purelin	-	2.297x10 ⁻¹¹
10	8x8x3	FFNN	Trainbr	Tansig	Purelin	Satlines	15.2869
11	8x8x3	FFNN	Trainlm	Tansig	Satlines	Purelin	5.4601x10 ⁻⁷
12	8x8x3	FFNN	Trainscg	Tansig	Purelin	Satlines	15.287
13	8x5x3	LRN	Trainlm	Tansig	Purelin	Purelin	3.7906x10 ⁻¹²
14	8x3	LRN	Trainlm	Tansig	Purelin	-	2.94x10 ⁻¹⁰

FINDINGS AND DISCUSSION

In this study, 14 different ANN structures have been trained with respect to different Network Dimension, Training Function, Activation Function. In these ANN structures, there are 2 hidden layers in 8x3 and 5x3, structures. Here, the first and second numbers express the number of neurons in the first and the second hidden layer, respectively. Also, the third refers to the number of neurons in the output layer. Apart from these, there are 1 hidden layers in 8x3 and 5x3 structures. Here, the first and second numbers denote the number of neurons in the hidden layer and output layer, respectively.

Levenberg-Marquardt backpropagation (Trainlm), Bayesian regularization backpropagation (Trainbr) and Scaled conjugate gradient backpropagation (Trainscg) functions have been used as Training Function in these structures. Hyperbolic tangent sigmoid transfer function (Tansig), Linear transfer function (Purelin) and Symmetric saturating linear transfer function (Satlines) functions have been used as Activation Function in these structures.

The results obtained by changing the training and activation functions in different ANN structures of the Rucklidge chaotic system are given in Table 1.

According to the data obtained from Table 1, the ANN structures that can best model the Rucklidge chaotic system are marked with red in the table, and the best result is the CFBN 3rd architecture, which is the 8x5x3 hidden layer Trainlm training function and has the tansig-purelin-purelin activation function order and the best test performance is 4.4519x10⁻¹⁵. The worst test performance is the 8th architecture, an FFNN with 5x5x3 hidden layer Trainlm

training function and Tansig- Purelin- Satlines activation function sequence. Based on this comparison, it can be concluded that FFNN gives better results for the Rucklidge chaotic system among network structures under the same conditions. For this reason, the network structure no. 9, which has fewer neurons and gives satisfactory accuracy values, was preferred in the error analysis.

For 100 iterative values produced by the Rucklidge Chaotic System with the Euler algorithm and 100 iterative values produced by the selected reference number 9 FFNN, Mean Squared Error (MSE), Root Mean Squared Error (RMSE) and Normalized Mean Squared Error (NMSE) values are obtained for 3 outputs, namely X, Y and Z. Here, X, Y and Z represent the produced outputs of the 9th FFNN structure of Rucklidge Chaotic System. The comparison of their outputs for 100 input values is presented in Table 2.

■ **Table 2 MSE, RMSE and NMSE values for 100 produced outputs between Rucklidge Chaotic System with the Euler algorithm and the FFNN network structure no. 9.**

	MSE	RMSE	NMSE
X	3.8965E - 04	1.9740E - 02	1.2065E - 03
Y	2.4895E - 04	1.5778E - 02	1.1937E - 03
Z	6.0393E - 04	2.4575E - 02	1.3986E - 03

CONCLUSION

In this study, the Rucklidge chaotic system, which has not been modeled using ANN before in the literature, has been solved by Euler numerical algorithm and network trainings with different architectures have been carried out with these solution values, making use of the proof of the rapid applicability of ANNs to the hardware implementation in the literature. In this context, network training results were compared by using different ANN structures and different activation functions in these structures, and ANN structures that could best model the Rucklidge Chaotic System were specified. The FFNN with 8×3 , which get more satisfactory results in terms of MSE as 2.297×10^{-11} in Table 1 in a shorter time than the others, was preferred for error analysis. In error analysis, 100 output values generated by Rucklidge Chaotic System with the Euler algorithm and 9th FFNN structure have been used and MSE, RMSE and NMSE values have been obtained. MSE, RMSE and NMSE values for X are $3.8965E-04$, $1.9740E-02$ and $1.2065E-03$, respectively. MSE, RMSE and NMSE values for Y are $2.4895E-04$, $1.5778E-02$ and $1.1937E-03$, respectively. MSE, RMSE and NMSE values for Z are $6.0393E-04$, $2.4575E-02$ and $1.3986E-03$, respectively. In future studies, an application can be made about the hardware implementation of the ANN-based Rucklidge chaotic system.

Conflicts of interest

The authors declare that there is no conflict of interest regarding the publication of this paper.

Availability of data and material

Not applicable.

LITERATURE CITED

- Alcin, M., İ. Koyuncu, M. Tuna, M. Varan, and İ. Pehlivan, 2019 A novel high speed artificial neural network-based chaotic true random number generator on field programmable gate array. *International Journal of Circuit Theory and Applications* **47**: 365–378.
- Avaroğlu, E., T. Tuncer, A. B. Özer, B. Ergen, and M. Türk, 2015 A novel chaos-based post-processing for trng. *Nonlinear Dynamics* **81**: 189–199.
- Azzaz, M. S., C. Tanougast, S. Sadoudi, R. Fellah, and A. Dandache, 2013 A new auto-switched chaotic system and its FPGA implementation **18**: 1792–1804.
- Boyras, O. F., E. Guleryuz, A. Akgul, M. Z. Yildiz, H. E. Kiran, *et al.*, 2022 A novel security and authentication method for infrared medical image with discrete time chaotic systems **267**: 169717.
- Cavusoglu, U., 2014 Surekli zamanli otonom kaotik devre tasarimi ve sinyal gizleme uygulaması. *Gazi Universitesi Muhendislik Mimarlik Fakültesi Dergisi* **29**.
- Dong, C., L. Jia, Q. Jie, and H. Li, 2021 Symbolic encoding of periodic orbits and chaos in the rucklidge system **2021**: e4465151, Publisher: Hindawi.
- Kiran, H. E., A. Akgul, and O. Yildiz, 2022 A new chaos-based lightweight encryption mechanism for microcomputers. In *2022 10th International Symposium on Digital Forensics and Security (IS-DFS)*, pp. 1–5.
- Koyuncu, I., M. Alcin, P. Erdogmus, and M. Tuna, 2020a Artificial neural network-based 4-d hyper-chaotic system on field programmable gate array **8**: 102–108, Number: 2.
- Koyuncu, I., K. Rajagopal, M. Alcin, A. Karthikeyan, M. Tuna, *et al.*, 2021 Control, synchronization with linear quadratic regulator

- method and FFANN-based PRNG application on FPGA of a novel chaotic system **230**: 1915–1931.
- Koyuncu, s., b. Şahin, C. Gloster, and N. K. Sarıtekin, 2017 A neuron library for rapid realization of artificial neural networks on FPGA: A case study of rössler chaotic system **26**: 1750015, Publisher: World Scientific Publishing Co.
- Koyuncu, s., M. Tuna, h. Pehlivan, C. B. Fidan, and M. Alçın, 2020b Design, FPGA implementation and statistical analysis of chaos-ring based dual entropy core true random number generator **102**: 445–456.
- Lee, S.-H., V. Kapila, M. Porfiri, and A. Panda, 2010 Master–slave synchronization of continuously and intermittently coupled sampled-data chaotic oscillators **15**: 4100–4113.
- Liu, J., K. Rajagopal, T. Lei, S. Kaçar, B. Arıcıoğlu, *et al.*, 2020 A novel hypogenetic chaotic jerk system: Modeling, circuit implementation, and its application. *Mathematical Problems in Engineering* **2020**.
- Prakash, P., K. Rajagopal, I. Koyuncu, J. P. Singh, M. Alcin, *et al.*, 2020 A novel simple 4-d hyperchaotic system with a saddle-point index-2 equilibrium point and multistability: design and fpga-based applications. *Circuits, Systems, and Signal Processing* **39**: 4259–4280.
- Rajagopal, K., M. Tuna, A. Karthikeyan, İ. Koyuncu, P. Duraisamy, *et al.*, 2019 Dynamical analysis, sliding mode synchronization of a fractional-order memristor hopfield neural network with parameter uncertainties and its non-fractional-order fpga implementation. *The European Physical Journal Special Topics* **228**: 2065–2080.
- Ramakrishnan, B., M. E. Cimen, A. Akgul, C. Li, K. Rajagopal, *et al.*, 2022 Chaotic oscillations in a fractional-order circuit with a josephson junction resonator and its synchronization using fuzzy sliding mode control. *Mathematical Problems in Engineering* **2022**.
- Tuna, M., 2020 A novel secure chaos-based pseudo random number generator based on ANN-based chaotic and ring oscillator: design and its FPGA implementation **105**: 167–181.
- Tuna, M., M. Alçın, İ. Koyuncu, C. B. Fidan, and İ. Pehlivan, 2019a High speed fpga-based chaotic oscillator design. *Microprocessors and Microsystems* **66**: 72–80.
- Tuna, M., A. Karthikeyan, K. Rajagopal, M. Alcin, and s. Koyuncu, 2019b Hyperjerk multiscroll oscillators with megastability: Analysis, FPGA implementation and a novel ANN-ring-based true random number generator **112**: 152941.
- Ullah, A., A. A. Shah, J. S. Khan, M. Sajjad, W. Boulila, *et al.*, 2022 An efficient lightweight image encryption scheme using multichaos **2022**: e5680357, Publisher: Hindawi.
- Vaidyanathan, S., A. Akgul, S. Kaçar, and U. Çavuşoğlu, 2018 A new 4-d chaotic hyperjerk system, its synchronization, circuit design and applications in rng, image encryption and chaos-based steganography. *The European Physical Journal Plus* **133**: 1–18.

How to cite this article: Keles, Z., Sonugur, G., and Alcin, M. A The Modeling of the Rucklidge Chaotic System with Artificial Neural Networks. *Chaos Theory and Applications*, 5(2), 59–64, 2023.

Monitoring Blood Pressure Variability via Chaotic Global Metrics using Local Field Potential Oscillations

David M. Garner¹, Shouyan Wang², Ashley L.B. Raghu³, Vitor E. Valenti⁴, Tipu Z. Aziz⁵ and Alexander L. Green⁶

¹Cardiorespiratory Research Group, Department of Biological and Medical Sciences, Faculty of Health and Life Sciences, Oxford Brookes University, Headington Campus, Gypsy Lane, Oxford OX3 0BP, United Kingdom, ²Autonomic Nervous System Center, Sao Paulo State University, UNESP, Marilia, SP, Brazil, ³Nuffield Department of Surgical Sciences, Level 6, West Wing, John Radcliffe Hospital, Oxford University, Oxford OX3 9DU, United Kingdom.

ABSTRACT

The intention was to associate blood pressure (BP) variability (BPV) measurements to Local field potentials (LFPs). Thus, assessing how LFPs can co-vary with BPV to permit implantable brain devices (via LFPs) to control output. Elevated BPV is a considerable cardiovascular disease risk factor. Often patients are resistant to pharmacotherapies. An alternative treatment is Deep Brain Stimulation (DBS). Mathematical techniques based on nonlinear dynamics assessed their correlation of BPV chaotic global metrics to LFPs. Chaos Forward Parameter (CFP6) was computed for LFPs, at three electrode depths in the mid-brain and sensory thalamus. Mean, root mean square of the successive differences (RMSSD) and the chaotic global metrics (CFP1 to CFP7) were computed for the BP signal. The right ventroposterolateral (RVPL) nucleus provided a substantial correlation via CFP6 for BP with R-squared up to approximately 79% by means of LFP gamma oscillations. Investigation of BPV via LFPs as a proxy marker might allow therapies to be attuned in a closed-loop system. Whilst all patients were chronic pain patients the chaotic global relationship should be unperturbed. LFPs correlation does not unconditionally predict its causation. There is no certainty DBS in these locations would be therapeutic but can be used as an assessment tool.

KEYWORDS

Chaotic global metrics
Spectral multi-taper method
Blood pressure variability
Local field potentials
Deep brain stimulation

INTRODUCTION

Monitoring deep brain local field potentials (LFPs) can provide wide-ranging information. They show oscillatory behaviour in several frequency bands. The frequency ranges explored here are delta (0.5-4 Hz), theta (4-8 Hz), alpha (8-12 Hz), beta (12-30 Hz), gamma (30-100 Hz) and fast (100-200 Hz) (McAfee 2017). They seed the electroencephalograms (EEGs) that are recorded non-invasively; so are clinically relevant. LFPs reflect the totalled synaptic activity from a local neuronal population within a region

of about 100 micrometres located around the recording electrode. Implanted Deep Brain Stimulation (DBS) electrodes can be used to record their activity from precise areas of the brain. They have been targeted to within sub-millimetric accuracy. Such oscillations are relevant to the neurophysiological and neuropathological aspects of neuropathic pain (Ploner *et al.* 2017), dystonia (Whitmer *et al.* 2013) and Parkinson's disease (Dauer and Przedborski 2003; Lang and Lozano 1998; Stoco-Oliveira *et al.* 2021), amongst others. LFP oscillations in the different frequency ranges are created by distinct mechanisms but, are all related to neural synchrony.

Concentrating on blood pressure (BP) variability (BPV); elevated levels of BP and BPV are interesting because of their correlation with adverse cardiovascular and cerebrovascular events (Appiah *et al.* 2021). The cause of BPV fluctuations versus the LFPs from deep brain areas could provide a therapeutic solution using DBS, pharmacotherapies and so forth. These associations are upheld throughout all age and ethnic groups (Mancia *et al.* 2013). Despite numerous pharmacotherapies, fewer than 50% of

Manuscript received: 15 March 2023,

Revised: 4 May 2023,

Accepted: 5 May 2023.

¹dgarnier@brookes.ac.uk (Corresponding author)

²shouyan@fudan.edu.cn

³ashley.raghu@pmb.ox.ac.uk

⁴vitor.valenti@unesp.br

⁵tipu.aziz@nds.ox.ac.uk

⁶alex.green@nds.ox.ac.uk

hypertensive patients regulate their BP and variabilities effectively. Approximately 0.5% are refractory to treatment, implying uncontrollability despite taking up to five categories of anti-hypertensive medication (Calhoun *et al.* 2014).

Whilst mainstream clinical studies focus on intermittently measured, static BP measurements, BP is not a constant variable. It oscillates, exhibiting short-term (seconds to minutes), mid-term (hours to days) and long-term (between seasons) fluctuations (Parati *et al.* 2018; Webb *et al.* 2021). Likewise, it varies with circadian cycles (Frank *et al.* 1966). Clinical studies have established an independent relationship between both short and long term BPV (Parati *et al.* 2008) to cardiovascular events, regardless of their mean BP levels. These mentioned cardiovascular events and mean BP associations to the chaotic global techniques (discussed later) are expected to initiate from different areas of the midbrain. BPV deviations have been related to target organ damage, such as arterial stiffness (Kim *et al.* 2016; Zhou *et al.* 2018), left ventricular hypertrophy (Mustafa *et al.* 2016), risk of developing diabetic foot ulcers (Palatini 2018) and risk of pre- and post- surgical complications (Henriques *et al.* 2019; Jinadasa *et al.* 2018; Packiasabapathy *et al.* 2020; Rangasamy *et al.* 2020).

Treatment using antihypertensive medications may reduce BPV. Consequently, this is linked with optimal cardiovascular protection (Appiah *et al.* 2021; Corrao *et al.* 2011). This may have implications for stroke (Appiah *et al.* 2021; Rothwell *et al.* 2010), myocardial infarction, heart failure, peripheral artery disease, end-stage renal disease (Parati *et al.* 2012) and explicitly the dynamical diseases (Mackey and Milton 1987). Dynamical diseases are categorized by unexpected aberrations in the qualitative dynamics of physiological processes (Bernardo *et al.* 2014; Chang 2010). This causes irregular dynamics and pathological states. Accordingly, there is an association between the mathematical niche of nonlinear dynamics and complexity theory with clinical medicine (Belair *et al.* 1995).

Initially, we focussed on LFPs in six bandwidths: delta (0.5-4 Hz), theta (4-8 Hz), alpha (8-12 Hz), beta (12-30 Hz), gamma (30-100 Hz) and fast (100-200 Hz) in four anatomical locations and at three electrode depths. We computed the chaotic global metrics (Chaos Forward Parameter, CFP1 to CFP7) that assess the chaotic response and irregularities of datasets, as described by Garner and Ling in 2014 (Garner and Ling 2014). These methods were later advanced to investigate *high spectral* variants and applied them to mathematical inverse problems in 2021 (Garner and Ling 2021). They had already been applied to forward problems (Garner *et al.* 2020a, 2017). We computed the spectral multi-Taper Method (SMTM) for the LFPs. Then, we concurrently logged the mean, root mean square of the successive differences (RMSSD) (Nazaraghaei and Bhat 2020; Schmitt *et al.* 2015) and the non-trivial permutations of three chaotic global metrics of BP. We are assessing its BPV via the somewhat sinusoidally oscillating BP signal. This is analogous to the Duffing (Bonatto *et al.* 2008), Brusselator (Osipov and Poni-zovskaya 2000) and Lorenz (Jeppesen *et al.* 2015) signals in Garner and Ling (Garner and Ling 2021).

BPV fluctuates highly irregularly and conceivably chaotically. So, algorithms that assess this property are appropriate. BPV arises as a result of the cross-talk between several cardiovascular and physiological regulatory systems. These include but are not limited to the baroreceptor reflex, the renin-angiotensin system, the vascular myogenic response and release of nitric oxide from the endothelium (Hocht 2013).

Up until now, the most sophisticated techniques applied to measure BPV have been their mean, standard deviation (Parati *et al.*

2013) and, Detrended Fluctuation Analysis (DFA) (Peng *et al.* 1995) in rats. Nonetheless, whilst DFA has been studied previously (Galhardo *et al.* 2009) it necessitates enforcement on the BP interpeak intervals not the periodic signal described here. Consequently, we later apply *high spectral* Detrended Fluctuation Analysis (*hsDFA*) as CFP5 instead. The chaotic global techniques implemented here (Barreto *et al.* 2014) are anticipated to have elevated responses to those changes than the linear time-domain descriptive statistics and DFA. Here, mean and RMSSD are set as benchmarks.

Some antihypertensive medications such as Calcium Channel Blockers (Rothwell *et al.* 2010; Silke *et al.* 1987) have been demonstrated to be effective in reducing BPV, either as monotherapy, or in combination with other therapies. Since diminishing BPV might avert the risk of cardiovascular mortality (Dolan and O'Brien 2010), under circumstances of refractory hypertension (Bacan *et al.* 2022; Matanes *et al.* 2022), an alternative treatment might be effective. Whilst not without significant risk, a potential substitute is DBS. DBS can effectively lower the absolute mean BP when stimulation is enforced to the ventral columns of the Periaqueductal grey area (PAG) (Green *et al.* 2005). BPV can fluctuate with chronic pain (Spallone 2018). So far, even if we can monitor the BPV levels via the LFPs; it is not inevitably the case that correlation implies causation. DBS in identical regions could be ineffective. Yet, additional pharmacotherapies should be analysed using these chaotic global techniques.

Anatomically, the periaqueductal grey matter (PAG) and rostrally contiguous periventricular grey (PVG) are located in the mid-brain and organized into functionally distinct and opposite columns (Carrive and Bandler 1991). These columns receive afferents from the sympathetic chain (Farkas *et al.* 1998), the rostral raphe (Marcinkiewicz *et al.* 1989), anterior hypothalamus (Cameron *et al.* 1995), thalamus (Krout and Loewy 2000) and cortex (Newman *et al.* 1989). In sequence, the PAG/PVG projects to sympathetic premotor neurons in the hypothalamus, pons and medulla. These projections influence sympathetic outflow that alter cardiovascular output (Farkas *et al.* 1998). Moreover, the PAG/PVG projects to vagal preganglionic neurons (Farkas *et al.* 1997). Assuming that the neurocircuitry of the PAG/PVG and their cross-talk components perform a pivotal role in cardiovascular control the central question of this study is whether the mathematical measures of complexity of this neural activity, in the appropriate region, correlate with BPV. Neuromodulation has the potential to reduce BPV and therefore reduce morbidity associated with this elevated BPV. The necessary neuromodulation may occur in very specific, sub-millimetric locations of the mid-brain and sensory thalamus.

MATERIAL AND METHODS

Twenty-two human patients underwent DBS for neuropathic pain; all were chronic pain. All DBS implantations were performed at the John Radcliffe Hospital, Oxford, United Kingdom. The surgical procedures for the targeting and implantation of DBS electrodes (Model 3387, Medtronic, Minneapolis, MN, United States of America) have been described previously (Bittar *et al.* 2005). All subjects provided their informed written consent and confidentiality rights observed. This study was approved by the Oxford Local Ethics Committee (OxRecB): study number 05 Q1605 47 and conformed to the declaration of Helsinki.

Data Acquisition & Experimental Procedures

The DBS electrodes were temporarily externalized for one week of trial stimulation. This delay was to ascertain if there was a clinical effect prior to implanting the battery. We recorded three bipolar recording signals in four different locations with each electrode situated either in the mid-brain or sensory thalamus (see Figure 1). Electrode contacts are labelled such that '0' is the deepest and '3' the most rostral so that bipolar channel (M23) was the most superficial, (M12) the middle depth and, (M01) the deepest of the recordings. The mid-brain regions were left and right periaqueductal/periventricular grey (LPVG & RPVG respectively). The thalamic areas were right and left ventroposterolateral nucleus (RVPL & LVPL respectively). In subjects with facial pain, their target was slightly medial and termed 'ventroposteromedial' nucleus or 'VPL' for simplicity as there is no structural or functional difference. This sensory thalamic location is ordered somatotopically with face medial and leg lateral (arm in between).

The researchers' ensured synchronisation between the BP signal and LFP measurements. The two outputs were logged simultaneously, aligned on the same clock and displayed online whilst recorded onto a hard disk in Spike2 (Cambridge Electronic Design, United Kingdom).

Datasets were acquired at two sampling frequencies; 4 kHz and 5 kHz. Those at 5 kHz were down-sampled to 4kHz so that all datasets could be manipulated identically. All signals were linearly detrended; the mean of the signal subtracted from the signal itself. The LFPs were bandpass filtered in accordance with delta (0.5-4 Hz), theta (4-8 Hz), alpha (8-12 Hz), beta (12-30 Hz), gamma (30-100 Hz) and fast (100-200 Hz). They were screened so that all values above and below four standard deviations were excluded from the time-series. This had the beneficial effect of removing the most extreme outliers without compromising the signal information. The blood pressure signal was Butterworth notch filtered to eliminate the 50 Hz UK mains noise. The width of the notch was defined by the 49 to 51 Hz frequency interval. This notch filter provided up to 24 dB of attenuation. The LFPs were not filtered in this way since they are only used to compute the sMTM (CFP6) which is contingent on the area between the power spectrum and the baseline, not the signal itself. (See later for elucidation on sMTM & CFP6). Next, all signals were down-sampled to 1 kHz so not too computer processor intensive when further processed. All time-series were 200 seconds long. To achieve correlations with LFP electrode recordings, we logged the concurrent blood pressure signals from the subjects. The LFPs and blood pressure signals had their power spectra computed for supplementary analysis. (See Figure 2).

An elevated level of chaotic global response is correlated with optimal physiological performance (Bernardo *et al.* 2014; De Souza *et al.* 2015). If the level of chaotic global response is lowered this is usually (there are exceptions) associated with the purported dynamical diseases (Belair *et al.* 1995; Mackey and Milton 1987; Pezard *et al.* 1996). These include cardiac arrhythmias and respiratory failures and are potentially fatal. Psychiatric disorders such as Schizophrenia (Bar *et al.* 2010, 2007) and bipolar disorder (Voss *et al.* 2006) are other examples. Chaotic global techniques have previously detected irregularities of the Heart Rate Variability (HRV) in attention deficit hyperactivity disorder (ADHD) (Wajnsztein *et al.* 2016), type 1 diabetes mellitus (T1DM) (De Souza *et al.* 2015; Garner *et al.* 2017) and chronic obstructive pulmonary disease (COPD) (Bernardo *et al.* 2014). The restoration of HRV levels have been confirmed in subjects who have undergone Bariatric surgery (Benjamim *et al.* 2021). These novel chaotic global techniques to

scrutinize BPV have not been applied to blood pressure signals prior to this study.

Signal Processing of Data Regarding further analysis we enforced 100 seconds of time-series. This is since we evaluate half of the 200 second time-series by implementing a sliding window 20 times. Generally, by means of the standard techniques based on nonlinear dynamics such as Shannon Entropy (Shannon 2001) and DFA to assess HRV we require as a minimum of 5 to 20 minutes of time-series (Camm *et al.* 1996). Yet, with the use of chaotic global techniques an ultra-short time series has been proven to be adequate (Garner *et al.* 2019b). The *high spectral* chaotic global metrics are very sensitive and therefore further responsive to chaotic and irregular signals (Garner and Ling 2021).

Each recorded time-series was disconnected into 20 comparable epochs. This attained 20 values. This was to substantiate that if the measures of the linear regression increased. This would indicate that the two samples are more highly correlated. Each epoch incorporated half of the time-series with subsequent epochs being shifted forward by 2.5%. Therefore, the first epoch was measured from 0 to 50%, second from 2.5 to 52.5% and so on until the 20th epoch measured from 50 to 100%. We recorded three bipolar signals (M01 deepest, M12 middle, M23 most superficial) in four different locations of the mid-brain and sensory thalamus. This gave us 20 sections for each bipolar recording signal which were taken per data set.

With regards the LFPs, the sMTM (CFP6) of the 20 phases was taken for each section. This gave 20 values for (M01), 20 values for (M12) and 20 values for (M23) recordings for each of the four regions. The last channel of data to be processed was the blood pressure which was monitored concurrently with the bipolar electrode recordings. We separated this into 20 phases synchronously with the bipolar recordings. For the blood pressure, we computed the mean, RMSSD and the seven non trivial chaotic global metric combinations (CFP1 to CFP7). For a full chaotic global analysis all seven permutations are necessary. It is not sufficient to just equate the signal chaotic global values CFP5, CFP6 and CFP7. This corresponded to 20 for mean, 20 for RMSSD, 20 for CFP1 and so on up to and including 20 for CFP7.

The Multi-Taper Method (MTM) power spectrum provided the foundation for all calculations regarding CFP1 to CFP7 parameters. In this study the parameters for MTM are set at: (i) 1Hz for sampling frequency; (ii) time bandwidth for the DPSS is set to 4; (iii) FFT is the larger of 256 and the next power of two greater than the length of the segment (iv) Thomson's 'adaptive' nonlinear combination method to combine individual spectral estimates.

$$\begin{aligned}
 CFP1 &= \left[n (hsEntropy)^2 + n (sMTM)^2 + (1 - [n (hsDFA)])^2 \right]^{\frac{1}{2}} \\
 CFP2 &= \left[n (hsEntropy)^2 + (1 - [n (hsDFA)])^2 \right]^{\frac{1}{2}} \\
 CFP3 &= \left[n (hsEntropy)^2 + n (sMTM)^2 \right]^{\frac{1}{2}} \\
 CFP4 &= \left[n (sMTM)^2 + (1 - [n (hsDFA)])^2 \right]^{\frac{1}{2}} \\
 CFP5 &= \left[(1 - [n (hsDFA)])^2 \right]^{\frac{1}{2}} \\
 CFP6 &= \left[n (sMTM)^2 \right]^{\frac{1}{2}} \\
 CFP7 &= \left[n (hsEntropy)^2 \right]^{\frac{1}{2}}
 \end{aligned}$$

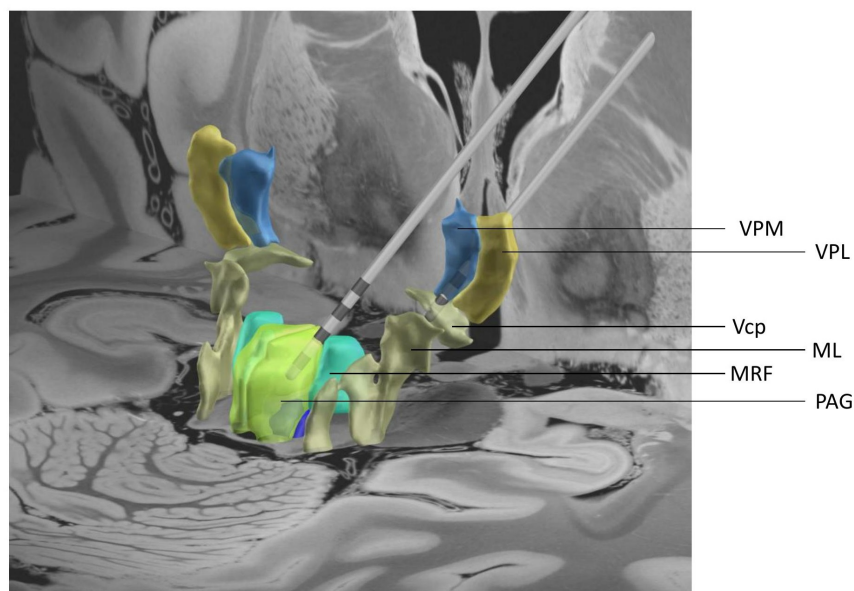


Figure 1 A 3-Dimensional image of the electrode locations. One electrode is PAG/PVG and the other is in the sensory thalamus. These signify a 'mean' position for the cohort described. The coordinates are the mean target (middle 2 contact points) from the mid-commissural point in millimetres (mm). anterior commissure (AC) - posterior commissure (PC) coordinates. PAG array centre : X = 5mm, Y = -16mm, Z = -2mm. Thalamic electrode: X = 16mm, Y = -9mm, Z = 4mm. [PAG = periaqueductal grey, MRF = midbrain reticular formation, ML = medial lemniscus, Vcp = Ventro-caudalis parvocell, VPL = ventral posterolateral, VPM = ventral posteromedial].

Multi-Taper Method Power Spectrum The MTM power spectrum is preferred and implemented as it has been established to statistically outperform several other power spectra (Alkan and Yilmaz 2007; Subasi 2007) when calculating chaotic global metrics (Garner *et al.* 2020a, 2017). MTM (Ghil 1997) is advantageous for spectral estimation and signal reconstruction, of a time-series of a spectrum that may contain broadband and line components. MTM is non-parametric as it does not enforce an a priori, parameter dependent model of the process that generated the time-series under analysis. It lessens the variances of spectral estimates by using a small set of tapers. Data is pre-multiplied by orthogonal tapers created to minimize the spectral leakage on account of the finite length of the time series. A set of independent approximations of the power spectrum is calculated. Functions identified as discrete prolate spheroidal sequences (DPSS) or Slepian sequences (Day *et al.* 2020; Slepian 1978) are a set of functions which optimize these tapers. They are defined as eigenvectors of a Rayleigh-Ritz minimization problem (Gould 1995). For further information consult Thomson (Thomson 1982) or Percival and Walden (Percival and Walden 1993).

Statistical Assessments: Mean, RMSSD & Chaotic Global Variants Firstly, the sMTM (or CFP6) of the pre-processed (linearly detrended and bandpass filtered) LFPs signal was computed. This was for all three depths of electrode (M01, M12, M23), and at the four locations of the mid-brain (LPVG, LVPL, RPVG and RVPL). Secondly, we measured the mean and RMSSD of the blood pressure signal. These were the linear time-domain measurements. They are the simplest to compute, least computer processor intensive and are applied directly to the time-series. These two measurements could then be compared against the chaotic global metrics; key to this investigation. The linear metrics are applied as benchmarks to which all other chaotic global parameters are compared.

The motivation for implementing techniques founded on non-linear dynamics is that they measure the chaos and irregularity of responses in slightly different ways. The initial chaotic global metrics by Garner and Ling (2014) (Garner and Ling 2014) were later distinguished into their *high spectral* variants (Garner and Ling 2021), namely *high spectral* Entropy (*hsEntropy*) and *hsDFA*. These were demonstrated to be more responsive and influential on the basis of a multivariate statistical technique termed Principal Component Analysis (PCA) (Jolliffe 2005). They are functional with ultra-short time-series (Garner *et al.* 2019b). Here the time-series assessed are 100 seconds which is well within the range of the aforementioned study. Thus, the statistical hazards in the application of one are potentially compensated by the others in the CFP1 to CFP7 combinations. This is standard procedure when assessing chaotic global metrics (Bernardo *et al.* 2014; De Souza *et al.* 2015; Garner *et al.* 2022, 2020a, 2017).

hsEntropy is a function of the irregularity of amplitude and frequency of the power spectrums peaks. It is derived by applying Shannon entropy (Shannon 2001) to the MTM (Ghil 1997; Vautard *et al.* 1992) power spectrum. Such variability and introduction of errors from spectral leakage in the time-series and its mathematical relationships over the duration of the datasets are minimised by using the MTM power spectrum, as opposed to that of the Welch (Alkan and Kiymik 2006; Alkan and Yilmaz 2007) power spectrum, which has been applied previously (Bernardo *et al.* 2014; De Souza *et al.* 2015).

DFA (Peng *et al.* 1995) can be implemented to datasets where statistics such as mean, variance and autocorrelation fluctuate with time. To obtain the *hsDFA* the spectral adaptation is computed precisely as for *hsEntropy*. But, this time DFA is enforced onto the MTM power spectrum which has settings identified above. *hsDFA* responds to chaos and irregularities in the reverse way, so we subtract its value from unity; hence we enforce (1-*hsDFA*) when making comparisons.

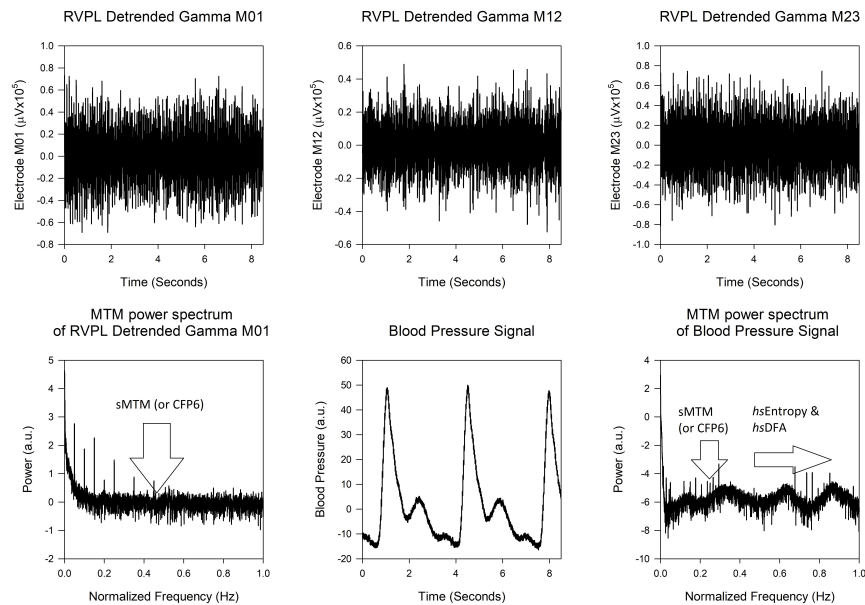


Figure 2 Right ventroposterolateral (RVPL): Three bipolar electrode recording signals; linearly detrended by subtracting the mean of the signal from the signal itself. Then, bandpass filtered in the gamma region (30 to 100 Hz); Electrode M01 (a:upper left) Electrode M12 (b:upper middle) and Electrode M23 (c:upper right) all in units of microVolts. Next, Multi-Taper Method (MTM) Power Spectrum of RVPL linearly detrended Gamma M01 with sMTM (or CFP6) illustrated as the area under the vertical downwards pointing arrow of the power spectrum yet above the baseline (d:lower left) with power in arbitrary units; Blood Pressure signal (e:lower middle) in arbitrary units and time in seconds. MTM power spectrum of the Blood Pressure signal only with sMTM (or CFP6) again illustrated as the area under the vertical arrow of the power spectrum but above the baseline. *High spectral Entropy* (*hsEntropy*) and *high spectral Detrended Fluctuation Analysis* (*hsDFA*) labelled by enforcing Shannon Entropy and DFA onto the power spectrum, respectively as indicated by the horizontal arrow. Power in arbitrary units (f:lower right).

sMTM (CFP6) is the area between the MTM power spectrum and the baseline. MTM of a clean sinusoidal signal in continuous time and infinite length has zero area beneath it (Dirac 1939). For totally uniformly distributed random variables the spectrum is essentially flat. These lesser chaotic and irregular responses offer lower values and totally random data has a value of zero. Within these extremes, chaotic responses are often present with a continuous broadband spectrum. Broadband noise lifts peaks and the trend of the spectrum up and above the baseline, and so chaotic sets have greater values of sMTM. All three chaotic global metrics have identical weightings of unity throughout.

Optimal bandwidth We assessed oscillatory performance using linear regressions during six frequency bands. These frequency ranges were delta (0.5-4 Hz), theta (4-8 Hz), alpha (8-12 Hz), beta (12-30 Hz), gamma (30-100 Hz) and fast (100-200 Hz). (See Figure 3). These regressions were also for the mean of the depth of electrodes (M01, M12, M23) for the four locations of the six aforesaid bandwidths. The gamma region achieved the highest level of linear regression. Therefore, indicating the strongest correlation. Accordingly, we enforce the 30 to 100 Hz bandwidth in all succeeding analysis.

Goodness-of-Fit Assessments: Gamma region (30-100Hz) R-squared (Miles 2005) is referred to as the coefficient of multiple determination for multiple regression. It is a statistical method to assess the proportion of variance in the dependant variable that can be explained by an independent variable. Namely, how good does the data fit the regression model. R-squared is the variation divided by its total variation. R-squared is always between 0 and 1; or as a percentage, 0% and 100%. 0% percent indicates that the model explains none of the variability of the response data about

its mean. Whilst, 100% specifies that the model explains all the variability of the response data about its mean.

Whilst R-squared delivers an insight into the assessment of the statistical model it ought not be relied upon alone. Further procedures need enforcement besides this technique. Moreover, it does not reveal information about the causal connection between the independent and dependent variables.

Residuals (Cook and Weisberg 1982; Gourieroux *et al.* 1987; Pierce and Schafer 1986) are useful for detecting outlying *y* values. They verify the linear regression expectations in regard to the error term in the regression model. High-leverage values have smaller residuals as they often shift the regression line nearer to them. They can detect types of autocorrelations and heteroscedasticity.

Studentized residuals (Gray and Woodall 1994) provide an alternate measure for identifying outliers. They are more discriminative than the Raw, Pearson or Standardized residuals. The notion is to delete certain values in turn; each time refitting the regression model on the remaining (*n*-1) values. So, comparing the observed response values to their fitted values based on the models with the appropriate value deleted. Standardizing these deleted residuals attain the Studentized residuals. They are more effective at detecting outlying *y* values than the other above-mentioned residuals.

We computed the mean of the standard deviation of the *modulus* of the Studentized Residuals and the mean of the maximum of the *modulus* of the Studentized Residuals. There were 20 residuals per regression. Residuals can be positive or negative and would cancel each other out if the mean was applied here just as they are. Consequently, we compute the modulus of the Studentized Residuals which indicates that all the negative values are made positive. Their individual magnitudes are unchanged. Then, since the outliers have greater values; be it the standard deviation or the

maximum; lower values indicate a better fit of regression.

Mean squared error (MSE) (Das *et al.* 2004; Tuchler *et al.* 2002; Wang and Bovik 2009) of an estimator calculates the mean of the squares of the errors. Intrinsically, the mean squared difference between the estimated values and the actual value. MSE is a function of risk, consistent with the expected value of the squared error loss. MSE is always above zero as there is always some randomness or noise inherent in the system. Again, lower values signify a better fit of regression.

RESULTS

The objective is to obtain the highest R-squared. In Figure 3 we are considering the regressions between the LFPs sMTM (or CFP6) and one of the nine metrics; the mean, RMSSD and chaotic global metrics (CFP1 to CFP7) of BP. For each measure of the BP, we have four areas of mid-brain. When the location for the best regressions has been attained, we explore those with a positive y -intercept and a significant slope. These are for the LFPs in the gamma region (30-100Hz) and at three electrode depths (see Table 1). Negative y -intercepts indicate a negative chaotic response which is forbidden by the non-equilibrium laws of thermodynamics (Prigogine 1962). A significant slope is required for an adequate recorded response. A slope of zero would indicate a flat response, hence unresponsive and futile. With regards the standard deviation and maximum of the mean of modulus for the studentized residuals (see Figure 4a & Figure 4b); a lower value indicates a better fitted regression. MSE is also lowest for the optimal regression (see Figure 4c).

LPVG: Left Periventricular Grey

CFP2 (39-59%), CFP4 (31-55%), CFP6 (31-55%) and CFP7 (36-60%) are significant with R-squared between 31% and 60%. The slopes are fairly weak and unresponsive to the electrode depths. CFP2, CFP4, CFP6 and CFP7 all have positive y -intercepts.

CFP1 (19-35%), CFP3 (22-35%) and CFP5 (25-50%) have low values for R-squared. None of the CFPs cited are consistent with positive or negative slopes at all electrode depths.

CFP2, CFP4, CFP6 and CFP7 have very high standard deviation (0.5844-0.8060) and maximum (2.2352-3.1660) Studentized residuals and MSEs (0.0055-0.0083).

RMSSD at M23 has high standard deviation (0.6659-0.7264) and maximum (2.3182-2.6788). Studentized residuals and quite high MSEs (0.0072-0.0091). It is rejected on the basis of a flat response and these low goodness-of-fit values.

So, the regressions for LPVG are confirmed to be lower than most of the other locations.

LVPL: Left Ventroposterolateral

Mean (30-32%) and RMSSD (30-38%) values for R-squared are all low at 30% to 38%. CFP1 (16-32%), CFP2 (28-39%), CFP3 (17-32%) and CFP7 (30-39%) are rejected as they have low R-squared across all electrode depths.

CFP4 (32-47%) and CFP6 (33-47%) have quite low R-squared at 32% to 47%. Yet, CFP5 is rejected as it has negative y -intercepts throughout. Then, CFP4 and CFP6 slopes are fairly weak and so unresponsive to electrode depths. They give a flat response. None of the CFPs are consistent with positive or negative slopes at all electrode depths

CFP4 and CFP6 have very high standard deviation (0.6478-0.7790) and maximum (2.4447-2.9734) Studentized residuals and quite high MSEs (0.0016-0.0114).

Overall for LVPL, the regressions are low and the responses when the regression are high are flat and unresponsive.

RPVG: Right Periventricular Grey

Mean (not RMSSD) gives two robust values for R-squared at M01 (63%) and M12 (55%). CFP1 gives one strong value for R-squared of 54% at electrode location M01. But, the response is relatively flat too.

CFP2 (20-43%) and CFP7 (21-44%) are rejected as they give a low value for R-squared across all electrode depths. There are moderately significant values for R-squared CFP3 (39-58%), CFP4 (46-54%), CFP5 (55% only) and CFP6 (43-52%) are significant for R-squared at 39% to 58%. Yet, the slopes are steeper and are so responsive with respect to all electrode depths. The Mean is consistent in that it has all y -intercepts positive for all electrode depths and very steep negative slopes. None of the CFPs or RMSSD are consistent as they respond with positive or negative slopes throughout at all electrode depths. Mean responds with all negative slopes.

All those with high R-squared CFP3, CFP4, CFP5 and CFP6 have moderately high standard deviation (0.6010-0.6377) and maximum (2.1023-2.4154) Studentized residuals and exceptionally low MSEs (<0.0001-0.0002).

RVPL: Right Ventroposterolateral

RMSSD (not mean) presents robust values for R-squared at M12 (66%) and M23 (56%). Nevertheless, they give low slopes so unresponsive with regards to the electrode depths. The response is flat and so rejected. CFP1 (16-36%) and CFP3 (19-41%) are rejected as they give a low value for R-squared across all electrode depths. CFP5 (39%) for M01 electrode only. All other electrodes gave a y -intercept which was negative and so forbidden.

CFP2 (44-57%), CFP4 (55-80%) and CFP6 (55-79%) gave strong R-squared and all positive y -intercepts throughout. Slopes are consistently negative for CFP2 and constantly positive for CFP4 and CFP6. CFP4 and CFP6 have the best R-squared at 55% to 80% and all slopes are similarly positive at all electrode depths.

CFP2 has high standard deviation (0.6062-0.6418) and maximum (2.2266-2.4339) Studentized residuals and relatively high MSE (0.0002-0.0021) compared to CFP4 and CFP6, later. CFP4 (SD 0.5307-0.6380; Max 2.0569-2.3452) and CFP6 (SD 0.5317-0.6364; Max 2.0349-2.3813) have low Studentized residuals and the low MSEs (0.0002-0.0008).

CFP7 (44-58%) for R-squared consistently negative slopes and always positive y -intercepts. CFP7 (SD 0.6009-0.6320; Max 2.2180-2.4339) have low Studentized residuals and the moderately low MSEs (0.0002-0.0021).

DISCUSSION

The principal aim is to assess the relationship between BPV and LFPs using chaotic global metrics. A relationship between them has clinical implications in that (a) it may allow us to monitor LFPs via DBS electrodes and imply a specific BPV state that may be useful for monitoring or guiding therapy (b) it may imply (if causative) that DBS can be used to clinically alter BPV, and (c) whether DBS confirms suitable pharmacotherapies effective in absence of other designated techniques.

When assessing the regressions of CFP6 for the LFPs versus the mean, RMSSD and CFP1 to CFP7 for the BP signal, we established that the gamma region (30 to 100 Hz) had the highest R-squared which inferred the strongest correlation (See Figure 3).

LPVG and particularly LVPL have the weakest regressions throughout. This is the case for the mean, RMSSD and CFP1 to CFP7. Their slopes are weak and so their responses are flat. Their

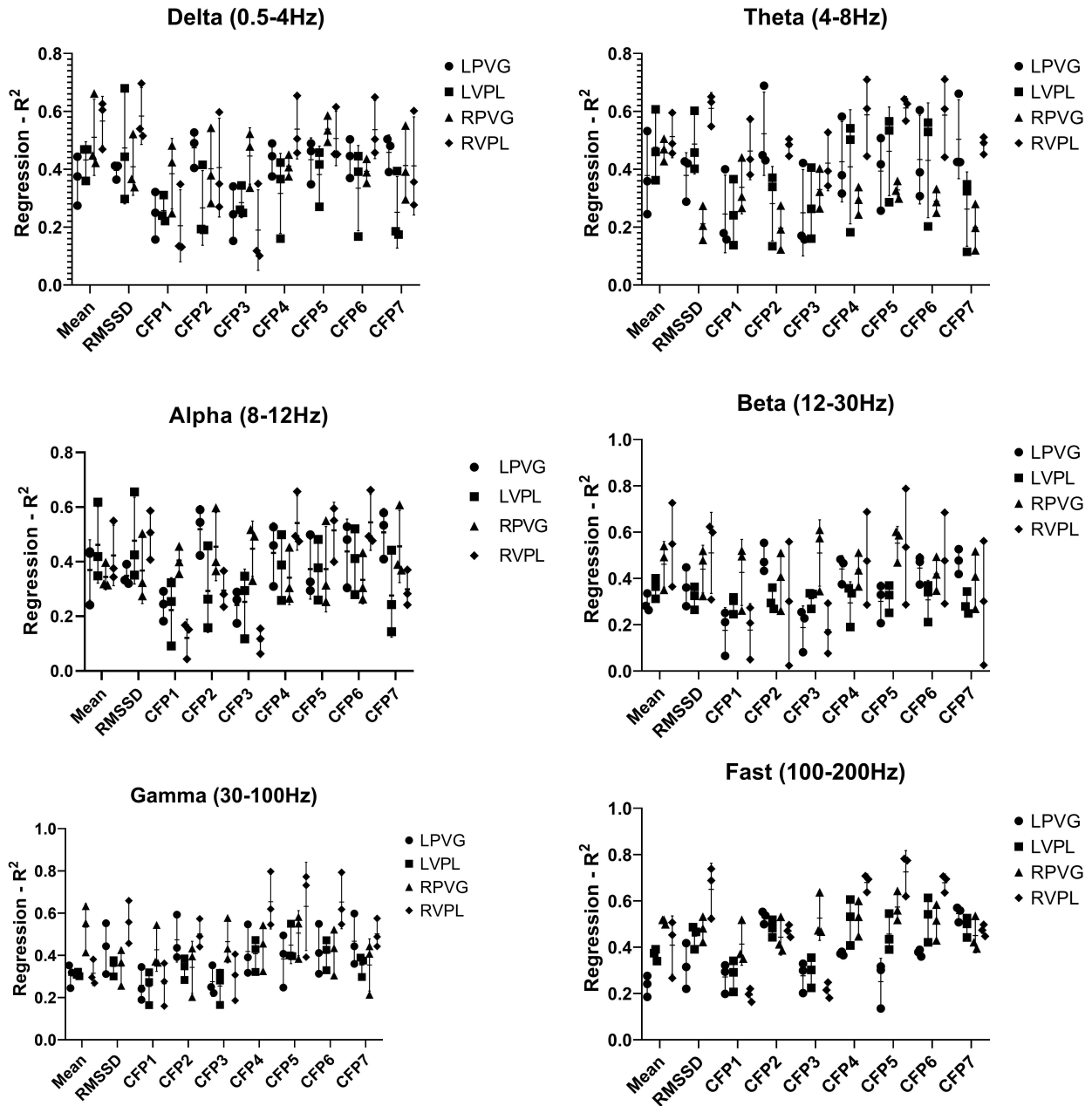


Figure 3 Regressions (R-squared) of sMTM (CFP6) for Local Field Potentials (LFPs) in the delta (0.5-4 Hz), theta (4-8 Hz), alpha (8-12 Hz), beta (12-30 Hz), gamma (30-100 Hz) and fast (100-200 Hz) ranges for the mean of electrodes contacts [M01 (deepest depth), M12 (middle depth) and M23 (most superficial)] at four locations [LPVG (n=5), LVPL (n=5), RPVG (n=8) and RVPL (n=4)] versus the two linear descriptive (Mean & RMSSD) and the seven non-trivial permutations of the three *high spectral* chaotic global variant metrics (*high spectral* Entropy, *high spectral* Detrended Fluctuation Analysis (*hsDFA*) and spectral Multi-Taper Method (sMTM)) of the blood pressure signal (CFP1 to CFP7). The four symbols (circle, square, triangle and diamond) represent the level of R-squared for the LPVG, LVPL, RPVG and RVPL. There are three symbols describing the electrode contacts [M01, M12, M23]. The upper symbol is the maximum R-squared, the lower symbol the minimum R-squared and finally the middle symbol the median R-squared. The horizontal line between the maximum and minimum symbols represents their mean value.

■ **Table 1** Multi-Taper Method (MTM) Power Spectrum: Mean Regressions (R-squared), Mean Slopes and Mean Y-Intercepts of CFP6 for Local Field Potentials (LFPs) in the gamma range (30Hz to 100Hz) for the electrode contacts [M01 (deepest depth), M12 (middle depth) and M23 (most superficial)] versus the two linear descriptive (Mean and RMSSD) and the seven non-trivial permutations of the three *high spectral* chaotic global variant metrics (*high spectral* Entropy, *high spectral* Detrended Fluctuation Analysis and spectral Multi-Taper Method (sMTM)) of blood pressure (CFP1 to CFP7) for recordings from the mid-brain and sensory thalamus locations, namely LPVG (n=5), LVPL (n=5), RPVG (n=8) and RVPL (n=4).

Gamma MTM	CFP (MTM)	Mean R-squared (Regression)			Mean Slope			Mean Y-Intercept		
		M01	M12	M23	M01	M12	M23	M01	M12	M23
LPVG (n=5)	Mean	0.3189	0.3525	0.2449	-0.0720	-0.0155	0.0594	0.0686	0.0124	-0.0583
	RMSSD	0.3116	0.4435	0.5523	0.0000	-0.0003	0.0005	0.0065	0.0067	0.0061
	CFP1	0.2410	0.3450	0.1896	-0.5489	-0.0774	0.3674	1.4466	0.9777	0.5778
	CFP2	0.4359	0.5928	0.3919	-1.0948	0.0418	0.4259	1.8926	0.7694	0.4505
	CFP3	0.2502	0.3531	0.2217	-0.5537	-0.0874	0.4114	1.4481	0.9837	0.5330
	CFP4	0.3177	0.5467	0.3906	-0.1441	-0.2564	0.2839	1.0639	1.1678	0.6629
	CFP5	0.2476	0.4947	0.4075	-1.4032	4.1011	4.0996	1.9084	-3.4154	-3.6113
	CFP6	0.3132	0.5492	0.4113	-0.1534	-0.2787	0.3772	1.0659	1.1819	0.5677
LVPL (n=5)	CFP7	0.4431	0.5979	0.3597	-1.1093	0.0220	0.5019	1.9072	0.7877	0.3801
	Mean	0.3222	0.3082	0.3015	-0.0111	0.0368	-0.0064	0.0055	-0.0329	0.0086
	RMSSD	0.3768	0.3650	0.3001	-0.0001	-0.0009	-0.0005	0.0064	0.0072	0.0067
	CFP1	0.2736	0.3194	0.1644	0.5669	-0.5029	-0.0449	0.3576	1.3904	0.9170
	CFP2	0.3481	0.3855	0.2834	1.1999	-0.9483	0.0159	-0.3325	1.7033	0.7151
	CFP3	0.2812	0.3173	0.1651	0.5730	-0.5084	-0.0493	0.3482	1.3935	0.9184
	CFP4	0.3215	0.4722	0.4298	0.0855	-0.3483	-0.1469	0.8465	1.2939	1.0808
	CFP5	0.3995	0.5500	0.3962	3.1834	7.6659	3.0033	-2.3982	-7.0839	-2.4554
RPVG (n=8)	CFP6	0.3296	0.4715	0.4263	0.0900	-0.3570	-0.1575	0.8347	1.2972	1.0850
	CFP7	0.3757	0.3891	0.2976	1.2406	-0.9806	0.0075	-0.3724	1.7352	0.7213
	Mean	0.6332	0.5532	0.4144	-17.3424	-3.4684	-35.1832	16.2967	2.5193	34.2220
	RMSSD	0.4248	0.2557	0.3664	-0.1180	2.0073	-1.7408	0.8548	-1.2691	2.4785
	CFP1	0.5438	0.3699	0.3650	0.1079	-2.5581	1.7963	0.8440	3.5045	-0.8619
	CFP2	0.4326	0.2024	0.3948	-0.2817	-24.9221	15.1715	1.1101	25.7363	-14.3729
	CFP3	0.5773	0.3853	0.4315	0.1508	-4.1633	2.8160	0.7966	5.1043	-1.8856
	CFP4	0.5428	0.3251	0.4554	0.0834	20.3526	-14.4953	0.8200	-19.4365	15.3966
RVPL (n=4)	CFP5	0.5818	0.3833	0.5508	4.0876	68.1583	-30.3918	-3.3819	-67.4462	31.1401
	CFP6	0.5216	0.3043	0.4340	0.1343	18.7723	-13.5547	0.7770	-17.8495	14.4640
	CFP7	0.4429	0.2134	0.4072	-0.2136	-28.9885	17.4886	1.0320	29.7911	-16.6985
	Mean	0.2692	0.3813	0.2958	11.3574	-3.2315	-1.4466	-11.0458	3.0903	1.5040
	RMSSD	0.4570	0.6589	0.5576	-0.1824	0.1025	0.0459	1.0476	0.7686	0.8224
	CFP1	0.3622	0.1597	0.2765	-0.1647	0.0466	0.0496	1.1374	0.9384	0.9325
	CFP2	0.4902	0.4407	0.5731	-0.7910	-0.1683	-0.3987	1.7010	1.1084	1.3244
	CFP3	0.4055	0.1861	0.3069	-0.1954	0.0284	0.0188	1.1657	0.9546	0.9610
CFP4	0.5458	0.6197	0.7973	0.4875	0.2878	0.5411	0.4723	0.6671	0.4227	
CFP5	0.3918	0.7319	0.7723	-0.1385	2.1030	3.3639	0.5431	-1.7147	-2.9434	
CFP6	0.5474	0.6179	0.7930	0.4483	0.2641	0.5013	0.5140	0.6938	0.4651	
CFP7	0.4880	0.4426	0.5750	-0.8580	-0.2064	-0.4636	1.7627	1.1422	1.3842	

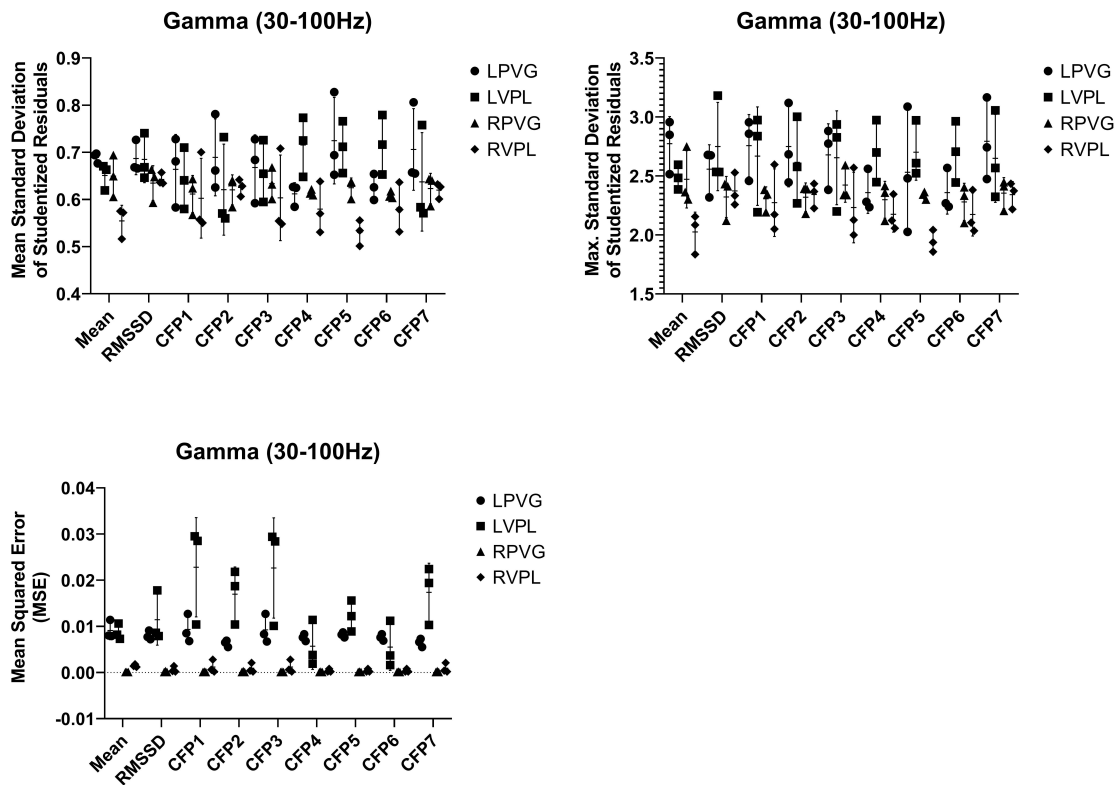


Figure 4 (a: upper left) Mean of the Standard Deviation of the modulus of the Studentized Residuals (b: upper right) Mean of the Maximum of the modulus of the Studentized Residuals (c: lower left) Mean of the mean squared error (MSE); of spectral Multi-Taper Method (or CFP6) for LFPs in the gamma range (30 to 100Hz) for the electrode contacts at three depths [M01 (deepest), M12 (middle) and M23 (superficial)] versus the two linear descriptive (Mean & RMSSD) and the seven non-trivial permutations of the three *high spectral* chaotic global variant metrics (*hsEntropy*, *hsDFA* and *sMTM*) of blood pressure (CFP1 to CFP7) for recordings in the four areas, specifically LPVG (n=5), LVPL (n=5), RPVG (n=8) and RVPL (n=4). Again as with Figure 3. The four symbols (circle, square, triangle and diamond) represent appropriate values for the LPVG, LVPL, RPVG and RVPL. There are three symbols describing the electrode contacts [M01, M12, M23]. The upper symbol is the maximum, the lower symbol the minimum and finally the middle symbol the median. The horizontal line between the maximum and minimum symbols represents their mean value.

slopes are inconsistent throughout for both locations. Some slopes are negative, some positive. Their slopes are such that when the electrodes are surgically implanted for monitoring the different depths they give radically different results. Their goodness-of-fits via their Studentized residuals and MSE are poor. These highlight yet again that the regressions are less significant. The points form an excess of high residuals signifying that the model explains little of the variability of the response data around its mean. For LVPL, CFP5 is totally rejected as all y-intercepts are negative.

RVPL and RPVG are better sites for monitoring. They give higher values for their regressions throughout equated to LPVG and LVPL. With regards RPVG for CFP1 to CFP7 and RMSSD they are unreliable as they respond with positive or negative slopes at all electrode depths. Yet, their mean is dependable with all negative slopes. The slopes are steeper and are so are highly responsive regarding electrode depths. The mean is consistent in that it has all y-intercepts positive at all electrode depths. The mean, however, only measures the datas' magnitude and does not assess its sequence as with the nonlinear dynamic techniques. Therefore, it should be judged with caution.

For RVPL, RMSSD has high R-squared values at electrode locations M12 (66%) and M23 (56%) but at these locations they have low slopes; so unresponsive and flat. Slopes are moderately steep and consistently negative for CFP2. They are continually positive and quite steep for CFP4 and CFP6. As their slopes are consistent they are good locations to position electrodes since surgical precision is less critical. CFP2, CFP4 and CFP6 give positive values for their y-intercepts throughout. Their regressions are CFP4 (55-80%) and CFP6 (55-79%). These are the most significant regressions of all of the locations. But, RVPL could be unduly significant as a result of its low sample size.

We have demonstrated that the most statistically robust and significant combinations are CFP4 and CFP6 for RVPL with regressions significant at the level of about 55% to 80%. CFP1 and CFP3 are usually the most robust and statistically significant when applied to forward problems (Garner *et al.* 2019b, 2017; Wajnsztein *et al.* 2016). Yet, CFP6 is favoured as it has been confirmed to be significant with forward and mathematical inverse problems, in particular, as in Garner and Ling (2014) (Garner and Ling 2014). Moreover, in 2021 with *high spectral* variants (Garner and Ling 2021). CFP6 is simple to implement and computationally fast.

Green *et al.* in 2005 (Green *et al.* 2005) revealed that stimulation in the rostral PVG/PAG can increase or decrease levels of arterial blood pressure. This effect is contingent on the ventral/dorsal location of the electrode. In this study, we revealed that with recordings of RVPL, decreases in the blood pressure signal complexity can be monitored in a similar manner. It is important to realize the study by Green *et al.* (Green *et al.* 2005) was considering BP whereas here we are assessing BPV. Interestingly the neuromodulation of BP and BPV are in different positions as revealed here. BPV neuromodulation is unique and so different LFPs are measured in dissimilar locations.

During some of the recorded LFPs time-series there were some locations in a few of the subjects which experienced short sections of DBS. These stimulations were not elongated enough to be measured for irregularities and chaotic responses. They are, nevertheless, not overlooked in the analysis. There were 20 epochs in the analysis which had a window of half of the entire time-series. This sliding window progresses from start to finish and for some zones or a few subjects this would have included short areas of DBS stimulation. These affect the LFPs recordings at three depths of electrode in the four areas of the brain. These were not excluded

as their effects would be minimal. They cannot be spliced online which is the proposed format of the analysis. The LFPs would be principally resting but the zones of stimulation would improve the significance of the regressions by extending the statistical range of the LFPs. Each regression was computed from 20 points from the 20 sections. Next, a mean regression was computed for all the four locations. The number of subjects in the mean regression varied from four (RVPL) to eight (RPVG). The mean regression was used in the correlation of LFPs with BPV from the mean, RMSSD and chaotic global metrics.

It is important to understand that the human subjects in this study were all chronic pain patients. BP and BPV responses may be altered by chronic pain. Correspondingly, we should consider lateralisation (Hodgetts and Hausmann 2022; Hwang *et al.* 2022; Srinivasan *et al.* 2022). This is the inclination of some neural functions or cognitive processes to be located in one hemisphere of the brain instead of the other. There is lateralisation in BPV autonomic control.

If subjects experience Hypertension refractory to current pharmacotherapies, DBS may be a potential alternative treatment. DBS is a surgical procedure and as such cannot be performed without substantial risk and unanticipated difficulties. Whilst DBS of the PAG has been enforced to treat refractory Hypertension both in the context of pain (Patel *et al.* 2011) and without (O'Callaghan *et al.* 2017), its lack of use for this indication since our original conclusions in 2005 are possibly on account of this balance of risks. A potential correlation between the LFPs and BPV would be advantageous as it could be useful for developing adaptive forms of DBS (or novel pharmacotherapies) to reduce BPV using closed-loop feedback. The chaotic global sMTM (CFP6) could be a statistical marker.

Additionally, it would be wise to consider alternative neuromodulator therapies such as carotid body stimulation or renal sympathetic nerve ablation as they have lower risk. Both therapies failed phase three trials (Simplicity and BAROSTIM NEO Hypertension Pivotal Study ClinicalTrials.gov) for refractory Hypertension, but the latter is currently undergoing reassessment using specific patient cohorts and updated technology and techniques (SPYRAL HTN-ON MED Study ClinicalTrials.gov).

Further work could be commenced. For instance, the parameters for the MTM spectra could be adjusted. MTM was predominantly chosen as it has less spectral leakage. Yet, the manipulation of DPSS and Thomson's Multi-Taper settings have been repeatedly shown to be trivial (Garner *et al.* 2019a). Other methods of monitoring might be better. Levels of chaotic response could be assessed alternatively by the fractal dimensions of Higuchi (Garner *et al.* 2018; Nogueira *et al.* 2017) or Katz (Garner *et al.* 2018). Approximate (Garner *et al.* 2021b; Pincus 1995) and Sample (Richman and Moorman 2000) entropies could be computed. However, the latter two are excessively reliant on their embedding dimensions and tolerances. These cannot be attained in any systematic way which maintains them undependable (Garner *et al.* 2021b,a, 2020b). Also, they are usually enforced on the inter-beat intervals rather than just the oscillating signal as with chaotic global metrics.

CONCLUSION

We revealed correlation (R-squared: up to 79%) in the RVPL site for all electrode depths (deep to superficial) between the LFPs gamma oscillations (30 to 100 Hz) and BPV for CFP6. This may have clinical uses. Perhaps, therapy could be achieved pharmacologically, surgically or otherwise by monitoring BPV using LFPs and making adjustments. Yet, correlation of the LFPs does not

inevitably predict its causation. There is no certainty that DBS in these areas will be therapeutic. They have only been confirmed for monitoring purposes with BPV. Further studies are suggested to ascertain if DBS or novel therapies do reduce BPV and lessen cardiovascular complications, potential morbidity and accordingly mortality.

Conflicts of interest

The authors declare that there is no conflict of interest regarding the publication of this paper.

Availability of data and material

Matlab code used in the study remains confidential as potential intellectual property.

Acknowledgements

This study was supported by the National Institute of Health (NIHR) Oxford Biomedical Research Centre.

LITERATURE CITED

- Alkan, A. and M. K. Kiyimik, 2006 Comparison of AR and Welch methods in epileptic seizure detection. *J Med Syst* **30**: 413–9.
- Alkan, A. and A. S. Yilmaz, 2007 Frequency domain analysis of power system transients using Welch and Yule-Walker AR methods. *Energy conversion and management* **48**: 2129–2135.
- Appiah, K. O. B., M. Nath, L. Manning, W. J. Davison, S. Mazzucco, *et al.*, 2021 Increasing blood pressure variability predicts poor functional outcome following acute stroke. *Journal of Stroke and Cerebrovascular Diseases* **30**.
- Bacan, G., A. Ribeiro-Silva, V. A. Oliveira, C. R. Cardoso, and G. F. Salles, 2022 Refractory hypertension: a narrative systematic review with emphasis on prognosis. *Current Hypertension Reports* **24**: 95–106.
- Bar, K. J., S. Berger, M. Metzner, M. K. Boettger, S. Schulz, *et al.*, 2010 Autonomic dysfunction in unaffected first-degree relatives of patients suffering from schizophrenia. *Schizophr Bull* **36**: 1050–8.
- Bar, K. J., M. K. Boettger, M. Koschke, S. Schulz, P. Chokka, *et al.*, 2007 Non-linear complexity measures of heart rate variability in acute schizophrenia. *Clin Neurophysiol* **118**: 2009–15.
- Barreto, G. S., F. M. Vanderlei, L. C. M. Vanderlei, and D. M. Garner, 2014 Risk appraisal by novel chaotic globals to HRV in subjects with malnutrition. *Journal of Human Growth and Development* **24**: 243–248.
- Belair, J., L. Glass, U. an der Heiden, and J. Milton, 1995 Dynamical disease: identification, temporal aspects and treatment strategies of human illness. *Chaos: An Interdisciplinary Journal of Nonlinear Science* **5**: 1–7.
- Benjamim, C. J. R., Y. Mota de M. Pontes, F. Welington de Sousa Junior, A. A. Porto, C. R. Bueno Junior, *et al.*, 2021 Does bariatric surgery improve cardiac autonomic modulation assessed by heart rate variability: a systematic review. *Surgery for Obesity and Related Diseases*.
- Bernardo, A. F., L. C. Vanderlei, and D. M. Garner, 2014 HRV analysis: A clinical and diagnostic tool in chronic obstructive pulmonary disease. *Int Sch Res Notices* **2014**: 673232.
- Bittar, R. G., I. Kar-Purkayastha, S. L. Owen, R. E. Bear, A. Green, *et al.*, 2005 Deep brain stimulation for pain relief: a meta-analysis. *J Clin Neurosci* **12**: 515–9.
- Bonatto, C., J. Gallas, and Y. Ueda, 2008 Chaotic phase similarities and recurrences in a damped-driven duffing oscillator. *Phys.Rev.E.Stat.Nonlin.Soft.Matter Phys.* **77**: 026217.
- Calhoun, D. A., J. N. Booth III, S. Oparil, M. R. Irvin, D. Shimbo, *et al.*, 2014 Refractory hypertension: determination of prevalence, risk factors, and comorbidities in a large, population-based cohort. *Hypertension* **63**: 451–458.
- Cameron, A. A., I. A. Khan, K. N. Westlund, K. D. Cliffer, and W. D. Willis, 1995 The efferent projections of the periaqueductal gray in the rat: A phaseolus vulgaris-leucoagglutinin study. I. Ascending projections. *Journal of Comparative Neurology* **351**: 568–584.
- Camm, A., M. Malik, J. Bigger, G. Breithardt, S. Cerutti, *et al.*, 1996 Heart rate variability: standards of measurement, physiological interpretation and clinical use. task force of the european society of cardiology and the north american society of pacing and electrophysiology. *Circulation* **93**: 1043–1065.
- Carrive, P. and R. Bandler, 1991 Viscerotopic organization of neurons subserving hypotensive reactions within the midbrain periaqueductal grey: a correlative functional and anatomical study. *Brain research* **541**: 206–215.
- Chang, S., 2010 Physiological rhythms, dynamical diseases and acupuncture. *Chin J Physiol* **53**: 77–90.
- Cook, R. D. and S. Weisberg, 1982 *Residuals and influence in regression*. New York: Chapman and Hall.
- Corrao, G., A. Parodi, F. Nicotra, A. Zambon, L. Merlino, *et al.*, 2011 Better compliance to antihypertensive medications reduces cardiovascular risk. *Journal of hypertension* **29**: 610–618.
- Das, K., J. Jiang, and J. Rao, 2004 Mean squared error of empirical predictor. *The Annals of Statistics* **32**: 818–840.
- Dauer, W. and S. Przedborski, 2003 Parkinson's disease: mechanisms and models. *Neuron* **39**: 889–909.
- Day, B. P., A. Evers, and D. E. Hack, 2020 Multipath suppression for continuous wave radar via slepian sequences. *IEEE Transactions on Signal Processing* **68**: 548–557.
- De Souza, N. M., L. C. M. Vanderlei, and D. M. Garner, 2015 Risk evaluation of diabetes mellitus by relation of chaotic globals to HRV. *Complexity* **20**: 84–92.
- Dirac, P., 1939 New notation for quantum mechanics. *Proceedings of the Cambridge Philosophical Society* **35**: 416.
- Dolan, E. and E. O'Brien, 2010 Blood pressure variability clarity for clinical practice. *Hypertension* **56**: 179–181.
- Farkas, E., A. S. Jansen, and A. D. Loewy, 1997 Periaqueductal gray matter projection to vagal preganglionic neurons and the nucleus tractus solitarius. *Brain research* **764**: 257–261.
- Farkas, E., A. S. Jansen, and A. D. Loewy, 1998 Periaqueductal gray matter input to cardiac-related sympathetic premotor neurons. *Brain research* **792**: 179–192.
- Frank, G., F. Halberg, R. Harner, J. Matthews, E. Johnson, *et al.*, 1966 Circadian periodicity, adrenal corticosteroids, and the eeg of normal man. *J.Psychiatr.Res.* **4**: 73–86.
- Galhardo, C., T. Penna, M. A. de Menezes, and P. Soares, 2009 Detrended fluctuation analysis of a systolic blood pressure control loop. *New Journal of Physics* **11**: 103005.
- Garner, D., M. Alves, B. da Silva, L. de Alcantara Sousa, and V. Valenti, 2020a Chaotic global analysis of heart rate variability following power spectral adjustments during exposure to traffic noise in healthy adult women. *Russ J Cardiol* **25**: 3739.
- Garner, D., A. Bernardo, and L. Vanderlei, 2021a HRV analysis: Unpredictability of approximate entropy in chronic obstructive pulmonary disease. *Series Cardiol Res* **3(1)**: 1–10.
- Garner, D., N. de Souza, and L. Vanderlei, 2020b Unreliability of approximate entropy to locate optimal complexity in diabetes mellitus via heart rate variability. *Series Endo Diab Met.* **2**: 32–40.
- Garner, D., F. Vanderlei, L. Vanderlei, V. Valenti, C. J. R. Benjamim,

- et al.*, 2022 Chaotic global metric analysis of heart rate variability following six power spectral manipulations in malnourished children. *Series Endo Diab Met* **4**: 44–58.
- Garner, D. M., G. S. Barreto, V. E. Valenti, F. M. Vanderlei, A. A. Porto, *et al.*, 2021b HRV analysis: undependability of approximate entropy at locating optimum complexity in malnourished children. *Cardiol Young* pp. 1–6.
- Garner, D. M., N. M. de Souza, V. E. Valenti, and L. C. M. Vanderlei, 2019a Complexity of cardiac autonomic modulation in diabetes mellitus: A new technique to perceive autonomic dysfunction. *Romanian Journal of Diabetes Nutrition and Metabolic Diseases* **26**: 279–291.
- Garner, D. M., N. M. De Souza, and L. C. M. Vanderlei, 2017 Risk assessment of diabetes mellitus by chaotic globals to heart rate variability via six power spectra. *Romanian Journal of Diabetes Nutrition and Metabolic Diseases* **24**: 227–236.
- Garner, D. M., N. M. de Souza, and L. C. M. Vanderlei, 2018 Heart rate variability analysis: Higuchi and katz's fractal dimensions in subjects with type 1 diabetes mellitus. *Romanian Journal of Diabetes Nutrition and Metabolic Diseases* **25**: 289–295.
- Garner, D. M. and B. W. K. Ling, 2014 Measuring and locating zones of chaos and irregularity. *J Syst Sci Complex* **27**: 494–506.
- Garner, D. M. and B. W.-K. Ling, 2021 Measuring and locating zones of chaos and irregularity by application of high spectral chaotic global variants. *International Journal of Bifurcation and Chaos* **31**: 2150236.
- Garner, D. M., F. M. Vanderlei, V. E. Valenti, and L. C. M. Vanderlei, 2019b Non-linear regulation of cardiac autonomic modulation in obese youths: interpolation of ultra-short time series. *Cardiol Young* pp. 1–6.
- Ghil, M., 1997 The SSA-MTM toolkit: Applications to analysis and prediction of time series. *Applications of Soft Computing* **3165**: 216–230.
- Gould, S. H., 1995 *Variational methods for eigenvalue problems: an introduction to the methods of Rayleigh, Ritz, Weinstein, and Aronszajn*. Courier Dover Publications.
- Gourieroux, C., A. Monfort, E. Renault, and A. Trognon, 1987 Generalised residuals. *Journal of econometrics* **34**: 5–32.
- Gray, J. B. and W. H. Woodall, 1994 The maximum size of standardized and internally studentized residuals in regression analysis. *The American Statistician* **48**: 111–113.
- Green, A. L., S. Wang, S. L. Owen, K. Xie, X. Liu, *et al.*, 2005 Deep brain stimulation can regulate arterial blood pressure in awake humans. *Neuroreport* **16**: 1741–5.
- Henriques, T. S., M. D. Costa, P. Mathur, P. Mathur, R. B. Davis, *et al.*, 2019 Complexity of preoperative blood pressure dynamics: possible utility in cardiac surgical risk assessment. *Journal of clinical monitoring and computing* **33**: 31–38.
- Hocht, C., 2013 Blood pressure variability: prognostic value and therapeutic implications. *ISRN Hypertension* **2013**.
- Hodgetts, S. and M. Hausmann, 2022 in *Sex/Gender Differences in Brain Lateralisation and Connectivity*, Springer.
- Hwang, W., D. Kang, and D. Kim, 2022 Brain lateralisation feature extraction and ant colony optimisation-bidirectional LSTM network model for emotion recognition. *IET Signal Processing* **16**: 45–61.
- Jeppesen, J., S. Beniczky, P. Johansen, P. Sidenius, and A. Fuglsang-Frederiksen, 2015 Detection of epileptic seizures with a modified heart rate variability algorithm based on lorenz plot. *Seizure* **24**: 1–7.
- Jinadasa, S. P., A. Mueller, V. Prasad, K. Subramaniam, T. Heldt, *et al.*, 2018 Blood pressure coefficient of variation and its association with cardiac surgical outcomes. *Anesthesia & Analgesia* **127**: 832–839.
- Jolliffe, I., 2005 *Principal component analysis*. Wiley Online Library.
- Kim, J.-S., S. Park, P. Yan, B. W. Jeffers, and C. Cerezo, 2016 Effect of inter-individual blood pressure variability on the progression of atherosclerosis in carotid and coronary arteries: a post hoc analysis of the normalise and prevent studies. *European Heart Journal-Cardiovascular Pharmacotherapy* **3**: 82–89.
- Krout, K. E. and A. D. Loewy, 2000 Periaqueductal gray matter projections to midline and intralaminar thalamic nuclei of the rat. *Journal of Comparative Neurology* **424**: 111–141.
- Lang, A. E. and A. M. Lozano, 1998 Parkinson's disease. *New England Journal of Medicine* **339**: 1130–1143.
- Mackey, M. C. and J. G. Milton, 1987 Dynamical diseases. *Ann N Y Acad Sci* **504**: 16–32.
- Mancia, G., R. Fagard, K. Narkiewicz, J. Redon, A. Zanchetti, *et al.*, 2013 2013 esh/esc guidelines for the management of arterial hypertension: the task force for the management of arterial hypertension of the european society of hypertension (esh) and of the european society of cardiology (esc). *Blood pressure* **22**: 193–278.
- Marcinkiewicz, M., R. Morcos, and M. Chretien, 1989 CNS connections with the median raphe nucleus: Retrograde tracing with wga-apohrp-gold complex in the rat. *Journal of Comparative Neurology* **289**: 11–35.
- Matanes, F., M. B. Khan, M. Siddiqui, T. Dudenbostel, D. Calhoun, *et al.*, 2022 An update on refractory hypertension. *Current Hypertension Reports* **24**: 225–234.
- McAfee, S. S., 2017 *Assessing Neuronal Synchrony and Brain Function Through Local Field Potential and Spike Analysis*. Thesis.
- Miles, J., 2005 R-squared, adjusted r-squared. *Encyclopedia of statistics in behavioral science*.
- Mustafa, E. R., O. Istratoaie, and R. Musetescu, 2016 Blood pressure variability and left ventricular mass in hypertensive patients. *Current health sciences journal* **42**: 47.
- Nazaraghaei, F. and K. K. Bhat, 2020 Physiological impacts of ajapajapa yogic meditation on HRV index, RMSSD, PNN50, heart rate and GSR following three-month training course in comparison to FG meditation. *Journal of Advanced Medical Sciences and Applied Technologies* **5**.
- Newman, D., S. Hilleary, and C. Ginsberg, 1989 Nuclear terminations of corticoreticular fiber systems in rats; pp. 253-264. *Brain, behavior and evolution* **34**: 253–264.
- Nogueira, M. L., D. M. Garner, F. M. Vanderlei, L. C. de Abreu, and V. E. Valenti, 2017 Higuchi fractal dimension applied to rr intervals during exposure to musical auditory stimulation. *Indian J Physiol Pharmacol* **61**: 211–218.
- O'Callaghan, E. L., E. C. Hart, H. Sims-Williams, S. Javed, A. E. Burchell, *et al.*, 2017 Chronic deep brain stimulation decreases blood pressure and sympathetic nerve activity in a drug-and device-resistant hypertensive patient. *Hypertension* **69**: 522–528.
- Osipov, V. and E. Ponizovskaya, 2000 Stochastic resonance in the brusselator model. *Phys.Rev.E.Stat.Phys.Plasmas.Fluids Relat Interdiscip.Topics*. **61**: 4603–4605.
- Packiasabapathy, S., V. Prasad, V. Rangasamy, D. Popok, X. Xu, *et al.*, 2020 Cardiac surgical outcome prediction by blood pressure variability indices poincare plot and coefficient of variation: a retrospective study. *BMC anesthesiology* **20**: 1–12.
- Palatini, P., 2018 Risk of developing foot ulcers in diabetes: contribution of high visit-to-visit blood pressure variability. *Journal of hypertension* **36**: 2132–2134.
- Parati, G., G. Bilo, and M. Valentini, 2008 Blood pressure vari-

- ability: methodological aspects, pathophysiological and clinical implications. *Manual of Hypertension of the European Society of Hypertension* p. 61.
- Parati, G., J. E. Ochoa, and G. Bilo, 2012 Blood pressure variability, cardiovascular risk, and risk for renal disease progression. *Current hypertension reports* **14**: 421–431.
- Parati, G., J. E. Ochoa, C. Lombardi, and G. Bilo, 2013 Assessment and management of blood-pressure variability. *Nature Reviews Cardiology* **10**: 143–155.
- Parati, G., G. S. Stergiou, E. Dolan, and G. Bilo, 2018 Blood pressure variability: clinical relevance and application. *The Journal of Clinical Hypertension* **20**: 1133–1137.
- Patel, N., S. Javed, S. Khan, M. Papouchado, A. Malizia, *et al.*, 2011 Deep brain stimulation relieves refractory hypertension. *Neurology* **76**: 405–407.
- Peng, C. K., S. Havlin, H. E. Stanley, and A. L. Goldberger, 1995 Quantification of scaling exponents and crossover phenomena in nonstationary heartbeat time series. *Chaos* **5**: 82–7.
- Percival, D. and A. Walden, 1993 *Spectral Analysis for Physical Applications: Multitaper and Conventional Univariate Techniques*. Cambridge University Press, New York.
- Pezard, L., J.-L. Nandrino, B. Renault, F. El Massioui, J.-F. Allilaire, *et al.*, 1996 Depression as a dynamical disease. *Biological Psychiatry* **39**: 991–999.
- Pierce, D. A. and D. W. Schafer, 1986 Residuals in generalized linear models. *Journal of the American Statistical Association* **81**: 977–986.
- Pincus, S., 1995 Approximate entropy (apen) as a complexity measure. *Chaos: An Interdisciplinary Journal of Nonlinear Science* **5**: 110–117.
- Ploner, M., C. Sorg, and J. Gross, 2017 Brain rhythms of pain. *Trends in cognitive sciences* **21**: 100–110.
- Prigogine, I., 1962 *Non-equilibrium statistical mechanics..* New York: Interscience.
- Rangasamy, V., T. S. Henriques, X. Xu, and B. Subramaniam, 2020 Preoperative blood pressure complexity indices as a marker for frailty in patients undergoing cardiac surgery. *Journal of cardiothoracic and vascular anesthesia* **34**: 616–621.
- Richman, J. S. and J. R. Moorman, 2000 Physiological time-series analysis using approximate entropy and sample entropy. *Am J Physiol Heart Circ Physiol* **278**: H2039–49.
- Rothwell, P. M., S. C. Howard, E. Dolan, E. O'Brien, J. E. Dobson, *et al.*, 2010 Effects of beta-blockers and calcium-channel blockers on within-individual variability in blood pressure and risk of stroke. *The Lancet Neurology* **9**: 469–480.
- Schmitt, L., J. Regnard, and G. P. Millet, 2015 Monitoring fatigue status with HRV measures in elite athletes: an avenue beyond RMSSD. *Frontiers in physiology* **6**: 343.
- Shannon, C. E., 2001 A mathematical theory of communication. *ACM SIGMOBILE Mobile Computing and Communications Review* **5**: 3–55.
- Silke, B., M. A. Fraix, K. A. Midtbo, S. P. Verma, S. Sharma, *et al.*, 1987 Comparative hemodynamic dose-response effects of five slow calcium channel-blocking agents in coronary artery disease. *Clin Pharmacol Ther* **42**: 381–7.
- Slepian, S., 1978 Prolate spheroidal wave functions, fourier analysis and uncertainty, v, the discrete case. *Bell Syst Tech J* **57**: 1371–1430.
- Spallone, V., 2018 Blood pressure variability and autonomic dysfunction. *Current Diabetes Reports* **18**: 137.
- Srinivasan, V., N. Udayakumar, H. Liang, and K. Anandan, 2022 A hybrid approach for analysis of brain lateralisation in autistic children using graph theory techniques and deep belief networks. *International Journal of Biomedical Engineering and Technology* **39**: 40–64.
- Stoco-Oliveira, M. C., A. L. Ricci-Vitor, L. M. Vanzella, H. B. Valente, V. E. d. S. Silva, *et al.*, 2021 Parkinson's disease effect on autonomic modulation: an analysis using geometric indices. *Arquivos de Neuro-Psiquiatria* **79**: 114–121.
- Subasi, A., 2007 Selection of optimal AR spectral estimation method for eeg signals using cramer-rao bound. *Comput.Biol.Med.* **37**: 183–194.
- Thomson, D. J., 1982 Spectrum estimation and harmonic analysis. *Proceedings of the IEEE* **70**: 1055–1096.
- Tuchler, M., A. C. Singer, and R. Koetter, 2002 Minimum mean squared error equalization using a priori information. *IEEE Transactions on Signal processing* **50**: 673–683.
- Vautard, R., P. Yiou, and M. Ghil, 1992 Singular-spectrum analysis - a toolkit for short, noisy chaotic signals. *Physica D* **58**: 95–126.
- Voss, A., V. Baier, S. Schulz, and K. J. Bar, 2006 Linear and nonlinear methods for analyses of cardiovascular variability in bipolar disorders. *Bipolar Disord* **8**: 441–52.
- Wajnsztein, R., T. D. De Carvalho, D. M. Garner, L. C. M. Vanderlei, M. F. Godoy, *et al.*, 2016 Heart rate variability analysis by chaotic global techniques in children with attention deficit hyperactivity disorder. *Complexity* **21**: 412–419.
- Wang, Z. and A. C. Bovik, 2009 Mean squared error: Love it or leave it: a new look at signal fidelity measures. *IEEE signal processing magazine* **26**: 98–117.
- Webb, A. J., A. Lawson, K. Wartolowska, S. Mazzucco, and P. M. Rothwell, 2021 Progression of beat-to-beat blood pressure variability despite best medical management. *Hypertension* **77**: 193–201.
- Whitmer, D., C. de Solages, B. C. Hill, H. Yu, and H. Bronte-Stewart, 2013 Resting beta hypersynchrony in secondary dystonia and its suppression during pallidal deep brain stimulation in DYT3+ l ubag dystonia. *Neuromodulation: Technology at the Neural Interface* **16**: 200–205.
- Zhou, T. L., R. M. Henry, C. D. Stehouwer, T. T. van Sloten, K. D. Reesink, *et al.*, 2018 Blood pressure variability, arterial stiffness, and arterial remodeling: The maastricht study. *Hypertension* **72**: 1002–1010.

How to cite this article: Garner, D. M., Wang, S., Raghu, A.L.B., Valenti, V.E., Aziz, T.Z., and Green, A.L. Monitoring Blood Pressure Variability via Chaotic Global Metrics using Local Field Potential Oscillations. *Chaos Theory and Applications*, 5(2), 65-77, 2023.

Investigation of the Relationship Between Chaos Data and €/€ Exchange Rate Index Data with RQA Method

Hüseyin Serdar Yalçinkaya^{id}*,1 and Nizamettin Başaran^{id}β,2

*Department of Accounting and Tax, Necmettin Erbakan University, Konya, 42090, Türkiye, βDepartment of Accounting and Tax, Niğde Ömer Halisdemir University, Niğde, 51240, Türkiye.

ABSTRACT A time series data contains a large amount of information in itself. Chaos data and volatility data which calculated by any time series are also derivative information included in the same time series. According to these assumptions, it is very important to question the ability of chaos and volatility information to affect each other, and which information affects and which information is affected. It is very important to determine the causes of volatility, which is an important result indicator for the finance literature, and especially with this study, it was tried to determine whether the chaos data is in a causal relationship with volatility. If some of the chaos data can be identified as the cause of volatility, the detected chaos data can be used in other research as a leading indicator of volatility. The data set used in the study is the daily €/€ exchange rate index between 01.01.2005 and 10.11.2022. In the study, time series of chaos data were created with Windowed RQA method and Hatemi-J asymmetric causality analysis research was carried out between these time series and €/€ exchange rate index volatility. The findings of the study conclude that the chaos data LnRR, LnEntr and LnLAM could be used as leading indicators of the €/€ exchange rate index volatility.

KEYWORDS
Recurrence quantification analysis
Chaos theory
€/€ exchange rate index
Volatility

INTRODUCTION

Traditional methods in determining the fundamental variables in time series containing economic data are generally insufficient because they require time series to be stationary. Making time series stationary can cause data loss and make it difficult to examine long-term behavior (Engle and Granger 1987). RQA is a method that can be applied to stationary and nonlinear time series with insufficient number of data (Kamphorst et al. 1987).

The literature indicates that RQA has found a wide range of applications in other fields of science. In the field of finance, it has been used recently, and the number of related studies is quite limited. The aim of this study is to investigate the causality relationship between the chaos data obtained from the €/€ exchange rate index using the RQA method and volatility. Through this aim, according to the literature review, RQA Method and Hatemi-J Asymmetric Causality Analysis are included in the study. In the 5th part of the study, how the chaos data are prepared is explained

and in the 6th part, the findings obtained by applying the Hatemi-J asymmetric causality analysis to the chaos data are presented. Within the framework of the findings, it can be concluded that the chaos data LnRR, LnEntr and LnLAM can be used as leading indicators of the €/€ exchange rate index volatility. As a result of the obtained results; It has been proven that the RQA method can be used in financial decision processes.

Although the number of studies applying the RQA methodology to the data obtained from the financial time series is increasing day by day in the literature, there are not many studies. In this study, it is tried to examine the relationship between volatility and chaos data, which is an important result indicator in the finance literature with using RQA. Some of the studies on financial time series are summarized below:

Belaire-Franch (2004) examined the time series behavior of simulated data from a financial market model with Lux and Marchesi (1999)'s interacting intermediaries. All RQA descriptors outperformed all nonlinear tests in terms of the number of rejections of the null hypothesis of linearity for the realization of the artificial financial market. Thus, it has been shown in the study that this new framework provides a useful complementary tool for testing complexity in financial data.

Manuscript received: 4 March 2023,

Revised: 5 May 2023,

Accepted: 12 May 2023.

¹ syalcinkaya@erbakan.edu.tr (Corresponding Author)

² nbasaran@ohu.edu.tr

Karagianni and Kyrtsov (2011) investigated the dynamics between US inflation and the Dow Jones Index using a set of nonlinear methods, including RQA, and found evidence in favor of negative nonlinear links between the natural dynamics of inflation and stock returns. Sasikumar and Kamaiah (2014) examined India's two major stock market indices, BSE Sensex and CNX Nifty. The analysis by applying RQA to two time series covering 2002 and 2013 provides conclusive evidence that the Indian stock market is inherently chaotic.

Celik and Afsar (2010)'s study considering the daily return series of the ISE 100 index between 1986 and 2008, concluded that the index movements are 25% based on internal dynamics and are predictable. However, when the ISE 100 index is analyzed by periods, it is seen that the periods of 1991-1995 and 2006-2008 are the periods in which deterministic tendencies are most intense, and the period of 1996-2000 is the period with the weakest predictability.

Niu and Zhang (2017) used MWPE (Multiscale Weighted Permutation Entropy) and RQA methods in their study in which they examined the price fluctuations in exchange rates between 2006 and 2016 in 8 different economies. According to their empirical results; They found that while some economies, such as South Korea, Hong Kong, and China, showed lower and weaker activity in their foreign exchange markets, JPY/USD indicates a higher complexity and the Japanese foreign exchange market has a relatively higher activity. Niu and Zhang (2017) also suggested that the financial crisis increased market efficiency in foreign exchange markets.

Facchini et al. (2019) studied the changes in price volatility after the modification in 2002 using a combination of RP and RQA in their study which is about the UK electricity supply industry. According to the findings of the study, after the modification, short-term price volatility decreased significantly between 2001 and 2008, long-term price volatility was not affected by the change, a dynamic regime change occurred in the price, and shorter GC (Gate Closure) intervals made easier short-term predictions of electricity demand and on the supply side, it facilitates reliability. In the study, the relationship between the GC, which is closer to real time, and the decreasing price fluctuations in the wholesale market is revealed.

Wu et al. (2020) investigated the volatility spread between the crude oil, natural gas and coal futures market and the carbon emissions market using RP and RQA. According to the findings from the study, it was seen that the volatility spread between the coal market and the carbon emission market was stronger than the others. Based on this, industries need to switch from coal to natural gas or oil in order to avoid the risk from the carbon emission market, and it is concluded that this behavior will lead to a reduction in carbon emissions.

Baki (2022b) examined how the dynamic properties of Bitcoin changed over time using RQA. In the study, it was concluded that Bitcoin became more unpredictable, more random, more unstable, more irregular and less complex in 2021.

Baki (2022a) analyzed the USD/TRY and EUR/TRY exchange rates using nonlinear and chaotic time series analysis methods. In the study, RQA and CRQA were used to determine how the chaotic characteristics of the exchange rates changed over time, and it was concluded that the exchange rate market became more unpredictable, more irregular and more unstable after 2014.

In the study, it was tried to determine the chaotic structures occurring in the foreign exchange markets and the interaction of this chaotic structure with volatility. Since the 2008 Mortgage crisis and the Covid-19 outbreak are the most important events that have deeply affected the global financial markets, the data set is

formed from the end-of-day values of the cross currency index of the units \$ (United States Dollar) and € (European Union Euro) money between 01.01.2005 - 01.11.2022 in order to keep it within the scope.

The main problem of the study is to determine whether the chaos or volatility started earlier. If it can be determined that the chaos structure started before the volatility in the foreign exchange market, measures can be taken against volatility with the chaos data which will be explained in the following sections. For this reason, RQA studies will be carried out on the obtained data set and a volatility time series will be created with the historical volatility calculation method over the same time series. In addition, time series will be created on the chaos data to be calculated and the Hatemi-J asymmetric causality test queries will be performed on the derived time series. If a causality can be determined from chaos data to volatility, it will be assumed that investors in the foreign exchange market begin to exhibit different behaviors before volatility begins.

METHODOLOGY

RQA (Recurrence Quantification Analysis)

According to Schumpeter, capitalism is inherently a form of change, and the economy is not static and can never be static (Schumpeter 1976; Orlando and Zimatore 2018). However, time series analyzes used in the literature accept the precondition of being stationary for the time series, if the time series is not stationary, it is requested to make the time series stationary. The stagnation process of the time series, on the other hand, causes data loss, especially in financial time series, and makes the interpretation of the results difficult (Engle and Granger 1987). Kamphorst et al. (1987) developed a method of visualization by transforming one-dimensional time series into two-dimensional with a delay of j in order to facilitate the research due to the stationarity problem in time series. In the method developed by Eckmann, the x_i time series is formed by a matrix with the x_j time series of the same time series with j delay. The repetitions detected by running the cascading \mathcal{H} (Heaviside) function on the obtained matrix are converted to 1, and 0 if there is no repetition. Visual graphics can also be obtained by coloring the matrix consisting of 1 and 0. The resulting square matrix image is called the refresh matrix (R_{ij}). The mathematical derivation method of the renewal matrix is as shown in Equation (1).

$$R_{ij} = \Theta \left(\varepsilon_i \| \vec{x}_i - \vec{x}_j \| \right), \quad \vec{x}_i \in R^m, \quad i, j = 1, 2, \dots, N \quad (1)$$

$$\Theta(x) = \left\{ \begin{array}{l} 1, \quad x_j \geq x_i \\ 0, \quad x_j < x_i \end{array} \right\}$$

In the formula, ' ε_i ' defines the threshold distance, ' Θ ' defines Heaviside stepping function, ' \vec{x}_i ' defines time series vector and ' \vec{x}_j ' defines delay time series vector. The resulting refresh graph can be applied to all stationary or non-stationary time series. In the renewal graph, the dark areas are considered to indicate that the two vectors converge, in other words, a repetition occurs on the time series, and the open areas are considered to indicate that there is no convergence or repetition between the two vectors (Celik and Afsar 2010). Although time series were visualized by Eckmann, mathematical analysis and visual description methods were developed by Zbilut and Webber Jr (2006) and the method was named RQA. While RQA was a method that was used to draw conclusions with topological (changes on the visual) analyzes in the early days, it was translated into mathematical models by the work of Zbilut, Webber, Marwan and Kurths. After this stage, it

has become a more understandable model with the interpretation of various variables obtained by RQA. Some of the numerical data obtained by RQA are explained below, respectively (Marwan and Kurths 2002; Zbilut and Webber Jr 2006).

RR (Recurrence Rate) It measures the repetition density as a percentage on the refresh graph obtained based on the RQA. The higher this ratio, the greater the number of repeated information on the time series. The RR ratio is explained on Equation (2).

$$RR = \frac{1}{N^2} \sum_{i,j=1}^N R(i, j) \quad (2)$$

The 'N' shown in equation (2) describes the recurrence points on the refresh graph.

DET (Determinism Ratio) It is the value that measures the predictability of the time series as a percentage ratio. It is understood that the larger the DET measurement value, the more predictable the system on the time series is. The calculation of the DET value is explained in Equation (3).

$$DET = \frac{\sum_{l=l_{\min}}^N lP(l)}{\sum_{i,j=1}^N R(i, j)} \quad (3)$$

The length of the diagonal lines $P(l)$ formed in the refresh graph shown in the formula l shows the diagonal line length frequency.

Entr (Entropy) The entropy value calculated with the RQA structure is the disorder value defined as Shannon Entropy. It shows that as the Entr value increases, the disorder in the system increases, that is, the time series turns into a chaotic structure, and as it decreases, it shows that the disorder decreases. The calculation made using the equation (4) is shown below:

$$Entr = - \sum_{l=l_{\min}}^N p(l) \ln p(l) \quad (4)$$

The $p(l)$ shown in equation (4) represents the probability of diagonal lines.

LAM (Laminarity) It represents laminar flow in time series. The higher the LAM value in the time series, the more stationary the system is. The frequencies of the vertical lines are used to calculate the slide value and the calculation is shown in Equation (5),

$$LAM = \frac{\sum_{v=v_{\min}}^N vP(v)}{\sum_{v=1}^N vP(v)} \quad (5)$$

The v shown in equation (5) represents the vertical line length on the refresh graph, and $P(v)$ the vertical line length frequency.

Although it is possible to calculate many more variables in RQA, analyzes will be performed with the four variables described in this study. The calculation formulas of the other RQA variables that were not included in the study were not included in this study.

As it can be understood from the calculations of RQA variables, static results are obtained with time series data. When the previous RQA studies were examined, it was examined whether the system had a chaotic structure mostly through the obtained static variables. In order to transform this static structure of RQA into a dynamic structure, Zbilut et al. (2002) created the windowed RQA method with their study. With this proposition, it is shown how to switch from a static structure to a dynamic data set in RQA calculations. Unlike the normal RQA structure, the windowed

RQA structure is divided into smaller time series using the window step number (s) and window size (m) parameters, and the RQA data are calculated over these newly created small time series. Derivative time series of the current time series based on RQA data can be created with the obtained RQA data. Windowed RQA has found use in the analysis of time series in many different fields of science, and in finance, Bastos and Caiado (2011); Piskun and Piskun (2011); Sasikumar and Kamaiah (2014); Soloviev and Belinskiy (2019); Soloviev et al. (2020); Baki (2022a) have been pioneering researchers using windowed RQA analysis techniques. After the windowed RQA technique was put into practice, apart from making inferences from RQA static data, dynamic chaos data were derived and different econometric analyzes were made with time-dependent chaos data indices. With this new situation, the effect of the chaos data obtained from the time series data on the same time series can be examined. Considering the studies examined in the literature review; structural breaks on time series and time series derived from chaos data were examined and the values of RQA data during structural break periods were tried to be interpreted. However, no causality research was conducted between time series and RQA data during structural break periods. In our study, it was aimed to find the traces of chaotic structure on the €/\$ exchange rate, and to reveal the causal relationship between the exchange rate and the chaos data time series that obtained with windowed RQA. Thus, this study will present a different perspective to chaos research on time series.

In the first stage of this study, derivative time series were created with RR, DET, Entr and LAM values obtained as a result of windowed RQA applied on the €/\$ exchange rate time series. In the second stage of the research, causality analyzes will be made between the €/\$ variable and the RR, DET, Entr and LAM variables, and a causality research will be carried out between the variables. In the causality research, Hatemi-J asymmetric causality analysis was preferred, which allows to understand the effects of negative and positive shocks of the variables. The main reason for choosing the Hatemi-J asymmetric causality analysis among the causality analyzes is; It is the desire to investigate how the negative or positive shocks experienced in the chaos data affect the volatility separately. In order to convey the subject better, the Hatemi-J asymmetric causality analysis is briefly explained in the next section.

Hatemi-J Asymmetric Causality Analysis

The concept of causality is a set of models that try to explain the correlation between two variables that depend on the stationarity problem on time series. According to the idea first put forward by Granger in 1969; If x and y are two different time series, y time series lagged values by t can explain x time series, then the hypothesis that y time series is the cause of x time series is accepted. However, it is not known whether the shocks in the y time series are positive or negative. Therefore, it will not be possible to determine whether a positive situation in the y time series or whether a negative situation explains the x time series. In order to eliminate this problem, Hatemi-j (2012) extracted the negative and positive shocks on the time series and derived two different time series, negative and positive, from one time series. By performing a Vector Autoregressive analysis on these derived time series, he was able to reach causality results due to positive and negative shocks (Hatemi-j 2012; Mert and Çağlar 2019). In order to better understand the subject, the mathematical propositions of the Hatemi-J asymmetric causality analysis will be briefly explained. Let x_t and y_t be time series which we think there is a causal relationship be-

tween them. Accordingly, the time series can be written as shown in equations (6) and (7),

$$x_t = x_{t-1} + \varepsilon_t = x_0 + \sum_{i=1}^t \varepsilon_{xi} \quad (6)$$

$$y_t = y_{t-1} + \varepsilon_t = y_0 + \sum_{i=1}^t \varepsilon_{yi} \quad (7)$$

In here, while x_0 and y_0 are the initial values of both time series, ε_{xi} and ε_{yi} are the error terms of time series. The resulting error terms are converted to negative and positive shock data as shown in Equation (8).

$$\varepsilon_{xi}^+ = (\varepsilon_{xi}, 0), \varepsilon_{xi}^- = (0, \varepsilon_{xi}) \quad (8)$$

$$\varepsilon_{yi}^+ = (\varepsilon_{yi}, 0), \varepsilon_{yi}^- = (0, \varepsilon_{yi})$$

and from here we obtain Equation (9),

$$\varepsilon_{xi} = \varepsilon_{xi}^+ + \varepsilon_{xi}^- \text{ and } \varepsilon_{yi} = \varepsilon_{yi}^+ + \varepsilon_{yi}^- \quad (9)$$

After the error terms of the time series are divided into positive and negative series, equations (6) and (7) can be modified and written as equations (10) and (11).

$$x_t = x_{t-1} + \varepsilon_t = x_0 + \sum_{i=1}^t \varepsilon_{xi}^+ + \sum_{i=1}^t \varepsilon_{xi}^- \quad (10)$$

$$y_t = y_{t-1} + \varepsilon_t = x_0 + \sum_{i=1}^t \varepsilon_{yi}^+ + \sum_{i=1}^t \varepsilon_{yi}^- \quad (11)$$

Positive and negative models are obtained from the structure modified as equations (10) and (11).

$$x_t^+ = \sum_{i=1}^t \varepsilon_{xi}^+, \quad x_t^- = \sum_{i=1}^t \varepsilon_{xi}^-, \quad y_t^+ = \sum_{i=1}^t \varepsilon_{yi}^+, \quad y_t^- = \sum_{i=1}^t \varepsilon_{yi}^- \quad (12)$$

Let's build a model as seen in equation (13), which is completely different from the models created in equation (12), and let's assume that this model is valid.

$$z_t^+ = x_t^+ y_t^+ \quad (13)$$

In here, the causality relationship between x_t^+ and y_t^+ variables will be determined by the p delayed Var model.

$$z_t^+ = v + A_1 z_{t-1}^+ + \dots + A_p z_{t-p}^+ + \mu_t^+ \quad (14)$$

In equation (14), z_t^+ denotes 2x1 variable vector, 2x1 denotes constant vector, μ_t^+ denotes 2x1 vector of error terms and A_p denotes 2x2 parameters matrix created for delay p . The results of the Var model are interpreted with the results of the Wald test statistics and the hypotheses are accepted or rejected.

THE DATA SET PREPARATION

In accordance with the purpose of the research, the daily €//\$ exchange rate index was obtained from the Yahoo/finance website between 02/01/2005 - 10/11/2022. The structure of the mentioned data set is shown in Figure 1.

In order to generate RR, DET, Entr and LAM data, which are chaos indicators, [Coco et al. \(2020\)](#) prepared by (CRQA) software was used. Although the CRQA software package was originally prepared for Cross RQA structures, instead of choosing different

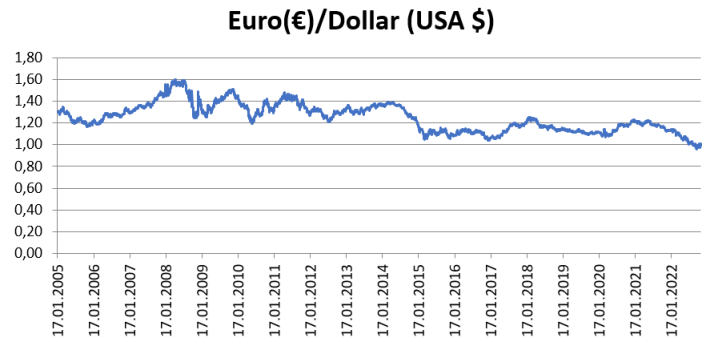


Figure 1 €//\$ Daily Exchange Rate, Source: Yahoo

variables, it turns into an RQA structure if both variables are the same. In addition, the ease of use and the reliability of the tested analysis results were effective in our preference for this software package [Coco and Dale \(2014\)](#). The mentioned CRQA software package runs on the R package program. In order to obtain windowed RQA results in the CRQA software package, the delay number (d), the embedding degree of the phase space (n) and the critical threshold value diameter (r), which are a requirement of the RQA structure, must be determined. In order to obtain these data, it will be necessary to run the "optimizeParam" module, which is also included in the same software package.

When the module that mentioned was run, it was determined that $d=1$, $n=1$ and $r=0.01$. After the necessary parameters were prepared, the window size (m) and window step number (s) values were determined for the windowed RQA. Since daily exchange rate data were used in the research, it was thought that it would be appropriate to produce chaos data as daily data, and $s=1$, that is, the number of window steps was determined as 1 day. For the appropriate window size, the 'windowdrp' module was run and it was determined that the smallest suitable window size would be $m=10$. Chaos data of the €//\$ exchange rate time series were obtained with all the parameters obtained, and the graphics of the chaos data are presented below.

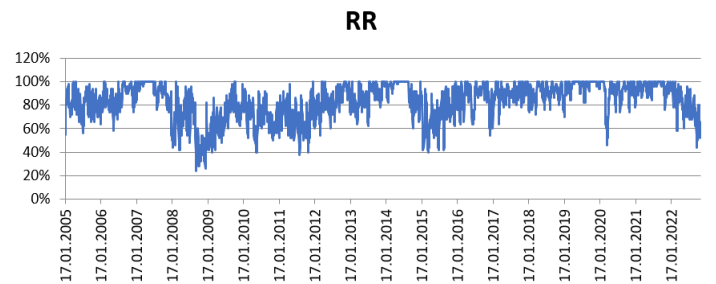


Figure 2 Daily RR Time Series

The RR value shows the number of repetitions of an information on the time series, and as this value decreases, it shows that the repetition of the information decreases. When Figure 2 is examined, the rate of recurrence before the 2008 crisis approached 100% and decreased to 20% with the onset of the crisis.

DET data determines the deterministic structure of the time series, that is, its predictability. While DET data, like RR data, had a high value before 2008, it was at low levels until 2014. Afterwards, it entered an upward trend again until 2020, the predictability of the time series decreased with the pandemic crisis.

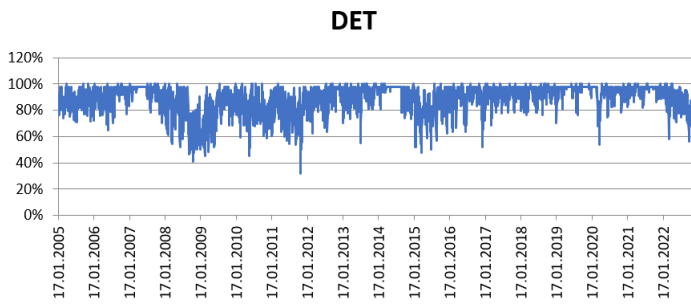


Figure 3 DET Time Series

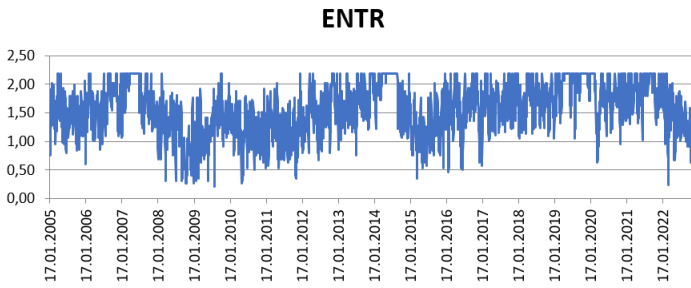


Figure 4 Entr Time Series

Entr is a measure of the disorder on the time series. If the information in the time series is in the same direction, the Entr variable will approach zero, and if the information differs, the value of the Entr variable will increase. According to the random walk hypothesis in financial markets, if Entr data is interpreted, the efficient market should be in a high entropy state. Otherwise, since all investors in the financial market will have the same opinion, the predictability of prices will increase.

When Figure 4 is examined, the entropy of the €//\$ exchange rate reached the highest levels before the 2008 crisis, and after the crisis, the complexity in the market started to decrease.

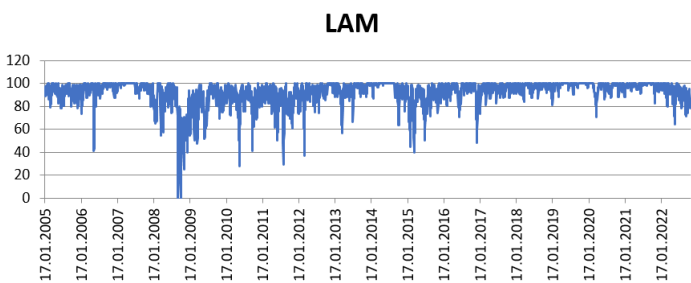


Figure 5 LAM Time Series

LAM data is an indicator of the stationarity of the time series. In the RQA literature, it is stated that LAM data is a suitable data for detecting the exit from chaos (Orlando and Zimatore 2018). When Figure 5 is examined, the LAM value decreased to its lowest level at the end of 2009 and showed a rapid increase after that. For this reason, it is necessary to carefully examine the proposition that sudden and large increases in the LAM value can be the points of exit from the chaos of the time series.

After creating the chaos data to be used in the research, historical volatility time series were created from the €//\$ exchange rate

index data. The reason for using historical volatility instead of logarithmic return is to investigate whether chaos data has an effect on volatility, which is a measure of risk in the market. For this purpose, it was decided to use the historical volatility time series with the thought that more accurate results would be obtained, and Equation (15) was used in the calculation of this series.

$$\sigma = |P_n - P_{n-1}| \quad (15)$$

In here, by calculating the absolute value of the difference between the price of P and the price of the previous period, the historical volatility time series is created and shown in Figure 6.

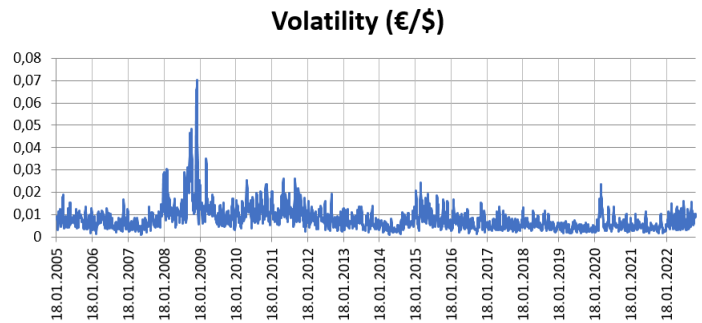


Figure 6 €//\$ Exchange Rate Volatility Time Series

EMPIRICAL FINDINGS

The Hatemi-J asymmetric causality analysis, which was previously explained, will be performed in order to test whether the chaos data has an effect on the €//\$ exchange rate volatility with the created data set. However, since the fundamental theorem of this analysis is the Var analysis, the stationarity problem of the time series should be questioned. Unit root tests are used to detect stationarity problems in time series. In this study, PP and ADF unit root tests were performed on time series and their results are shown in Table-1.

Notes: (*)Significant at the 10%; (**)Significant at the 5%; (***)Significant at the 1%. and (no) Not Significant *MacKinnon (1996) one-sided p-values.

As can be seen from the test results in Table-1, no unit root problem was detected in any of the variables to be used in the research, and accordingly, all of the variables were considered stationary at the level. In the next stage, the Var model was established and the most appropriate number of lags between the variables was determined and presented in Table-2.

The most appropriate lag number of the model created according to Table-2 was determined as 2 periods, and the results of the analysis were obtained with this lag number in the Hatemi-J asymmetric causality analysis and the results are presented in Table-3.

When the causality analysis results were examined, it was determined that both the negative shocks and positive shocks of the chaos data RR, DET, Entr and LAM data were not the cause of the negative and positive shocks of the €//\$ exchange rate index volatility. However, on the contrary, the negative and positive shocks of the €//\$ exchange rate index volatility are the cause of the negative and positive shocks of the RR, DET, Entr and LAM data. Depending on these determinations, while the volatility variable affects the chaos data, the chaos data does not affect the volatility.

■ **Table 1** Unit Root Test Results

UNIT ROOT TEST TABLE (PP)

		<u>At Level</u>				
		DET	ENTR	LAM	RR	Volatilite
With Constant	t-Statistic	-32.6300	-16.7856	-16.5460	-10.3829	-9.8304
	<u>Prob.</u>	<u>0.0000</u>	<u>0.0000</u>	<u>0.0000</u>	<u>0.0000</u>	<u>0.0000</u>
		***	***	***	***	***
With Constant & Trend	t-Statistic	-33.6054	-17.3222	-17.2308	-11.1659	-10.2556
	<u>Prob.</u>	<u>0.0000</u>	<u>0.0000</u>	<u>0.0000</u>	<u>0.0000</u>	<u>0.0000</u>
		***	***	***	***	***

UNIT ROOT TEST TABLE (ADF)

		<u>At Level</u>				
		DET	ENTR	LAM	RR	STDAVDO
With Constant	t-Statistic	-7.5979	-9.6085	-7.3866	-5.0824	-14.5642
	<u>Prob.</u>	<u>0.0000</u>	<u>0.0000</u>	<u>0.0000</u>	<u>0.0000</u>	<u>0.0000</u>
		***	***	***	***	***
With Constant & Trend	t-Statistic	-7.9746	-10.0362	-7.7480	-5.2695	-15.3171
	<u>Prob.</u>	<u>0.0000</u>	<u>0.0000</u>	<u>0.0000</u>	<u>0.0001</u>	<u>0.0000</u>
		***	***	***	***	***

■ **Table 2** The Most Appropriate Number of Lags

Lag	LogL	LR	FPE	AIC	SC	HQ
0	1885.041	NA	0.000189	-2.896987	-2.889032	-2.894002
1	2106.520	441.9349	0.000135	-3.231569	-3.207707	-3.222616
2	2170.273	127.0159*	0.000124*	-3.323497*	-3.283727*	-3.308575*

■ **Table 3** Hatemi-J Causality Analysis Results Between Chaos Data and Volatility

	Wald İst.	%1	%5	%10
entr +=>vol+	3.923	13.234	7.748	4.509
entr +=>vol-	2.529	11.237	8.170	4.642

■ **Table 3** Hatemi-J Causality Analysis Results Between Chaos Data and Volatility (continued)

entr \Rightarrow vol+	3.735	10.172	7.891	5.428
entr \Rightarrow vol-	2.324	11.765	7.072	5.143
Vol+ \Rightarrow entr+	25.132(*)	13.321	7.943	5.802
Vol+ \Rightarrow entr-	35.223(*)	11.632	6.832	4.732
vol- \Rightarrow entr+	31.219(*)	12.167	6.982	4.290
vol- \Rightarrow entr-	45.208(*)	11.291	6.219	4.231
rr \Rightarrow vol+	3.764	10.874	6.326	4.248
rr \Rightarrow vol-	5.043	12.215	7.884	6.981
rr \Rightarrow vol+	1.028	12.183	6.994	5.875
rr \Rightarrow vol-	1.432	11.764	7.162	6.231
vol+ \Rightarrow rr+	35.278(*)	10.342	6.442	4.743
vol+ \Rightarrow rr-	42.237(*)	12.453	7.349	5.658
vol- \Rightarrow rr+	46.286(*)	12.893	6.238	4.673
vol- \Rightarrow rr-	39.587(*)	12.752	7.872	5.125
det \Rightarrow vol+	3.543	11.592	7.816	5.827
det \Rightarrow vol-	2.445	12.986	8.438	6.521
det \Rightarrow vol+	3.091	11.446	7.171	6.392
det \Rightarrow vol-	2.854	12.659	8.215	6.383
vol+ \Rightarrow det+	23.842(*)	11.832	6.212	5.408
vol+ \Rightarrow det-	36.128(*)	11.109	6.649	5.787
vol- \Rightarrow det+	43.485(*)	12.954	8.221	6.734
vol- \Rightarrow det-	44.228(*)	11.184	7.843	5.543
lam \Rightarrow vol+	1.556	11.265	6.978	4.874
lam \Rightarrow vol-	1.754	13.129	8.508	6.548
lam \Rightarrow vol+	2.386	12.328	8.761	6.109
lam \Rightarrow vol-	1.326	13.673	8.265	6.439
vol+ \Rightarrow lam+	22.452(*)	11.912	6.867	4.381
vol+ \Rightarrow lam-	35.945(*)	12.769	6.743	4.214
vol- \Rightarrow lam+	39.281(*)	14.679	9.389	7.222
vol- \Rightarrow lam-	28.328(*)	12.769	8.325	6.927

According to this result, it is not possible to make early decisions about volatility using chaos data. However, chaos data was used directly in the research and it was not allowed to clearly reveal negative and positive shocks. In order to eliminate this problem, new time series were created by taking the logarithmic differences of the chaos data. The new time series created are presented in Figures 7,8,9,10.

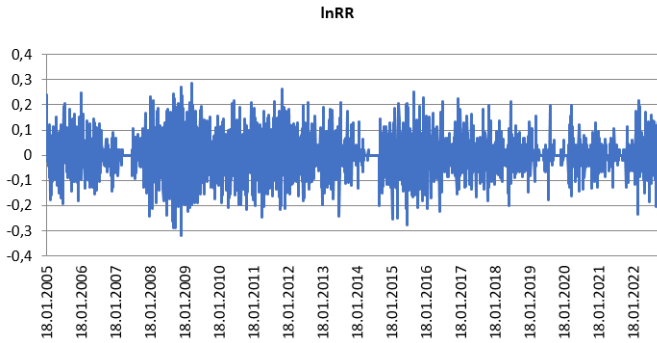


Figure 7 $\ln RR = \ln(RR_n/RR_{n-1})$

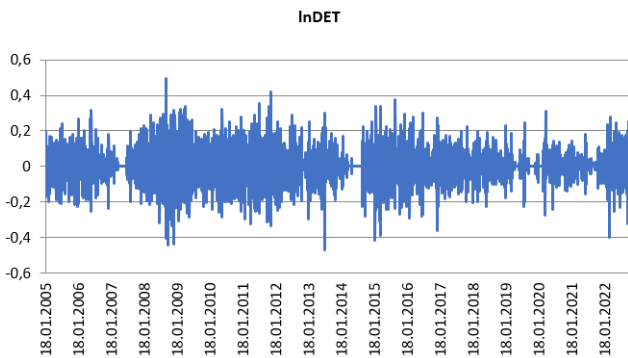


Figure 8 $\ln DET = \ln(DET_n/DET_{n-1})$

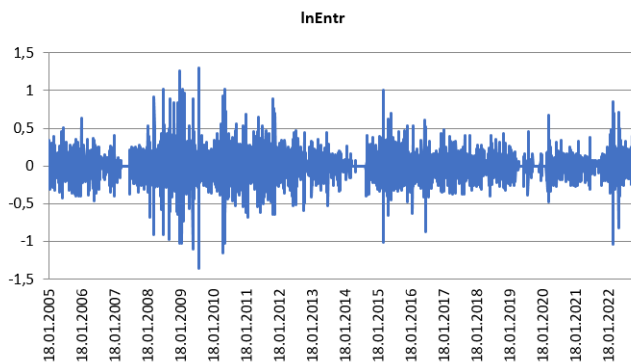


Figure 9 $\ln Entr = \ln(Entr_n/Entr_{n-1})$

With the new variables created, the Hatemi-J asymmetric causality analysis procedures were repeated and the new analysis results are presented in tables below. While the negative and positive differences in the logarithmic difference of the RR data, which gives the repetition percentage of the time series, were determined as the cause of the positive shocks of volatility, causality towards

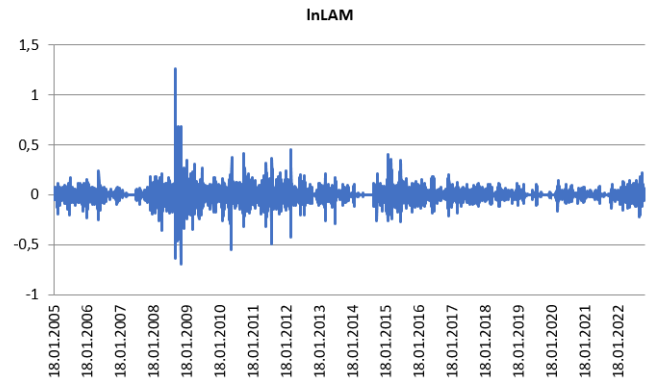


Figure 10 $\ln LAM = \ln(LAM_n/LAM_{n-1})$

the negative shocks of volatility of the same variable could not be determined.

The negative and positive shocks of the €/€ exchange rate volatility are the cause of both the negative and positive shocks of the LnRR variable. Based on these determinations, it is accepted that the LnRR variable can be used as a leading indicator for positive shocks of €/€ exchange rate volatility, and additionally that all shocks in the €/€ exchange rate volatility are the cause of the LnRR variable makes it difficult to accept the LnRR variable as a leading indicator in any case.

Depending on these determinations, LnRR data can be used as a leading indicator that €/€ exchange rate volatility will increase when sudden and large shocks are detected, as in the crises experienced in 2008 and 2020. However, this determination does not reduce the importance of the LnRR variable, if it is followed as an index, it can be added to the literature as a very important leading indicator in terms of increasing the limited data diversity in risk management.

It has been understood that the logarithmic difference of LnDET, which is the predictive variable in chaos data, does not affect the negative or positive shocks of volatility. On the contrary, it is understood that both negative and positive shocks of volatility affect the negative and positive shocks of LnDET. Depending on these determinations, it is not possible to use the LnDET variable as a leading indicator. However, it can be used to understand and interpret the general situation in the time series.

When the asymmetric causality analysis results between the logarithmic difference value of the entropy data, which is the indicator of the irregularity in the time series, and the €/€ exchange rate volatility are examined, it is understood that the LnRR, that is, the repetition data, shows consistent results with the logarithmic difference. Here, the hypothesis that the negative and positive shocks of the LnEntr data is the cause of the negative shock of the €/€ exchange rate volatility is accepted.

The negative and positive shocks of the €/€ exchange rate volatility are the cause of both the negative and positive shocks of the LnEntr data. In this case, it is understood that the result obtained with LnRR data is the opposite for LnEntr, and this result should be considered quite consistent. Because while RR is a measure of regular repetitions, Entr is defined as a measure of irregularity and they give opposite results. With this study, it has been accepted that it is possible to use sudden large shocks in the logarithmic difference of entropy as a leading indicator that volatility will decrease.

■ **Table 4** Causality Results Between LnRR and Exchange Rate Volatility

	Wald İst.	%1	%5	%10
Lnrr +=>vol+	10.199 (**)	11.863	7.538	5.728
Lnrr +=>vol-	4.390	12.005	7.994	6.241
Lnrr -=>vol+	918.028(*)	9.243	5.928	4.605
Lnrr -=>vol-	1.156	11.884	7.817	6.191
vol+ => Lnrr+	79.618(*)	10.587	6.213	4.698
vol+ => Lnrr-	44.174(*)	12.149	7.733	5.909
vol- => Lnrr+	86.936(*)	10.593	6.101	4.535
vol- => Lnrr-	49.521(*)	10.902	6.638	5.008

■ **Table 5** Causality Results Between LnDET and Exchange Rate Volatility

	Wald İst.	%1	%5	%10
Lndet +=>vol+	2.815	11.828	7.535	5.836
Lndet +=>vol-	0.020	12.273	8.434	6.626
Lndet -=>vol+	3.464	11.961	7.814	6.224
Lndet -=>vol-	0.324	12.726	8.791	6.863
vol+ => Lndet+	47.638(*)	11.868	6.892	5.114
vol+ => Lndet-	76.446(*)	12.090	7.456	5.577
vol- => Lndet+	26.934(*)	12.779	8.612	6.800
vol- => Lndet-	37.082(*)	11.311	7.550	5.895

■ **Table 6** Causality Results Between LnEntr and Exchange Rate Volatility

	Wald İst.	%1	%5	%10
Lnentr +=>vol+	2.193	14.229	8.078	5.959
Lnentr +=>vol-	217.272(*)	12.897	7.890	5.802
Lnentr -=>vol+	3.022	12.611	8.011	6.227
Lnentr -=>vol-	216.543(*)	11.855	7.562	5.653
Vol+ => Lnentr+	37.221(*)	14.161	7.053	5.106
Vol+ => Lnentr-	58.123(*)	11.390	6.620	4.855
vol- => Lnentr+	41.256(*)	12.000	7.539	5.670
vol- => Lnentr-	41.256(*)	12.000	7.539	5.670

■ **Table 7** Causality Results Between LnLAM and Exchange Rate Volatility

	Wald İst.	%1	%5	%10
LnLAM +=>vol+	198.185(*)	9.802	5.921	4.478
LnLAM +=>vol-	3.277	13.418	8.090	6.259
LnLAM -=>vol+	2.825	15.565	8.400	6.078
LnLAM -=>vol-	1.181	13.579	8.250	6.198
vol+ => LnLAM+	36.330(*)	13.907	6.780	4.901
vol+ => LnLAM-	56.945(*)	12.240	6.667	4.884
vol- => LnLAM+	39.281(*)	14.679	9.389	7.222
vol- => LnLAM-	56.272(*)	12.954	8.229	6.183

Notes: (*)There is causality with 1% margin of error. (**)There is causality with 5% margin of error. (***)There is causality with 10% margin of error.

According to the results of the causality inquiry that is made between the logarithmic difference values of the LAM data, which is an indicator of a stable structure in time series, and the €/ \$ exchange rate volatility; The positive shocks of the LnLAM data are determined to be the cause of only the positive shocks of the €/ \$ exchange rate volatility, while the negative shock of the LnLAM data is not the cause of the negative and positive shocks of the volatility. With this finding, it was concluded that positive shocks in LnLAM data can be used as an important indicator that volatility will increase.

CONCLUSION

When the literature in the field of RQA is examined, it has been seen that the chaotic structures on the time series are interpreted by calculating static chaos data by dividing the time series into certain sub-time periods. By using the chaos data converted from static structure to dynamic structure with windowed RQA, it was possible to create time series and limited number of studies on this subject could be reached. From these studies;

Soloviev *et al.* (2020) tested whether the chaos data would be a leading indicator by detecting structural breaks on the daily data of the US, German and French stock markets. According to the results of the research, it has been suggested that DET, LAM and Entr data can be used as crisis leading indicators.

Piskun and Piskun (2011) produced windowed RQA dynamic chaos data during financial crisis periods in different countries and argued that LAM data could be the leading indicator of crises by detecting structural breaks on these data.

The path followed in the research conducted in the field of finance with windowed RQA is generally to determine the structural break times of the time series in order to determine the relationship between the generated chaos data and volatility. In our study, whether the chaos data will be a leading indicator for volatility was investigated by Hatemi-J asymmetric causality analysis. In this respect, this study reveals an innovation for the finance literature. Our study has proven that RR, Entr and LAM data can be leading indicators of volatility, consistent with other studies. However, it has also been proven in the study that using logarithmic differences instead of using these data directly will give better results.

As a result of econometric analysis, it was determined that the negative and positive shocks of the LnRR value were the cause of the positive shocks of the €/ \$ exchange rate volatility, and the negative and positive shocks of the LnEntr value were the cause of the negative shocks of the €/ \$ exchange rate volatility. In addition, it has been determined that the positive shock of the LnLAM value is the cause of the positive shock of the €/ \$ exchange rate volatility. It has also been determined that both negative and positive shocks of the €/ \$ exchange rate volatility are the cause of the negative and positive shocks of all chaos data. According to this result, it is concluded that the €/ \$ exchange rate volatility affects the chaos data under normal conditions, while the chaos data has the ability to affect the €/ \$ exchange rate volatility in extreme cases (Financial Crises). This interpretation of opinion does not eliminate the importance of chaos data in volatility analysis. It indices to be derived from chaos data (especially LnRR, LnEntr and LnLAM) have increased their importance in order to provide new opportunities for analysis for stakeholders working in the field of volatility detection and risk management.

Conflicts of interest

The authors declare that there is no conflict of interest regarding the publication of this paper.

Availability of data and material

Not applicable.

LITERATURE CITED

- Baki, U., 2022a Nonlinear chaotic analysis of usd/try and eur/try exchange rates. *Eskişehir Osmangazi Üniversitesi İktisadi ve İdari Bilimler Dergisi* **17**: 410–432.
- Baki, U., 2022b Stability analysis of bitcoin using recurrence quantification analysis. *Chaos Theory and Applications* **4**: 104–110.
- Bastos, J. A. and J. Caiado, 2011 Recurrence quantification analysis of global stock markets. *Physica A: Statistical Mechanics and its Applications* **390**: 1315–1325.
- Belaire-Franch, J., 2004 Testing for non-linearity in an artificial financial market: a recurrence quantification approach. *Journal of Economic Behavior & Organization* **54**: 483–494.
- Celik, M. Y. and K. E. Afsar, 2010 Finansal zaman serilerinde yineleme haritaları analizi: İmkb Örneği. *Dumlupınar Üniversitesi Sosyal Bilimler Dergisi*.
- Coco, M. I. and R. Dale, 2014 Cross-recurrence quantification analysis of categorical and continuous time series: an r package. *Frontiers in psychology* **5**: 510.
- Coco, M. I., D. Mønster, G. Leonardi, R. Dale, and S. Wal-lot, 2020 Unidimensional and multidimensional methods for recurrence quantification analysis with crqa. *arXiv preprint arXiv:2006.01954*.
- Engle, R. F. and C. W. Granger, 1987 Co-integration and error correction: representation, estimation, and testing. *Econometrica: journal of the Econometric Society* pp. 251–276.
- Facchini, A., A. Rubino, G. Caldarelli, and G. Di Liddo, 2019 Changes to gate closure and its impact on wholesale electricity prices: The case of the uk. *Energy Policy* **125**: 110–121.
- Hatemi-j, A., 2012 Asymmetric causality tests with an application. *Empirical economics* **43**: 447–456.
- Kamphorst, J.-P., D. Ruelle, *et al.*, 1987 Recurrence plots of dynamical systems. *Europhysics Letters* **4**: 17.
- Karagianni, S. and C. Kyrtsov, 2011 Analysing the dynamics between us inflation and dow jones index using non-linear methods. *Studies in Nonlinear Dynamics & Econometrics* **15**.
- Marwan, N. and J. Kurths, 2002 Nonlinear analysis of bivariate data with cross recurrence plots. *Physics Letters A* **302**: 299–307.
- Mert, M. and A. E. Çağlar, 2019 EvIEWS ve gauss uygulamalı zaman serileri analizi. Ankara: Detay Yayıncılık pp. 183–213.
- Niu, H. and L. Zhang, 2017 Nonlinear multiscale entropy and recurrence quantification analysis of foreign exchange markets efficiency. *Entropy* **20**: 17.
- Orlando, G. and G. Zimatore, 2018 Recurrence quantification analysis of business cycles. *Chaos, Solitons & Fractals* **110**: 82–94.
- Piskun, O. and S. Piskun, 2011 Recurrence quantification analysis of financial market crashes and crises. *arXiv preprint arXiv:1107.5420*.
- Sasikumar, A. and B. Kamaiah, 2014 A complex dynamical analysis of the indian stock market. *Economics Research International* **2014**.
- Schumpeter, J. A., 1976 *Li. capitalism, socialism, and democracy*, 1942.
- Soloviev, V., O. Serdiuk, S. Semerikov, and A. Kiv, 2020 Recurrence plot-based analysis of financial-economic crashes. *CEUR Workshop Proceedings*.

- Soloviev, V. N. and A. Belinskiy, 2019 Complex systems theory and crashes of cryptocurrency market. In Information and Communication Technologies in Education, Research, and Industrial Applications: 14th International Conference, ICTERI 2018, Kyiv, Ukraine, May 14-17, 2018, Revised Selected Papers 14, pp. 276–297, Springer.
- Wu, Q., M. Wang, and L. Tian, 2020 The market-linkage of the volatility spillover between traditional energy price and carbon price on the realization of carbon value of emission reduction behavior. *Journal of Cleaner Production* **245**: 118682.
- Zbilut, J. P., N. Thomasson, and C. L. Webber, 2002 Recurrence quantification analysis as a tool for nonlinear exploration of nonstationary cardiac signals. *Medical engineering & physics* **24**: 53–60.
- Zbilut, J. P. and C. L. Webber Jr, 2006 Recurrence quantification analysis. *Wiley encyclopedia of biomedical engineering* .

How to cite this article: Yalcinkaya, H. S., and Basaran, N. Investigation of the Relationship Between Chaos Data and €/\$ Exchange Rate Index Data with RQA Method. *Chaos Theory and Applications*, 5(2), 78-89, 2023.

Bifurcation Analysis and 0-1 Chaos Test of a Discrete T System

Sarker Md. Sohel Rana ^{*,1}

*Department of Mathematics, University of Dhaka, Dhaka, 1000, Bangladesh.

ABSTRACT This study examines discrete-time T system. We begin by listing the topological divisions of the system's fixed points. Then, we analytically demonstrate that a discrete T system sits at the foundation of a Neimark Sacker(NS) bifurcation under specific parametric circumstances. With the use of the explicit Flip-NS bifurcation criterion, we establish the flip-NS bifurcation's reality. Center manifold theory is then used to establish the direction of both bifurcations. We do numerical simulations to validate our theoretical findings. Additionally, we employ the 0-1 test for chaos to demonstrate whether or not chaos exists in the system. In order to stop the system's chaotic trajectory, we ultimately employ a hybrid control method.

KEYWORDS

T system
Stability
Bifurcations
Chaos Control

INTRODUCTION

The nonlinear differential systems, including those in engineering, economy, physics, biology, chemistry, and other domains, have been explored from both theoretical and potential practical perspective. The feature of sensitivity to the beginning circumstances is frequently seen in nonlinear systems (some authors consider this property sufficient for a system to be chaotic). One of the first examples of a 3-D continuous dynamical system using numerical simulations that illustrate the property of sensitivity to initial conditions is the Lorenz system (Lorenz 1963).

The Rayleigh-Benard experiment is the Lorenz system's physical implementation. A dynamical model for meteorology was developed using the system, which was derived from the hydrodynamical Navier-Stokes equations. Scientists have looked into numerous 3-D chaotic systems as a result of his classically innovative work. After a decade, Rössler (1976) made the discovery of a 3-D chaotic system that had been built up while studying a chemical reaction. The discovery of numerous 3-D chaotic systems was made possible by these classical pioneering works on chaotic systems. Attempting to convert the Lorenz system from a stable to a chaotic condition (concept known as anticontrol of chaos), Lü *et al.* (2002) and Ueta and Chen (2000) constructed new critical chaotic systems by anti-control technique in Lorenz system (Lorenz 1963) which were known as Lü system and Chen's system respectively.

Qualitative analyses of these empirical works found many dynamical properties including local bifurcations, chaotic, periodic, quasi-periodic orbits and route to chaos. They also obtained super-critical and sub-critical bifurcations conditions around positive equilibrium. In Sachdev and Sarathy (1994), a nonlinear system resulting from a nuclear spin generator is explored and contrasted with the Lorenz system. The T system, which Tigan (Tigan 2005) explored, is a novel chaotic system deriving from the Lorenz system. The system T exhibits a more complicated dynamics than the Lü system because it offers greater flexibility in selecting the system's parameters. To improve the chaotic system's complexity and the accuracy of the weak signal detection, a novel 3-D chaotic system studied (Luo *et al.* 2020). A 3-D jerk system dynamics examined in (Kengne *et al.* 2016), which can be utilized as an analog simulator for experiments made in a lab. This work investigated several dramatic and uncommon bifurcation situations, such as those with multiple attractors, symmetry-recovering crises, and basins of attraction for a variety of coexisting attractors. These applications provide justification for the creation of new chaotic systems. Numerous fields, ranging from ecology (Tang and Chen 2003) and physics (El Naschie 2003), encounter nonlinear dynamics.

We recall some applications of such systems in biological systems, secure communication, information processing (see, for example, (Babloyantz *et al.* 1985; Chen and Dong 1998; Chen 1999; Pecora and Carroll 1991; Rabinovich and Abarbanel 1998; Yang and Chua 1997)). A numerous number of scholars have been given attention and investigated extensively system's bifurcation in continuous dynamical system, but a little works have been studied in system's bifurcations in discrete dynamical system. However, a lot of exploratory works have been suggested that discrete-time

Manuscript received: 4 December 2022,

Revised: 20 April 2023,

Accepted: 22 May 2023.

¹ srana.mthdu@gmail.com (Corresponding Author)

models are more suitable compared to differential equation model as discrete-time model reveal rich chaotic dynamics and give effective computational models for numerical simulations (Chakraborty et al. 2020; Li and He 2019; Liu and Li 2021; Rana 2019b,a; Zhao 2021; Liu and Li 2021; Zhang et al. 2022; Fei et al. 2021; Singh and Deolia 2021). These studies investigated unexpected characteristics, such as the occurrence of (flip-NS) bifurcations and chaotic events, using either numerical methods or center manifold theory applications. In fact, these studies solely focused on 2-D discrete systems.

A limited number of contributions have recently been made to the study of the dynamics of 3-D discrete systems (Khan and Javaid 2021; Abdelaziz et al. 2020; Din and Ishaque 2019; Feng et al. 2021; Hu et al. 2014; Ishaque et al. 2019; Qin et al. 2016; Khan et al. 2021; Xin et al. 2010). For example, a discrete-time SIR epidemic models discussed in (Abdelaziz et al. 2020; Khan et al. 2021; Hu et al. 2014), in (Xin et al. 2010) the authors investigated discrete financial system and in (Qin et al. 2016), the authors studied discrete chaotic system.

The explicit Flip-NS bifurcation criterion, center manifold theory, and bifurcation theory were all used by the researchers in these works to focus their efforts on figuring out the direction and stability of Flip and NS bifurcation. The studies in (Khan and Javaid 2021; Din and Ishaque 2019; Ishaque et al. 2019) investigated discrete population models. In (Feng et al. 2021), the authors explored NS bifurcation for discrete food chain model. For the existence of flip and NS bifurcations, these research solely employed the explicit (Flip-NS bifurcation) criteria and numerical simulations. In nonlinear field research, the chaos theory has recently attracted a lot of attention.

In light of the aforementioned research projects, we express our interest in studying at 3-D T system (Tigan 2005):

$$\begin{aligned} \dot{x} &= a(y - x) \\ \dot{y} &= (c - a)x - axz \\ \dot{z} &= xy - bz \end{aligned} \quad (1)$$

In system (1), $x, y, z \in \mathbb{R}$ are the state variables with parameters $a, b, c \in \mathbb{R}$ and $a \neq 0$. The parameters $a, b, c \in \mathbb{R}^+$ in the system represent the Prandtl number, the Rayleigh number, and some physical proportions of the region under study and for more description of these parameters we refer (Sparrow 2012). Diverse perspectives were used to study the T system: dynamics (Jiang et al. 2010), chaos control (Yong and Zhen-Ya 2008), anti-synchronization (Vaidyanathan and Rajagopal 2011). Secure communications might benefit from the system (1) (Li et al. 2009; Sundarapandian 2011). The T system undergoes a Hopf bifurcation and possesses a strange chaotic attractor (Jiang et al. 2010).

A continuous-time differential equation can be discretized in a variety of ways, but the fourth-order Runge-Kutta approach and the forward Euler scheme are the most straightforward. The discrete systems' features can change significantly from those of the original continuous ones since the forward Euler technique uses first-order precision to solve approximation differential equation solutions. However, a big step size ensures low stability of the selected Euler integrator, which means all of the impacts we see may have nothing to do with the characteristics of the original continuous system. This intentionally induced instability of the finite-difference system is where the chaotic regimes mostly develop. How the forward Euler scheme affects the capabilities

of continuous systems is something we are interested in. Our present work is looking at a discrete-time system that is built on the continuous-time 3D T system. Applying forward Euler scheme, the discrete form of (1) is given by

$$\begin{pmatrix} x \\ y \\ z \end{pmatrix} \rightarrow \begin{pmatrix} x + \delta(a(y - x)) \\ y + \delta((c - a)x - axz) \\ z + \delta(xy - bz) \end{pmatrix} \quad (2)$$

We are motivated to investigate the T system in discrete form because of the interest in studying it. The discrete T system differs from the continuous one in both characteristics and structure, according to analysis. The Flip and NS bifurcations play an significant role for generation of critical chaotic dynamics in discrete system and trigger a route to chaos. The objective of this work is to analyze systematically the conditions for occurrence of flip and NS bifurcations by using an explicit Flip-NS bifurcation criterion and to determine the stability and direction of both bifurcations by the applications of bifurcation theory.

The structure of this study is as follows. The local stability requirements of possible fixed points are examined in Section 2. In Section 3, we theoretically examine whether the system (2) experiences a Flip or NS bifurcation under a certain parametric condition. To support the conclusions of our analytical work, we numerically show system dynamics in Section 4 together with bifurcation diagrams, phase portraits, and MLEs. There is also a 0 - 1 chaotic test method offered. In Section 5, we put a hybrid control technique into practice to stabilize the uncontrolled system's chaos. We provide a brief summary in Section 6.

LOCAL DYNAMICS

The fixed points of the system (2) are the solutions of the following system of non-linear equations:

$$\begin{aligned} x &= x + \delta(a(y - x)) \\ y &= y + \delta((c - a)x - axz) \\ z &= z + \delta(xy - bz) \end{aligned} \quad (3)$$

By some algebraic computation, we obtain the following lemma.

Lemma 1 (i) For any parameter values, the system (2) has only one fixed point $E_0 = (0, 0, 0)$, (ii) if $c > a$, the system (2) has three fixed points $E_0 = (0, 0, 0)$, and $E_{\pm} = (x^{\pm}, y^{\pm}, z^{\pm}) = \left(\pm \sqrt{\frac{b}{a}(c - a)}, \pm \sqrt{\frac{b}{a}(c - a)}, \frac{c - a}{a} \right)$.

Given at fixed point $E(x, y, z)$, the Jacobian matrix of the system (2) and its characteristic equation are as follows

$$J(E) = \begin{pmatrix} 1 - a\delta & a\delta & 0 \\ -(a - c + az)\delta & 1 & -ax\delta \\ y\delta & x\delta & 1 - b\delta \end{pmatrix} = (j_{kl}), \quad k, l = 1, 2, 3 \quad (4)$$

and

$$P(\mu) := \mu^3 + \vartheta_2\mu^2 + \vartheta_1\mu + \vartheta_0 = 0 \quad (5)$$

where,

$$\begin{aligned} \vartheta_2 &= -tr(J), \\ \vartheta_1 &= \begin{vmatrix} j_{11} & j_{12} \\ j_{21} & j_{22} \end{vmatrix} + \begin{vmatrix} j_{22} & j_{23} \\ j_{32} & j_{33} \end{vmatrix} + \begin{vmatrix} j_{11} & j_{13} \\ j_{31} & j_{33} \end{vmatrix}, \\ \vartheta_0 &= -|J|. \end{aligned}$$

We first provide the following lemma regarding the necessary and sufficient criteria for stability around fixed point of system (2) in order to study the nature of the system around fixed point $E(x, y, z)$.

Lemma 2 (Camouzis and Ladas 2007) Suppose that $\vartheta_2, \vartheta_1, \vartheta_0 \in \mathbb{R}$. Then, the necessary and sufficient conditions for all roots μ of the equation

$$\mu^3 + \vartheta_2\mu^2 + \vartheta_1\mu + \vartheta_0 = 0$$

to satisfy $|\mu| < 1$ are

$$|\vartheta_2 + \vartheta_0| < 1 + \vartheta_1, |\vartheta_2 - 3\vartheta_0| < 3 - \vartheta_1, \text{ and } \vartheta_0^2 + \vartheta_1 - \vartheta_0\vartheta_2 < 1.$$

Now, the local dynamics of system (2) around fixed points E_0 and E_+ are as follows.

At E_0 , the Jacobian matrix $J(E_0)$ have eigenvalues $\mu_1 = 1 - b\delta, \mu_{2,3} = \frac{1}{2} \left(2 - a\delta \pm \sqrt{\delta^2(-3a^2 + 4ac)} \right)$, where $\mu_{2,3}$ satisfy the equation

$$\mu^2 - (2 - a\delta)\mu + (1 - a\delta + (a^2 - ac)\delta^2) = 0.$$

We obtain the topological classification of E_0 presented in the following Lemma.

Lemma 3 If $c < a$, the fixed point E_0 is a

- sink if (i) $-3a^2 + 4ac \geq 0, \delta < \min \left\{ \frac{2}{b}, \frac{a - \sqrt{-3a^2 + 4ac}}{a^2 - ac} \right\}$,
- (ii) $-3a^2 + 4ac < 0, \delta < \min \left\{ \frac{2}{b}, \frac{1}{a-c} \right\}$,
- source if (iii) $-3a^2 + 4ac \geq 0, \delta > \max \left\{ \frac{2}{b}, \frac{a - \sqrt{-3a^2 + 4ac}}{a^2 - ac} \right\}$,
- (iv) $-3a^2 + 4ac < 0, \delta > \max \left\{ \frac{2}{b}, \frac{1}{a-c} \right\}$,
- non-hyperbolic if (v) $-3a^2 + 4ac \geq 0, \delta = \frac{2}{b}$, or $\delta = \frac{a \pm \sqrt{-3a^2 + 4ac}}{a^2 - ac}$,
- (vi) $-3a^2 + 4ac < 0, \delta = \frac{1}{a-c}$.

Let,

$$FB_{E_0} = \left\{ (a, b, c, \delta) : \delta = \frac{a \pm \sqrt{-3a^2 + 4ac}}{a^2 - ac}, \delta \neq \frac{2}{b}, -3a^2 + 4ac \geq 0 \right\}$$

and

$$NSB_{E_0} = \left\{ (a, b, c, \delta) : \delta = \frac{1}{a-c}, -3a^2 + 4ac < 0 \right\},$$

then system (2) encounters a flip (NS) bifurcation at E_0 if parameters change in small vicinity of FB_{E_0} (NSB_{E_0}).

At E_+ , we rewrite the equation (5) as

$$P(\mu) := \mu^3 + \kappa_2\mu^2 + \kappa_1\mu + \kappa_0 = 0. \quad (6)$$

where,

$$\begin{aligned} \kappa_2 &= -3 + \delta(a + b), \\ \kappa_1 &= 3 - 2a\delta + b\delta(-2 + c\delta), \\ \kappa_0 &= -1 - 2a^2b\delta^3 + b(\delta - c\delta^2) + a(\delta + 2bc\delta^3) \end{aligned} \quad (7)$$

Following is the Lemma for stability requirement of E_+ .

Lemma 4 The fixed point E_+ of system (2) is locally asymptotically stable if and only if the coefficients $\kappa_2, \kappa_1, \kappa_0$ of (6) satisfy $|\kappa_2 + \kappa_0| < 1 + \kappa_1, |\kappa_2 - 3\kappa_0| < 3 - \kappa_1$, and $\kappa_0^2 + \kappa_1 - \kappa_0\kappa_2 < 1$.

ANALYSIS OF BIFURCATIONS

This part will focus to recapitulate the conditions for stability and direction of flip and NS bifurcations of system (2) around fixed points E_0 and E_+ by using an explicit Flip-NS bifurcation criterion without computing the eigenvalues of the respective system and bifurcation theory (Kuznetsov 2013; Wen 2005; Yao 2012). We take δ as bifurcation parameter, otherwise stated.

NS bifurcation around E_0

Suppose that parameters $(a, b, c, \delta) \in NSB_{E_0}$, then the eigenvalues of system (2) are

$$\mu_1 = 1 - b\delta, \quad \mu_{2,3} = \alpha \pm i\beta \quad (8)$$

where $\alpha = 1 - \frac{a\delta}{2}$ and $\beta = \delta\sqrt{3a^2 - 4ac}$.

Let, $\delta = \delta_{NS} = \frac{1}{a-c}$, then we have

$$|\mu_{2,3}(\delta_{NS})| = \sqrt{(1 - a\delta_{NS} + (a^2 - ac)\delta_{NS}^2)} = 1, \quad \mu_1(\delta_{NS}) = 1 - \frac{b}{a-c} \quad (9)$$

and

$$\frac{d|\mu_i(\delta)|}{d\delta} \Big|_{\delta=\delta_{NS}} = \frac{a}{2} \neq 0, i = 2, 3 \quad (10)$$

Moreover,

$$\frac{a}{a-c} \neq 2, 3 \quad (11)$$

implies that $\mu_{2,3}^k \neq 1, k = 1, 2, 3, 4$. We write the system (2) as

$$X = A(\delta)X + F \quad (12)$$

where $A(\delta) = J(E_0)$ and $F = (0, -axz\delta, xy\delta)^T$ with $\delta = \delta_{NS}$. It is possible to express the system (12) as

$$X_{n+1} = AX_n + \frac{1}{2}B(X_n, X_n) + \frac{1}{6}C(X_n, X_n, X_n) + O(X_n^4)$$

where,

$$B(x, y) = \begin{pmatrix} B_1(x, y) \\ B_2(x, y) \\ B_3(x, y) \end{pmatrix} \quad \text{and} \quad C(x, y, u) = \begin{pmatrix} C_1(x, y, u) \\ C_2(x, y, u) \\ C_3(x, y, u) \end{pmatrix} \quad (13)$$

are the symmetric multi-linear functions of $x, y, z, u \in \mathbb{R}^3$ and defined by

$$B_i(x, y) = \sum_{j,k=1}^3 \frac{\partial^2 F_i(v, \delta)}{\partial v_j \partial v_k} \Big|_{v=0} x_j y_k,$$

$$C_i(x, y, u) = \sum_{j,k,l=1}^3 \frac{\partial^3 F_i(v, \delta)}{\partial v_j \partial v_k \partial v_l} \Big|_{v=0} x_j y_k u_l.$$

In particular,

$$B(x, y) = \begin{pmatrix} 0 \\ -ax_3y_1\delta - ax_1y_3\delta \\ x_2y_1\delta + x_1y_2\delta \end{pmatrix} \quad \text{and} \quad C(x, y, u) = \begin{pmatrix} 0 \\ 0 \\ 0 \end{pmatrix} \quad (14)$$

Let $\zeta_1, \zeta_2 \in \mathbb{C}^3$ be two eigenvectors of $A(\delta_{NS})$ and $A^T(\delta_{NS})$ respectively such that

$$A(\delta_{NS})\zeta_1 = \mu_2(\delta_{NS})\zeta_1, \quad A^T(\delta_{NS})\zeta_2 = \mu_3(\delta_{NS})\zeta_2 \quad (15)$$

then after some algebraic calculation, we obtain

$$\zeta_1 = (\phi_1 + i\psi_1, 1, 0)^T \quad \text{and} \quad \zeta_2 = (\phi_2 + i\psi_2, 1, 0)^T$$

with $\phi_1 = \frac{a\delta}{2(a-c)\delta}, \psi_1 = \frac{-\beta}{2(a-c)\delta}$ and $\phi_2 = \frac{-a\delta}{2a\delta}, \psi_2 = \frac{-\beta}{2a\delta}$.

The standard inner product property $\langle \zeta_1, \zeta_2 \rangle = \sum_{i=1}^3 \zeta_{1i} \bar{\zeta}_{2i}$ is applied to set the normalized vector $\bar{\zeta}_2 = \zeta \zeta_2$ so that $\langle \zeta_1, \bar{\zeta}_2 \rangle = 1$ is obtained where $\zeta = \zeta_1 + i\zeta_2$ with

$$\bar{\zeta}_1 = \frac{\phi_1\phi_2 + \psi_1\psi_2 + 1}{(\phi_1\phi_2 + \psi_1\psi_2 + 1)^2 + (\phi_2\psi_1 - \phi_1\psi_2)^2},$$

$$\bar{\zeta}_2 = \frac{\phi_2\psi_1 - \phi_1\psi_2}{(\phi_1\phi_2 + \psi_1\psi_2 + 1)^2 + (\phi_2\psi_1 - \phi_1\psi_2)^2}.$$

Now, decomposing the vector $X \in \mathbb{R}^3$ as $X = z\zeta_1 + \bar{z}\bar{\zeta}_1$ by considering δ vary near to δ_{NS} and for $z \in \mathbb{C}$. Obviously, $z = \langle \zeta_2, X \rangle$. So, we derive the transformed form of system (12) for $|\delta|$ close to δ_{NS} as follows:

$$z \mapsto \mu(\delta)z + \hat{g}(z, \bar{z}, \delta) \quad (16)$$

where $\mu(\delta) = (1 + \hat{\varphi}(\delta))e^{i\theta(\delta)}$ with $\hat{\varphi}(\delta_{NS}) = 0$ and $\hat{g}(z, \bar{z}, \delta)$ is a smooth complex-valued function. Then we obtain

$$\hat{g}(z, \bar{z}, \delta) = \sum_{k+l \geq 2} \frac{1}{k!l!} \hat{g}_{kl}(\delta) z^k \bar{z}^l \quad \text{with} \quad \hat{g}_{kl} \in \mathbb{C}, k, l = 0, 1, \dots$$

The coefficients \hat{g}_{kl} are determined via multilinear symmetric vector functions:

$$\begin{aligned} \hat{g}_{20}(\delta) &= \langle \zeta_2, B(\zeta_1, \zeta_1) \rangle, \quad \hat{g}_{11}(\delta) = \langle \zeta_2, B(\zeta_1, \bar{\zeta}_1) \rangle, \\ \hat{g}_{02}(\delta) &= \langle \zeta_2, B(\bar{\zeta}_1, \bar{\zeta}_1) \rangle, \\ \hat{g}_{21}(\delta) &= \langle \zeta_2, C(\zeta_1, \zeta_1, \bar{\zeta}_1) \rangle + 2 \langle \zeta_2, B(\zeta_1, (I_n - A)^{-1} B(\zeta_1, \bar{\zeta}_1)) \rangle \\ &\quad + \langle \zeta_2, B(\bar{\zeta}_1, (\mu_2^2 I_n - A)^{-1} B(\zeta_1, \zeta_1)) \rangle + \frac{(1-2\mu_2)\mu_3}{1-\mu_2} \hat{g}_{20} \hat{g}_{11} \\ &\quad + \frac{2}{1-\mu_2} |\hat{g}_{11}|^2 + \frac{\mu_2}{\mu_2-1} |\hat{g}_{02}|^2. \end{aligned} \quad (17)$$

with $\delta = \delta_{NS}$.

After some tedious calculation, we get

$$\begin{aligned} \hat{g}_{20}(\delta_{NS}) &= 0, \quad \hat{g}_{11}(\delta_{NS}) = 0, \quad \hat{g}_{02}(\delta_{NS}) = 0, \\ \hat{g}_{21}(\delta_{NS}) &= \frac{-2a\delta_{NS}}{b(\Phi_4^2 + \Psi_4^2)} [(\Phi_3\Phi_4 + \Psi_3\Psi_4) + i(\Phi_4\Psi_3 - \Phi_3\Psi_4)] \end{aligned} \quad (18)$$

where

$$\begin{aligned} \Phi_4 &= -1 + \alpha^2 - \beta^2 + b\delta, \\ \Psi_4 &= 2\alpha\beta, \\ \Phi_3 &= \Phi_1\Phi_2 - \Psi_1\Psi_2, \\ \Psi_3 &= \Phi_2\Psi_1 + \Phi_1\Psi_2, \\ \Phi_2 &= \phi_1(-2 + 2\alpha^2 - 2\beta^2 + 3b\delta), \\ \Psi_2 &= 4\phi_1\alpha\beta - b\psi_1\delta, \\ \Phi_1 &= \phi_1\bar{\zeta}_1 + \psi_1\bar{\zeta}_2, \\ \Psi_1 &= \psi_1\bar{\zeta}_1 - \phi_1\bar{\zeta}_2. \end{aligned}$$

Then using coefficient of the critical normal form

$$l_1(\delta_{NS}) = \text{Re} \left(\frac{\mu_3 \hat{g}_{21}}{2} \right) - \text{Re} \left(\frac{(1-2\mu_2)\mu_3^2}{2(1-\mu_2)} \hat{g}_{20} \hat{g}_{11} \right) - \frac{1}{2} |\hat{g}_{11}|^2 - \frac{1}{4} |\hat{g}_{02}|^2 \quad (19)$$

we obtain $l_1(\delta_{NS}) = \frac{-a\delta_{NS}}{b(\Phi_4^2 + \Psi_4^2)} (\Phi_6\Phi_4 + \Psi_6\Psi_4)$ where

$$\begin{aligned} \Phi_5 &= \alpha\Phi_1 + \beta\Psi_1, \\ \Psi_5 &= \alpha\Psi_1 - \beta\Phi_1, \\ \Phi_6 &= \Phi_2\Phi_5 - \Psi_2\Psi_5, \\ \Psi_6 &= \Phi_2\Psi_5 + \Phi_5\Psi_2. \end{aligned}$$

The following theorem can be used in conjunction with the preceding description to demonstrate the direction and stability of the NS bifurcation.

Theorem 1 Suppose (11) holds and $l_1(\delta_{NS}) \neq 0$, then NS bifurcation emerges at fixed point $E_0(0, 0, 0)$ for system (2) if the δ changes its value in small neighbourhood of NSB_{E_0} . Additionally, there exists an attractive (resp. repelling) smooth closed invariant curve bifurcate from E_+ if $l_1(\delta_{NS}) < 0$ (resp. $l_1(\delta_{NS}) > 0$) and the bifurcation is sub-critical (resp. super-critical).

Bifurcation Analysis around E_+

Flip Bifurcation: Existence condition To investigate the existence of flip bifurcation, we will use Lemma in (Yao 2012).

Lemma 5 The flip bifurcation of system (2) takes place around fixed point $E_+ = \left(\sqrt{\frac{b}{a}(c-a)}, \sqrt{\frac{b}{a}(c-a)}, \frac{c-a}{a} \right)$ at $\delta = \delta_F$ if and only if

$$\begin{aligned} 1 - \kappa_1 + \kappa_0(\kappa_2 - \kappa_0) &> 0, \\ 1 + \kappa_1 - \kappa_0(\kappa_2 + \kappa_0) &> 0, \\ 1 + \kappa_2 + \kappa_1 + \kappa_0 &> 0, \\ 1 - \kappa_2 + \kappa_1 - \kappa_0 &= 0, \\ 1 + \kappa_0 &> 0, \\ 1 - \kappa_0 &> 0, \end{aligned}$$

$$\text{and} \quad \frac{\sum_{i=1}^n (-1)^{n-i} i'_i}{\sum_{i=1}^n (-1)^{n-i} (n-i+1)_{i-1}} = \frac{\kappa'_2 - \kappa'_1 + \kappa'_0}{3 - 2\kappa_2 + \kappa_1} \neq 0,$$

where $\kappa_2, \kappa_1, \kappa_0$ are given as in (7) and $\kappa'_i = \frac{d\kappa_i}{d\delta} \Big|_{\delta=\delta_F}$ with

$$\delta_F = \frac{-c}{3a^2-3ac} + \frac{6a^3+6a^2(b-c)-6abc+bc^2}{3a(a-c)\Gamma_1} + \frac{\Gamma_1}{3ab(a-c)},$$

$$\Gamma_1 = \sqrt[3]{-54a^4b^2 + 99a^3b^2c + 9ab^3c^2 - b^3c^3 - 9a^2b^2c(b+5c) + 3\sqrt{3}\sqrt{\Gamma_2}},$$

$$\Gamma_2 = -a^2b^3(a-c)^2(8a^5 + b^2(b-4c)c^2 - 4a^4(21b+2c) + 12a^3b(2b+13c) + \Gamma_3),$$

$$\Gamma_3 = 2ab^2c(-4b+19c) + a^2b(8b^2 - 60bc - 71c^2).$$

Define the set

$$FB_{E_+} = \{(a, b, c, \delta) : \delta = \delta_F, a, b, c > 0\}.$$

If system parameters value vary in a small vicinity of FB_{E_+} , one of the eigenvalue of (6) is $\mu_3(\delta_F) = -1$ and other two are $|\mu_{1,2}(\delta_F)| \neq \pm 1$, and then system (2) underlies a flip bifurcation around E_+ .

Flip Bifurcation: Direction and Stability We choose parameter $(a, b, c, \delta) \in FB_{E_+}$ and let $\delta = \delta_F$, then the eigenvalues of $J(E_+)$ are:

$$\mu_1(\delta_F) = -1, \quad |\mu_i(\delta_F)| \neq \pm 1, i = 2, 3 \quad (20)$$

Next, we set $\hat{x} = x - x^+, \hat{y} = y - y^+, \hat{z} = z - z^+, A(\delta_F) = J(E_+)$ and transfer the fixed point E_+ of system (2) to the origin. Since symmetric multi-linear functions are not associated with fixed point, the bi-linear and trilinear functions for flip bifurcation will remain unchanged as in (14).

Consider two eigenvectors $\eta_1, \eta_2 \in \mathbb{R}^3$ of A for eigenvalue $\mu_1(\delta_F) = -1$ such that

$$A(\delta_F)\eta_1 = -\eta_1, \quad A^T(\delta_F)\eta_2 = -\eta_2, \quad \langle \eta_2, \eta_1 \rangle = 1.$$

Then the coefficient of normal form is

$$l_2(\delta_F) = \frac{1}{6} \langle \eta_2, C(\eta_1, \eta_1, \eta_1) \rangle - \frac{1}{2} \langle \eta_2, B(\eta_1, (A-I)^{-1}B(\eta_1, \eta_1)) \rangle \quad (21)$$

In light of the aforementioned investigation, we provide the following conclusion with regard to the stability and direction of the flip bifurcation.

Theorem 2 Suppose (20) holds well and $l_2(\delta_F) \neq 0$ for the fixed point $E_+(x^+, y^+, z^+)$. Then the system (2) encounters a flip bifurcation at E_+ if $l_2(\delta_F) \neq 0$ and δ fluctuates its value in a limited proximity of bifurcation point. Moreover, stable (resp., unstable) period-2 orbits split off from E_+ if $l_2(\delta_F)$ is positive (resp., negative).

NS Bifurcation: Existence condition We will use the explicit Flip-NS bifurcation criterion (Wen 2005; Yao 2012) for the existence of NS bifurcation and the subsequent lemma will give the necessary and sufficient parametric conditions for which system (2) underlies NS bifurcation if bifurcation parameter δ passes its critical value.

Lemma 6 The NS bifurcation of system (2) occurs around the fixed point E_+ at $\delta = \delta_{NS_+}$ if and only if

$$\begin{aligned} 1 - \kappa_1 + \kappa_0(\kappa_2 - \kappa_0) &= 0, \\ 1 + \kappa_1 - \kappa_0(\kappa_2 + \kappa_0) &> 0, \\ 1 + \kappa_2 + \kappa_1 + \kappa_0 &> 0, \\ 1 - \kappa_2 + \kappa_1 - \kappa_0 &> 0, \\ \frac{d}{d\delta} (1 - \kappa_1 + \kappa_0(\kappa_2 - \kappa_0))_{\delta=\delta_{NS_+}} &\neq 0, \end{aligned}$$

$$\text{and } \cos\left(\frac{2\pi}{l}\right) \neq 1 - \frac{1+\kappa_2+\kappa_1+\kappa_0}{2(1+\kappa_0)}, l = 3, 4, 5, \dots$$

where $\kappa_2, \kappa_1, \kappa_0$ are given as in (7) with

$$\delta_{NS_+} = \frac{1}{48a^2b(a-c)^2} \left(\frac{16abc(-a-c) - (8a^2b(a-c))^2(6a^3+6a^2(b-c)-6abc+bc^2)}{\Lambda_1} - 8\Lambda_1 \right),$$

$$\Lambda_1 = \sqrt[3]{\Lambda_2 + \Lambda_3 + 3\sqrt{3}\sqrt{\Lambda_4}},$$

$$\Lambda_2 = -54a^10b^2 + 261a^9b^2c - 12a^4b^3c^5 + a^3b^3c^6 + 3a^5b^2c^4(13b + 15c),$$

$$\Lambda_3 = 18a^7b^2c^2(2b + 27c) - 9a^8b^2c(b + 56c) - a^6b^2c^3(55b + 234c),$$

$$\Lambda_4 = -a^8b^3(a-c)^8(8a^5 + b^2(b-4c)c^2 - 4a^4(21b+2c) + 12a^3b(2b+13c) + \Lambda_5),$$

$$\Lambda_5 = 2ab^2c(-4b+19c) + a^2b(8b^2 - 60bc - 71c^2).$$

Set

$$NSB_{E_+} = \{(a, b, c, \delta) : \delta = \delta_{NS_+}, a, b, c > 0\},$$

and for parameter perturbation in a small neighborhood of NSB_{E_+} , two roots (eigenvalues) of (6) are complex conjugate having modulus one and the magnitude of other root is not equal to one, then the system (2) experiences NS bifurcation around E_+ .

NS Bifurcation: Direction and Stability This section will present the direction of NS bifurcation. We choose the fixed point E_+ of system (2) with arbitrary parameter $(a, b, c, \delta) \in NSB_{E_+}$. Let, $\delta = \delta_{NS_+}$, then the matrix $J(E_+)$ has the eigenvalues satisfying

$$|\mu_i(\delta_{NS_+})| = 1, i = 2, 3 \quad (22)$$

and $\mu_1(\delta_{NS_+}) \neq 1$.

For eigenvalues $\mu_2(\delta_{NS_+})$ and $\mu_3(\delta_{NS_+})$, let $\tau_1, \tau_2 \in \mathbb{C}^3$ be two eigenvectors of $A(\delta_{NS_+})$ and $A^T(\delta_{NS_+})$ respectively such that

$$A(\delta_{NS_+})\tau_1 = \mu_2(\delta_{NS_+})\tau_1, A^T(\delta_{NS_+})\tau_2 = \mu_3(\delta_{NS_+})\tau_2, \quad (23)$$

$$\langle \tau_2, \tau_1 \rangle = \sum_{i=1}^3 \bar{\tau}_{2i}\tau_{1i} = 1$$

The coefficient $l_3(\delta_{NS_+})$ calculated by (19) presents the direction and stability of NS bifurcation which has been stated in the following theorem.

Theorem 3 Suppose (22) holds and $l_3(\delta_{NS_+}) \neq 0$ for the fixed point E_+ . Then system (2) encounters NS bifurcation at E_+ if the δ fluctuates its value in a limited vicinity of NSB_{E_+} . Moreover, if $l_3(\delta_{NS_+}) < 0$ (resp. $l_3(\delta_{NS_+}) > 0$), a singular invariant closed curve bifurcates from E_+ that is attracting (resp., repelling) and the bifurcation is sub-critical (resp. super-critical).

NUMERICAL SIMULATIONS

Using numerical simulations with the aid of bifurcation diagrams, phase portraits, and MLEs, we will confirm our theoretical conclusions for the system (2) in this section. The presence of chaos has been supported by the 0-1 test algorithm. For the investigations of bifurcations, we will take different set of parameter values.

Example 1 We take parameter values $a = 18, b = 12, c = 10$ and $0.1 \leq \delta \leq 0.1317$. By calculation, we find a fixed point $E_0 = (0, 0, 0)$ of system (2) and the bifurcation point is obtained as $\delta_{NS} = 0.125$. The Jacobian matrix J evaluated at E_0 have eigenvalues $\mu_1 = -0.5$ and $\mu_{2,3} = -0.125 \pm 0.9921575i$ with $|\mu_{2,3}| = 1$.

Furthermore,

$$\frac{d|\mu_i(\delta)|}{d\delta} \Big|_{\delta=\delta_{NS}} = \frac{a}{2} = 9 \neq 0, i = 2, 3,$$

$$\frac{a}{a-c} = \frac{9}{4} \neq 2, 3.$$

So, the criterion for the existence of NS bifurcation are fulfilled with $(a, b, c, \delta) \in NSB_{E_0}$. This confirms the correctness of Lemma 3. Therefore, a NS bifurcation occurs around fixed point E_0 if δ crosses its critical value δ_{NS} .

Let $\zeta_1, \zeta_2 \in \mathbb{C}^3$ be two complex eigenvectors of $A(\delta_{NS})$ and $A^T(\delta_{NS})$ corresponding to $\mu_{2,3}$, respectively. Therefore,

$$\zeta_1 \sim (1.125 - 0.992157i, 1, 0)^T, \zeta_2 \sim (-0.5 - 0.440959i, 1, 0)^T.$$

For $\langle \zeta_1, \zeta_2 \rangle = 1$, we can take normalized vector as $\zeta_2 = \gamma \zeta_2$ where, $\gamma = 0.5 + 0.566947i$. Then

$$\zeta_1 \sim (1.125 - 0.992157i, 1, 0)^T, \zeta_2 \sim (-0.503953i, 0.5 + 0.566947i, 0)^T.$$

Also by (18) the Taylor coefficients are, $\hat{g}_{20} = 0$, $\hat{g}_{11} = 0$, $\hat{g}_{02} = 0$, $\hat{g}_{21} = 0.421875 - 0.797269i$.

From (19), we obtain the Lyapunov coefficient $l_2(\delta_{NS}) = -0.421875 < 0$. As a result, the NS bifurcation is super-critical and the Theorem 1 conditions are satisfied.

The NS bifurcation diagrams are displayed in Figure 1 (a) which reveal that the condition of stability for the positive fixed point E_0 occurs when $\delta < \delta_{NS}$, loses its stability at $\delta = \delta_{NS}$ and there appears an attracting closed invariant curve when $\delta > \delta_{NS}$. The MLEs related to Figure 1 (a) are shown in Figure 1 (b). The non stability of system dynamics are justified with the sign of MLEs.

The phase portraits of system (2) that correspond to the bifurcation diagram in Figure 1 (a) are plotted in Figure 2, explicitly illuminating the mechanism by which an invariant smooth closed curve splits from a stable fixed point E_0 when δ varies close to its critical value. We noticed that NS bifurcations occurs at $\delta = \delta_{NS}$ (see in Figure 2(b)). When $\delta > \delta_{NS}$, there appears an invariant closed curve and further increasing of δ , NS bifurcation instigate a route to chaos.

Example 2 We take $a = 5.2, b = 13.5, c = 6.5, 0.14 \leq \delta \leq 0.1636$. We obtain $E_+ = (1.83712, 1.83712, 0.25)$ and bifurcation point $\delta_F = 0.1533$. At $\delta = \delta_F$, the Jacobian matrix of system (2) takes the form

$$A(\delta_F) = \begin{pmatrix} 0.202839 & 0.797161 & 0 \\ 0 & 1 & -1.46448 \\ 0.28163 & 0.28163 & -1.06955 \end{pmatrix}.$$

and the eigenvalues of $A(\delta_F)$ are $\mu_1 = -1$ and $\mu_{2,3} = 0.566644 \pm 0.375479i$ with $|\mu_{2,3}| = 0.679757$. Moreover,

$$\begin{aligned} 1 - \kappa_1 + \kappa_0 (\kappa_2 - \kappa_0) &= 1.39612 > 0, \\ 1 + \kappa_1 - \kappa_0 (\kappa_2 + \kappa_0) &= 0.176862 > 0, \\ 1 + \kappa_2 + \kappa_1 + \kappa_0 &= 0.657564 > 0, \\ 1 - \kappa_2 + \kappa_1 - \kappa_0 &= 0, \\ 1 + \kappa_0 &= 1.46207 > 0, \\ 1 - \kappa_0 &= 0.53793 > 0, \end{aligned}$$

$$\text{and } \frac{\kappa_2 - \kappa_1 + \kappa_0'}{3 - 2\kappa_2 + \kappa_1} = 13.0463 \neq 0$$

This shows that all requirements of Lemma 5 are validated with $(a, b, c, \delta) \in FB_{E_+}$. Thus, the requirement for flip bifurcation's existence is confirmed and system (2) experience a flip bifurcation around E_+ at $\delta = \delta_F$.

Next, let the two eigenvectors of $A(\delta_F)$ corresponding to $\mu_1(\delta_F) = -1$, be $\eta_1, \eta_2 \in \mathbb{R}^3$ respectively. Then, we obtain

$$\eta_1 \sim (-0.364586, 0.550125, 0.7512923)^T, \eta_2 \sim (-0.227729, -0.0461924, 0.972628)^T.$$

To set $\langle \eta_1, \eta_2 \rangle = 1$, we can choose normalized vector as $\eta_2 = \gamma \zeta_2$ where, $\gamma = 1.26848$. Therefore,

$$\eta_1 \sim (-0.364586, 0.550125, 0.751292)^T, \eta_2 \sim (-0.288871, -0.0585943, 1.23376)^T.$$

Then from (21), the Lyapunov coefficient $l_2(\delta_F) = 0.0397406 > 0$ is obtained. This guarantees the appropriateness of Theorem 2.

The diagrams of bifurcation shown in Figure 3 (a) express the stability of fixed point E_+ when δ crosses bifurcation point. The MLEs and phase portraits of system (2) associated with Figure 3 (a) are shown in Figure 3 (b) and Figure 4 respectively which explicitly illustrate the mechanism of how period doubling phenomena leads to chaos.

Example 3 We choose $0.06 \leq \delta \leq 0.11, a = 12, b = 12, c = 18$. Then we find a fixed point $E_+ = (2.44949, 2.44949, 0.5)$ of system (2) and the bifurcation point is obtained as $\delta_{NS_+} = 0.0671545$. The Jacobian matrix is evaluated at E_+ is

$$A(\delta_{NS}) = \begin{pmatrix} 0.194146 & 0.805854 & 0 \\ 0 & 1 & -1.97393 \\ 0.164494 & 0.164494 & 0.194146 \end{pmatrix},$$

and the eigenvalues of $A(\delta_{NS})$ are $\mu_1 = -0.16093$ and $\mu_{2,3} = 0.77461 \pm 0.632439i$ with $|\mu_{2,3}| = 1$.

Furthermore,

$$\begin{aligned} 1 - \kappa_1 + \kappa_0 (\kappa_2 - \kappa_0) &= 0, \\ 1 + \kappa_1 - \kappa_0 (\kappa_2 + \kappa_0) &= 1.9482 > 0, \\ 1 + \kappa_2 + \kappa_1 + \kappa_0 &= 0.523323 > 0, \\ 1 - \kappa_2 + \kappa_1 - \kappa_0 &= 2.97805 > 0, \\ \frac{d}{d\delta} (1 - \kappa_1 + \kappa_0 (\kappa_2 - \kappa_0)) &= -8.55995 \neq 0 \end{aligned}$$

and

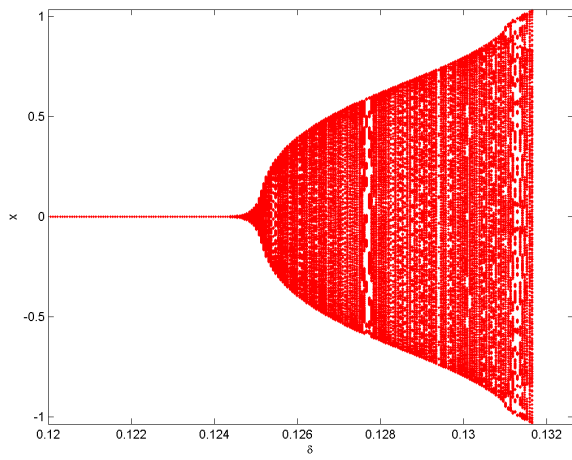
$$1 - \frac{1 + \kappa_2 + \kappa_1 + \kappa_0}{2(1 + \kappa_0)} = 0.77461.$$

From the resonance condition $\cos\left(\frac{2\pi}{l}\right) = 0.77461$, we get $l = \pm 9.17659$.

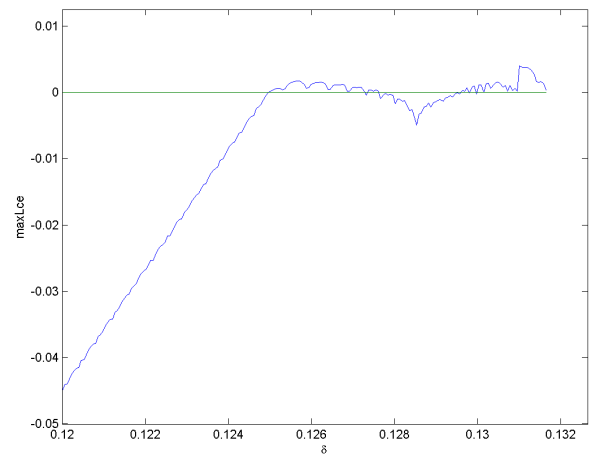
So, the criterion for the existence of NS bifurcation are fulfilled with $(a, b, c, \delta) \in NSB_{E_+}$. This confirms the correctness of Lemma 6. Therefore, a NS bifurcation occurs around fixed point E_+ if δ crosses its critical value δ_{NS_+} .

Let $\tau_1, \tau_2 \in \mathbb{C}^3$ be two complex eigenvectors of $A(\delta_{NS})$ and $A^T(\delta_{NS})$ corresponding to $\mu_{2,3}$, respectively. Therefore,

$$\tau_1 \sim (0.449192 - 0.489412i, 0.70765, 0.0808016 - 0.226728i)^T, \tau_2 \sim (0.117028 + 0.127506i, -0.265599 + 0.28938i, 0.903196)^T.$$

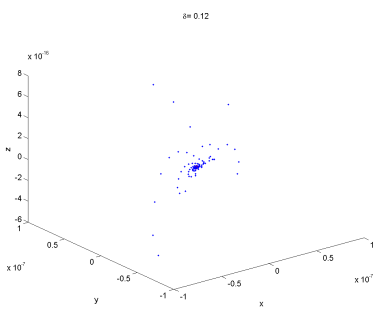


(a)

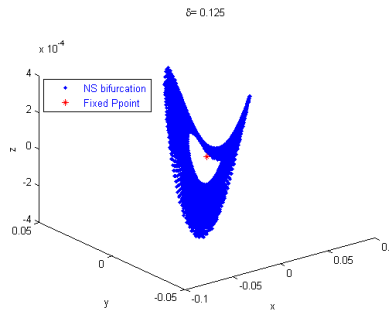


(b)

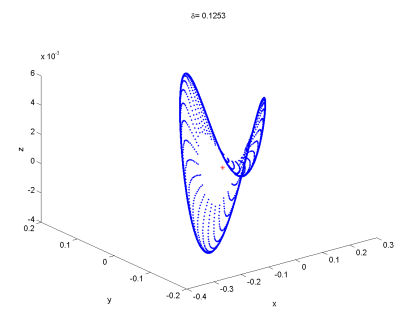
Figure 1 NS Bifurcation Diagram: in (a) (δ, x) plane, (b) MLEs, $(x_0, y_0, z_0) = (0.93, 0.93, 0.33)$.



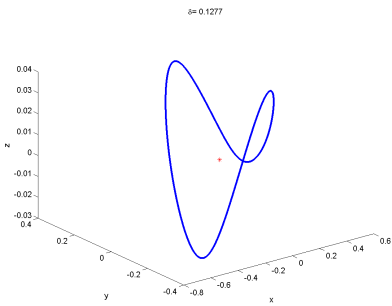
(a)



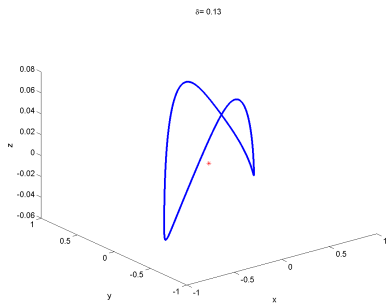
(b)



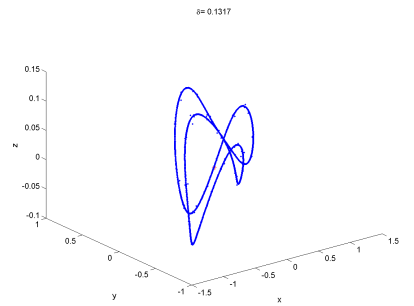
(c)



(d)

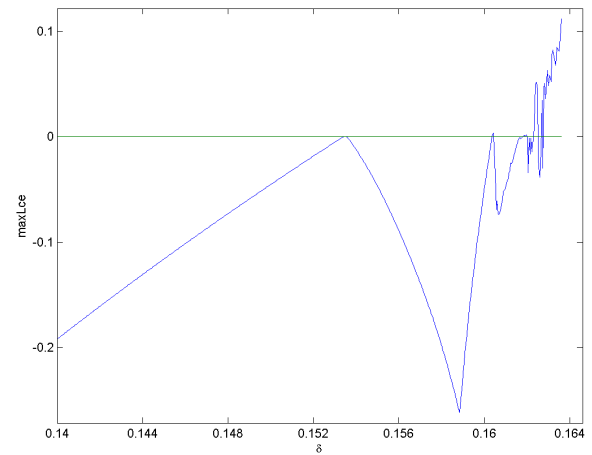
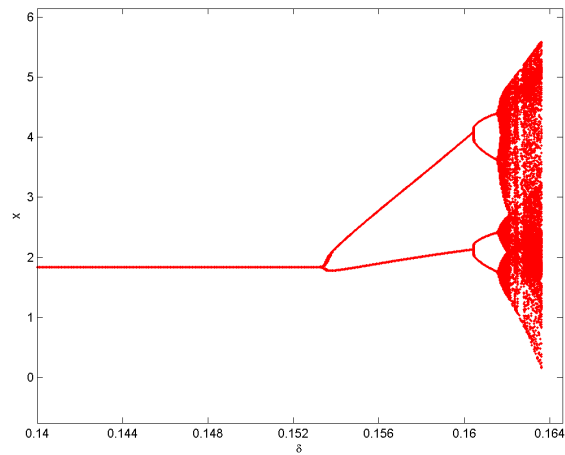


(e)



(f)

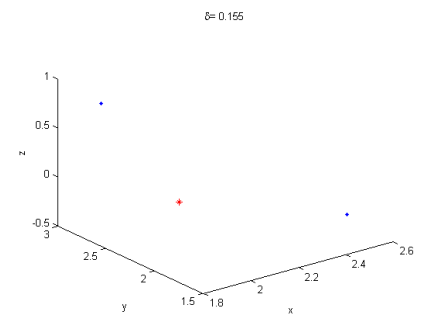
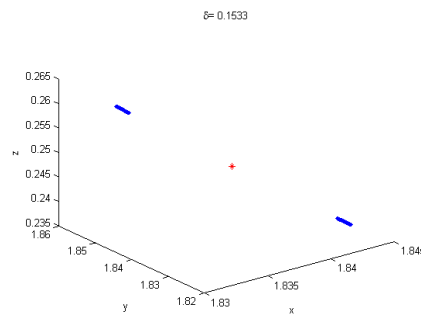
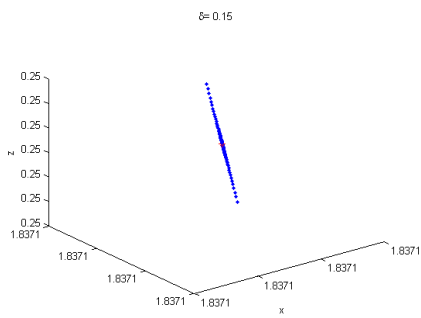
Figure 2 Phase portrait for different values of δ connected to Figure 1 a. Red * is the fixed point E_+ .



(a)

(b)

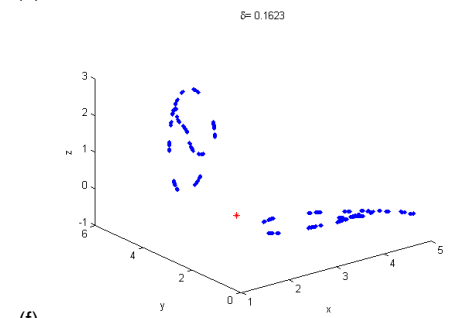
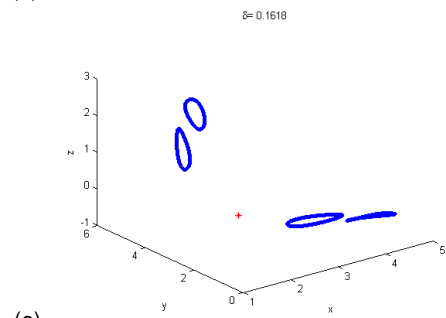
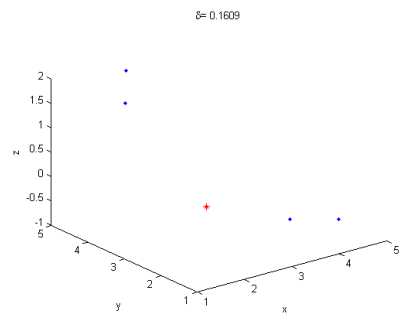
Figure 3 Flip Bifurcation Diagram: in (a) (δ, x) plane, (b) MLEs, $(x_0, y_0, z_0) = (0.93, 0.93, 0.33)$.



(a)

(b)

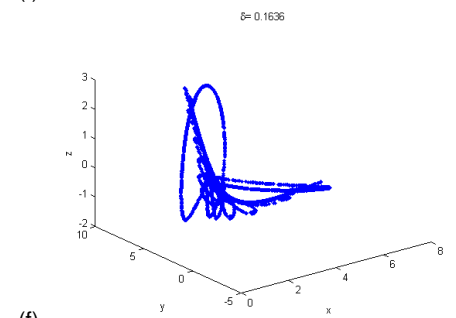
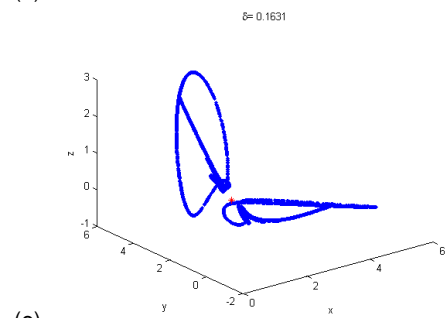
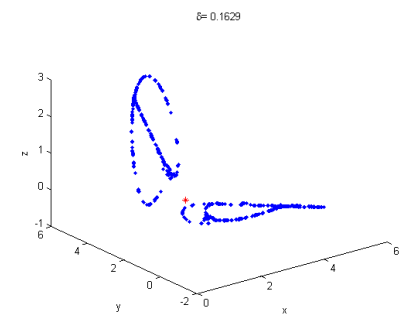
(c)



(d)

(e)

(f)



(d)

(e)

(f)

Figure 4 Phase portrait for different values of δ associated to Figure 3 a. Red * is the fixed point E_+ .

For $\langle \tau_1, \tau_2 \rangle = 1$, we can take normalized vector as $\tau_2 = \gamma \tau_1$ where, $\gamma = -0.429971 - 1.80561i$. Then

$$\begin{aligned} \tau_1 &\sim (0.449192 - 0.489412i, 0.70765, 0.0808016 - \\ &0.226728i)^T, \tau_2 \sim (0.179908 - 0.266131i, 0.636707 + \\ &0.355143i, -0.388348 - 1.63082i)^T. \end{aligned}$$

Also by (17) the Taylor coefficients are, $\hat{g}_{20} = 0.216831 + 0.190042i$, $\hat{g}_{11} = -0.167694 + 0.153913i$, $\hat{g}_{02} = -0.0967446 - 0.136271i$, $\hat{g}_{21} = 0.074238 - 0.170412i$.

From (19), we obtain the Lyapunov coefficient $l_2(\delta_{NS}) = -0.094591 < 0$. Therefore, the NS bifurcation is super-critical and the requirements of Theorem 3 are established.

The NS bifurcation diagrams are displayed in Figure 5 (a) which reveal that the condition of stability for the positive fixed point E_+ occurs when $\delta < \delta_{NS}$, loses its stability at $\delta = \delta_{NS}$ and there appears an attracting closed invariant curve when $\delta > \delta_{NS}$. The MLEs related to Figure 5 (a) are shown in Figure 5 (b). The non stability of system dynamics are justified with the sign of MLEs.

The phase portraits of system (2) corresponding to diagram of bifurcation shown in Figure 5 (a) are plotted in Figure 6. This figure explicitly illustrate the mechanism of how an invariant smooth closed curve bifurcates from stable fixed point E_+ when δ changes near its critical value. We noticed that NS bifurcations occurs at $\delta = \delta_{NS}$ (see in Figure 6(b)). When $\delta > \delta_{NS}$, there appears an invariant closed curve and further increasing of δ , NS bifurcation instigate a route to chaos.

Example 4 Taking parameter values $11.63 \leq a \leq 14.5, 10 \leq c \leq 20.5, b = 12, c = 18, \delta = 0.1057$, the two-dimensional parametric space is depicted in Figure 7(a) which shows critical value curves of NS bifurcation of system (2) in (a, c) plane and regions of stability. It may help one to choose parameter values to see how do dynamics of the system change its topological properties. Varying two parameters, multiple bifurcation diagrams of system (2) are plotted in Figure 7(c) together with the sign of MLEs presented in Figure 7(b). We notice that the growth of parameter c delays NS bifurcation.

In particular, for $c = 18$ the NS bifurcation of system (2) takes place at $a_{NS} = 13.999$ around fixed point $E_+ = (1.85193, 1.85193, 0.285803)$. The bifurcation diagram of system (2) with MLEs are plotted in Figure 8 (a,b). The Lyapunov coefficient $l_3(a_{NS}) = -0.543329 < 0$ results that the NS bifurcation is super-critical. The phase portraits of system (2) in Figure 9 reflect the break down of invariant closed curve, a period of 9, 11 orbits and attracting chaotic set.

0-1 test algorithm for chaos

The 0 – 1 test algorithm (Gottwald and Melbourne 2004; Xin and Li 2013; Xin and Wu 2015) returns a real number $K \in [0, 1]$ and a graph in 2D new coordinates (u, v) -plane.

Let $\hat{\Phi}(n)$ be finely sampled set of measurement data, where $n = 1, 2, 3, \dots, N_{tot}$ and N_{tot} is length of data. The test steps are as follows.

Step 1: Take a random real number $d \in \left(\frac{\pi}{5}, \frac{4\pi}{5}\right)$, and define new coordinates $(u_d(n), v_d(n))$ as follows.

$$\begin{aligned} u_d(n) &= \sum_{j=1}^n \hat{\Phi}(j) \cos(\hat{\theta}(j)) \\ v_d(n) &= \sum_{j=1}^n \hat{\Phi}(j) \sin(\hat{\theta}(j)) \end{aligned} \quad (24)$$

where

$$\hat{\theta}(j) = jd + \sum_{i=1}^j \hat{\Phi}(i), \quad j = 1, 2, 3, \dots, n$$

Step 2: Define the quantity $SD_d(n)$ called mean square displacement as follows:

$$SD_d(n) = \lim_{N_{tot} \rightarrow \infty} \frac{1}{N_{tot}} \sum_{j=1}^{N_{tot}} (u_d(j+n) - u_d(j))^2 + (v_d(j+n) - v_d(j))^2, \quad (25)$$

$$n \in \left[1, \frac{N_{tot}}{10}\right]$$

Step 3: Define the quantity $MSD_d(n)$ called modified mean square displacement as follows:

$$MSD_d(n) = SD_d(n) - \left(\lim_{N_{tot} \rightarrow \infty} \frac{1}{N_{tot}} \sum_{j=1}^{N_{tot}} \hat{\Phi}(j) \right)^2 \frac{1 - \cos nc}{1 - \cos c} \quad (26)$$

Step 4: Define the median value of correlation coefficient K as follows:

$$K = \text{median}(\kappa_c) \quad (27)$$

where

$$\kappa_c = \frac{\text{cov}(\Omega_1, \Omega_2)}{\sqrt{\text{var}(\Omega_1)\text{var}(\Omega_2)}} \in [-1, 1]$$

with vectors $\Omega_1 = (1, 2, 3, \dots, n_{cut})$, $\Omega_2 = (MSD_d(1), MSD_d(2), MSD_d(3), \dots, MSD_d(n_{cut}))$, $n_{cut} = \text{round}\left(\frac{N_{tot}}{10}\right)$. For the vectors p, s of length n_t , the covariance and variance are defined as follows:

$$\text{cov}(p, s) = \frac{1}{n_t} \sum_{j=1}^{n_t} (p(j) - \bar{p})(s(j) - \bar{s})$$

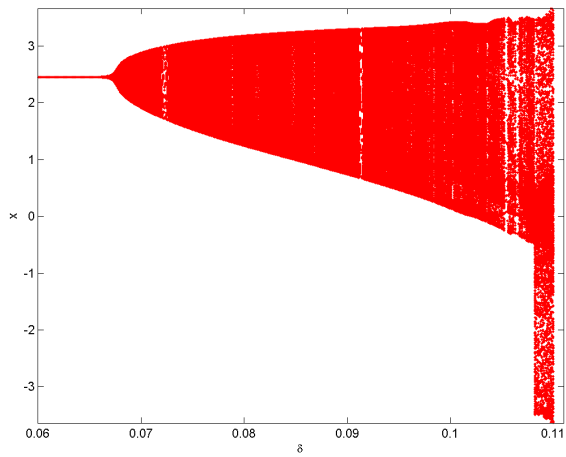
$$\bar{p} = \frac{1}{n_t} \sum_{j=1}^{n_t} p(j)$$

$$\text{var}(p) = \text{cov}(p, p)$$

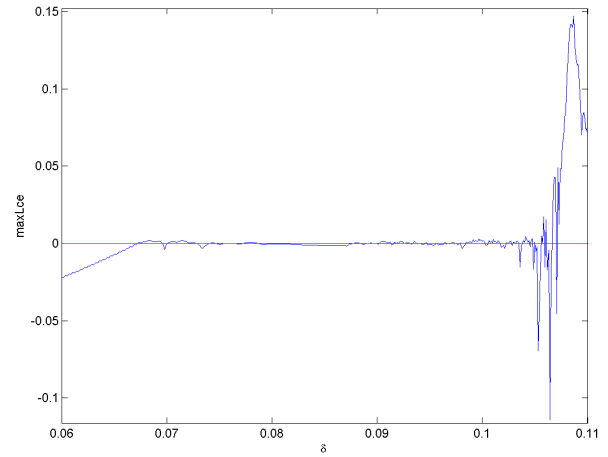
Step 5: Use the test outputs' interpretation as follows:

- (i) $K \approx 0$ suggests that the dynamics of observed data are regular (i.e., periodic or quasi-periodic), whereas $K \approx 1$ suggests that the dynamics of recorded data are chaotic.
- (ii) Bounded trajectories in the new coordinate system (p, s) denote regular underlying dynamics, while Brownian-like (unbounded) trajectories denote chaotic underlying dynamics.

Example 5 The chaotic dynamics (see Figure 9 (a)) of the system (2) are quantified with correlation coefficient value $K = 0.97639$ by 0 – 1 test for chaos and the plot in transformed coordinates (p, s) (see Figure 10(b)) showing Brownian-like trajectories. The diagram of correlation coefficient value K is displayed in Figure 10(a) which guarantees that decreasing the values of parameter a causes unstable system dynamics for discrete T system.



(a)



(b)

Figure 5 NS Bifurcation diagram: in (a) (δ, x) plane, (b) MLEs, $(x_0, y_0, z_0) = (0.98, 0.98, 0.6)$.

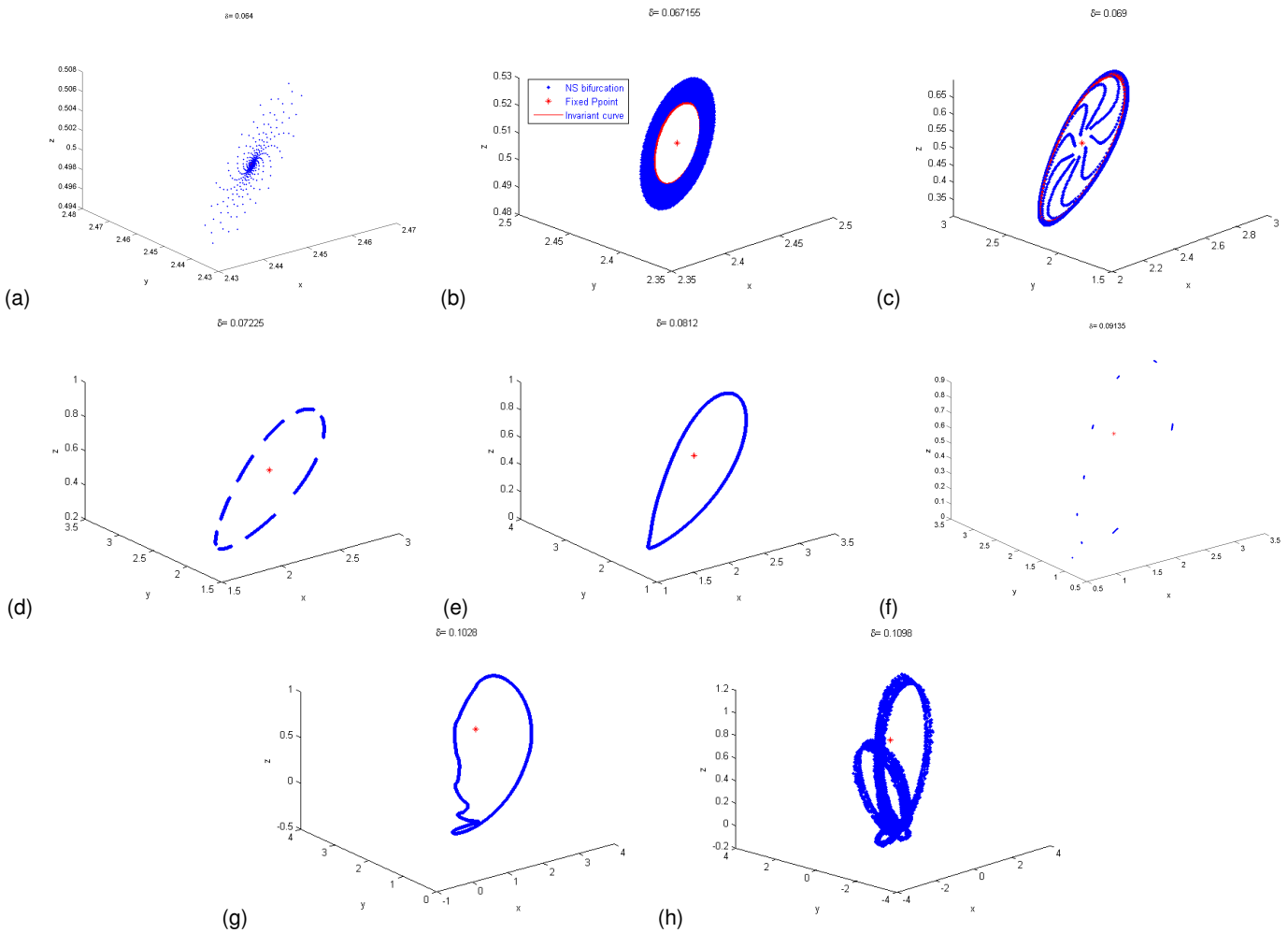


Figure 6 Phase portrait for different values of δ corresponding to Figure 5 a. Red $*$ is the fixed point E_+ .

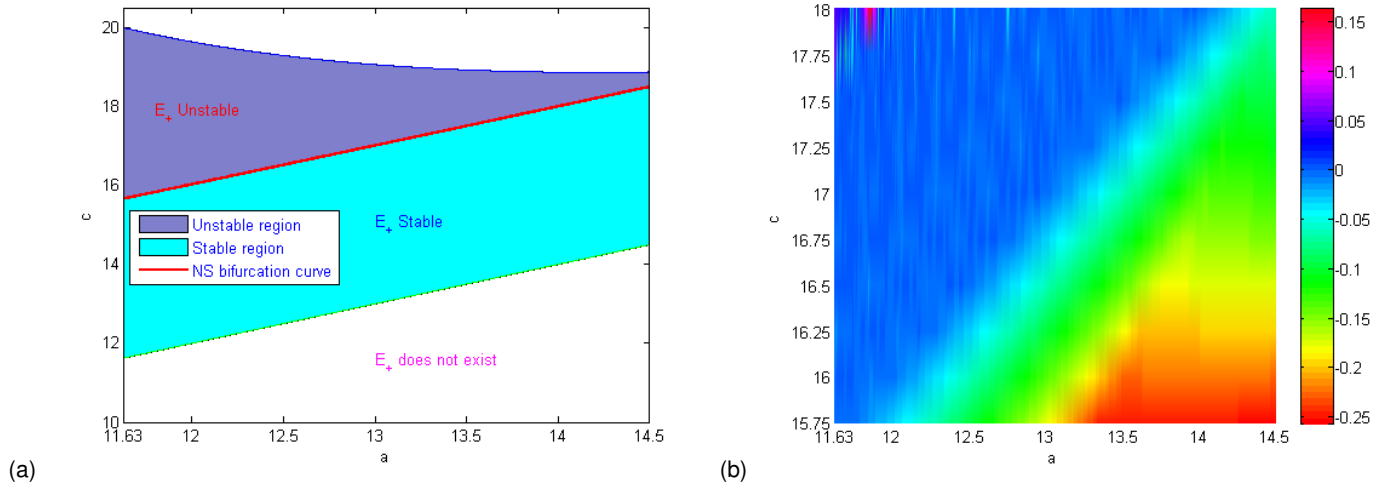


Figure 7 System Dynamics for two control parameters (a) Stability region in (a, c) plane (b) The projection of MLEs onto (a, c) plane (c) NS bifurcation in (a, c, x) space for $a \in [2.6, 7.5]$ and $c = 3, 3.6, 4.2, 5.04, 6 \in [3, 6]$.

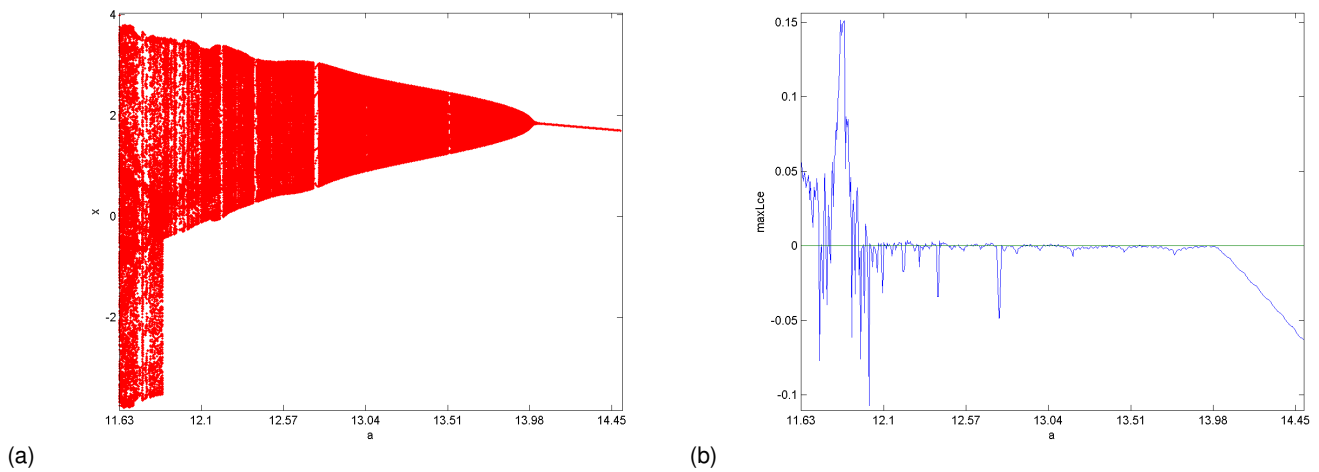


Figure 8 NS Bifurcation diagram: in (a) (a, x) plane, (b) MLEs, $(x_0, y_0, z_0) = (1.95, 1.95, 1.2)$.

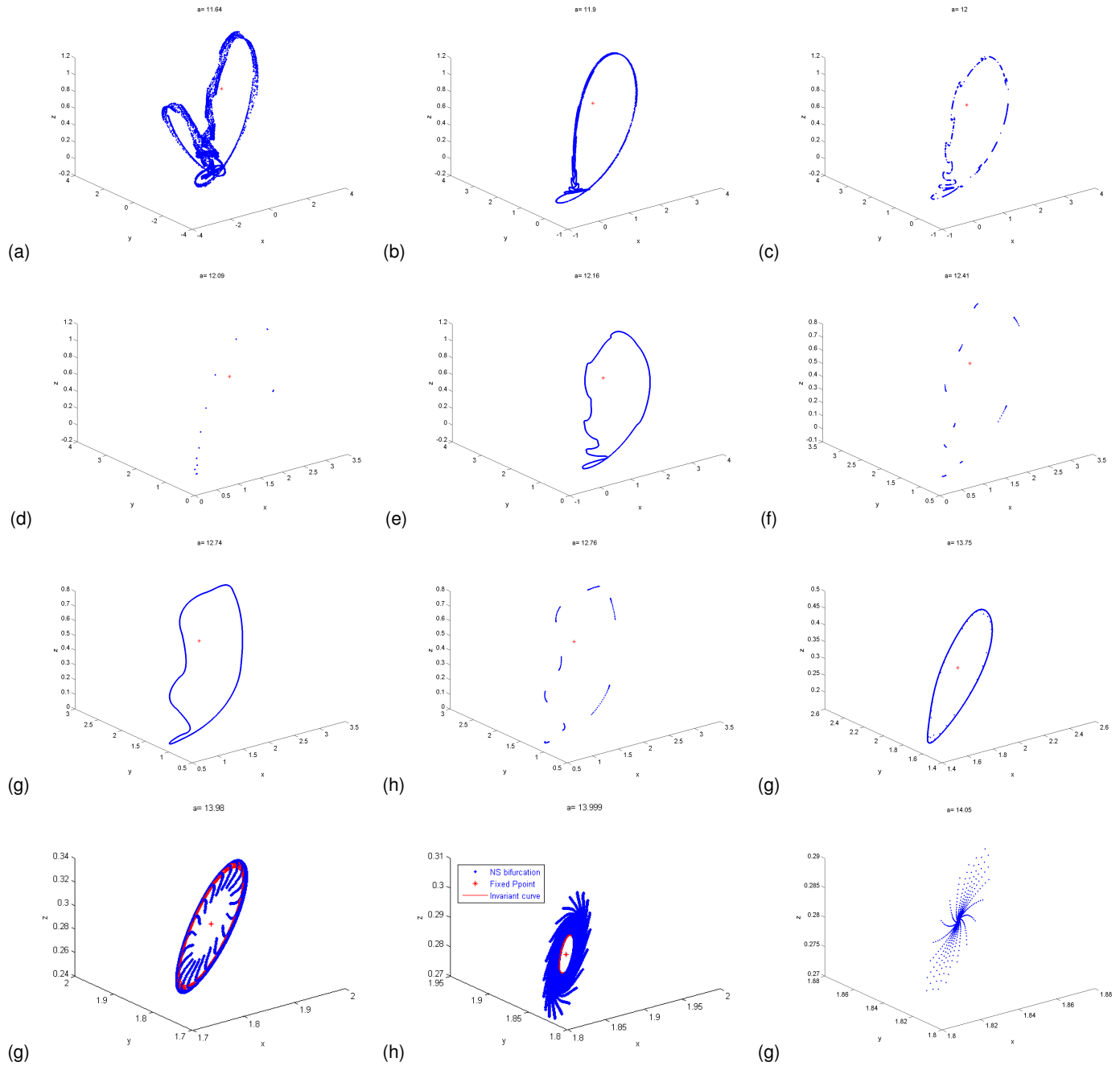


Figure 9 Phase portrait for different values of α corresponding to Figure 8 a. Red * is the fixed point E_+ .

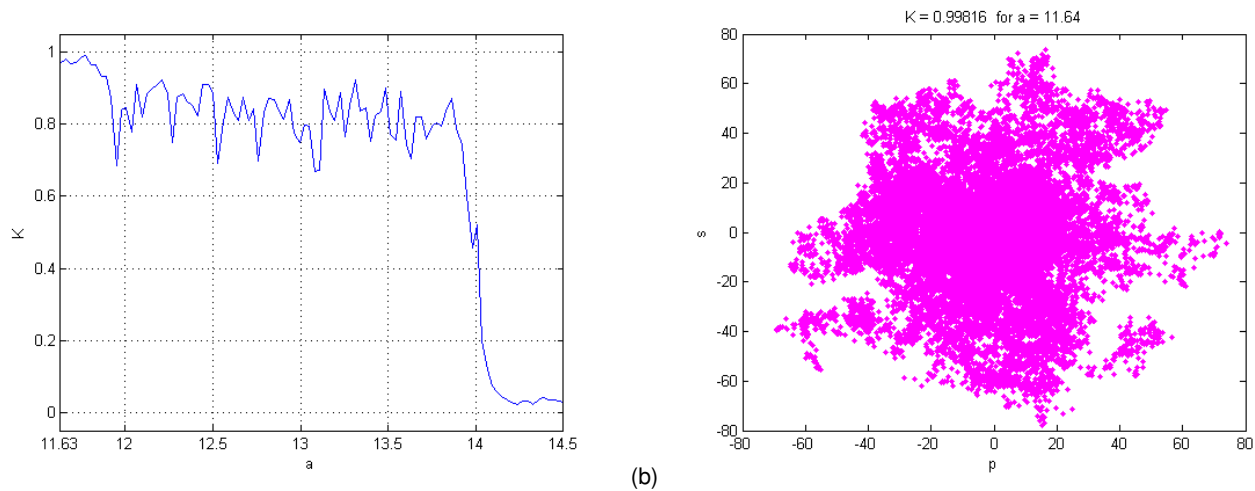


Figure 10 0 – 1 test for Chaos of system (2). (a) The curve of median of correlation coefficient in (K, δ) plane (b) Dynamics of system (2) in new (p, s) plane.

CHAOS CONTROL

Hybrid control strategy (Yuan and Yang 2015) is applied to system (2) to get the following controlled system

$$\begin{cases} x_{n+1} = \rho(x_n + \delta(a(y_n - x_n))) + (1 - \rho)x_n, \\ y_{n+1} = \rho(y_n + \delta((c - a)x_n - ax_n z_n)) + (1 - \rho)y_n, \\ z_{n+1} = \rho(z_n + \delta(x_n y_n - bz_n)) + (1 - \rho)z_n \end{cases} \quad (28)$$

For the controlled system (28), at fixed point $E_+ = \left(\sqrt{\frac{b}{a}(c-a)}, \sqrt{\frac{b}{a}(c-a)}, \frac{c-a}{a}\right)$, the zeroes of $|\mu I - J(E_+)|$ (eigenvalues of J) satisfy the equation

$$\mu^3 + \varepsilon_2 \mu^2 + \varepsilon_1 \mu + \varepsilon_0 = 0. \quad (29)$$

where,

$$\begin{aligned} \varepsilon_2 &= -3 + \delta\rho(a + b), \\ \varepsilon_1 &= 3 - 2a\delta\rho + b\delta\rho(-2 + c\delta\rho), \\ \varepsilon_0 &= -1 - 2a^2b\delta^3\rho^3 + b\delta\rho(1 - c\delta\rho) + a(\delta\rho + 2bc\delta^3\rho^3) \end{aligned} \quad (30)$$

Lemma 7 If the fixed point E_+ of the uncontrolled system (2) is unstable, then it is a sink (stable) the controlled system (28), if the roots of (29) lie inside open disk satisfying conditions in Lemma 2.

Example 6 To see the effectiveness of hybrid control strategy to control chaotic (unstable) system dynamics, we fix $b = 12, c = 18, \delta = 0.1057$ with $a = 11.64 < a_{NS,+}$. The fixed point $E_+(2.56061, 2.56061, 0.546392)$ of system (2) is then demonstrated to be unstable (see Fig 8), however it is stable for the controlled system (28) iff $0 < \rho < 0.596385$. Taking $\rho = 0.55$, the unstable system dynamics around E_+ are eliminated showing that E_+ is a sink for the controlled system (28) which have been displayed in Figure 11 (a,b). Moreover, for the choice of $\rho = 0.7$, the NS bifurcation moves to negative a -axis and occurs at $a = 12.5042$ for this controlled system by hybrid control strategy (see Figure 11 (c)).

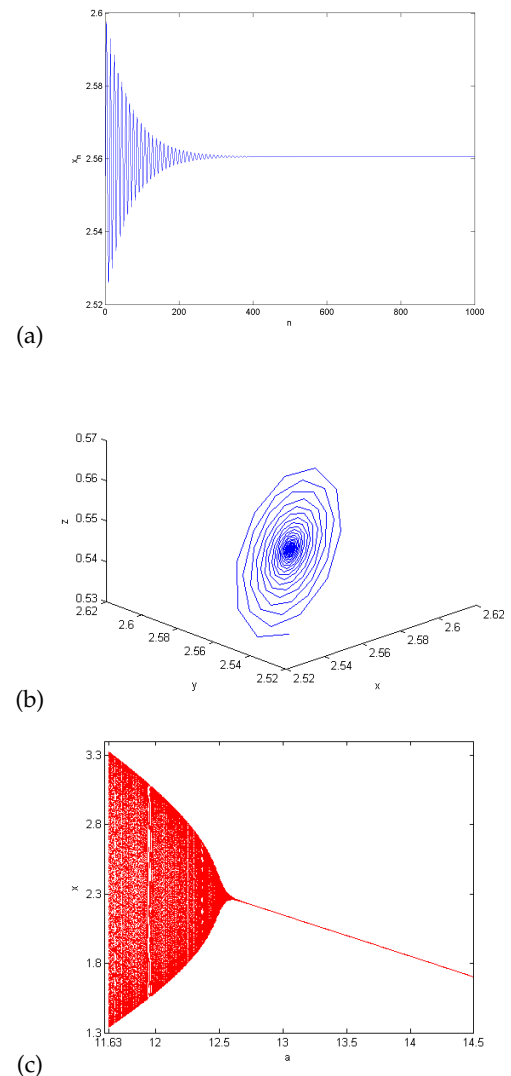


Figure 11 Dynamics of controlled system (28), (a) Time history of x (b) Phase diagram (c) NS bifurcation in (a, x) -plane for $\rho = 0.7$.

CONCLUSION

We analysis discrete-time chaotic T system both qualitatively and quantitatively. The Hopf bifurcation of the T system occurs, and it has an irregular chaotic attractor. We discover that the discrete T system exhibits more varied dynamical behaviors than the continuous system. Firstly, the conditions and directions of NS bifurcation of system (2) around E_0 are explicitly described by center manifold theory. Then we find the criteria of happening Flip and NS bifurcations of system (2) around fixed point E_+ .

In addition, we determine directions of these bifurcations. More Specifically, NS bifurcation around E_0 and Flip or NS bifurcation around E_+ take place of system (2) for small perturbation of bifurcation parameter δ or a . Both bifurcations change system dynamics topologically and trigger a route to chaos. For the generation of NS bifurcation, we find closed invariant curve, sudden break down of closed curve, period -9 , -11 orbits and chaotic attractors when δ and/or a pass their threshold values. For the generation of flip bifurcation, we observe the stable period -1 orbit becomes period -2 , -4 , orbits, 4 closed curves, two-coexisting chaotic sets and nice attracting chaotic set respectively for growth of δ .

Based on two dimensional parameteric space, we see how the mechanism of NS bifurcation switch the behaviors of system and advance or delay of occurring bifurcation when two parameters vary simultaneously. Moreover, for all the cases chaoticity of system dynamics are justified with sign of MLEs and $0 - 1$ chaos test. Finally, we are able to control and eliminate unstable system trajectories by hybrid control strategy. For this system, it is open to study the other properties like synchronization and co-dimension-2 bifurcation. Studying how two factors affect the dynamics of the discrete T system will be intriguing and difficult, but it is something to keep in mind for future study.

Conflicts of interest

The author declares that there is no conflict of interest regarding the publication of this paper.

Availability of data and material

Not applicable.

LITERATURE CITED

- Abdelaziz, M. A., A. I. Ismail, F. A. Abdullah, and M. H. Mohd, 2020 Codimension one and two bifurcations of a discrete-time fractional-order seir measles epidemic model with constant vaccination. *Chaos, Solitons & Fractals* **140**: 110104.
- Babloyantz, A., J. Salazar, and C. Nicolis, 1985 Evidence of chaotic dynamics of brain activity during the sleep cycle. *Physics letters A* **111**: 152–156.
- Camouzis, E. and G. Ladas, 2007 *Dynamics of third-order rational difference equations with open problems and conjectures*, volume 5. CRC Press.
- Chakraborty, P., S. Sarkar, and U. Ghosh, 2020 Stability and bifurcation analysis of a discrete prey–predator model with sigmoidal functional response and allee effect. *Rendiconti del Circolo Matematico di Palermo Series 2* pp. 1–21.
- Chen, G., 1999 *Controlling chaos and bifurcations in engineering systems*. CRC press.
- Chen, G. and X. Dong, 1998 *From chaos to order: methodologies, perspectives and applications*, volume 24. World Scientific.
- Din, Q. and W. Ishaque, 2019 Bifurcation analysis and chaos control in discrete-time eco–epidemiological models of pelicans at risk in the salton sea. *International Journal of Dynamics and Control* **8**: 132–148.
- El Naschie, M., 2003 Non-linear dynamics and infinite dimensional topology in high energy particle physics. *Chaos, Solitons & Fractals* **17**: 591–599.
- Fei, L., X. Chen, and B. Han, 2021 Bifurcation analysis and hybrid control of a discrete-time predator–prey model. *Journal of Difference Equations and Applications* **27**: 102–117.
- Feng, G., D. Yin, and L. Jiacheng, 2021 Neimark–sacker bifurcation and controlling chaos in a three-species food chain model through the ogy method. *Discrete Dynamics in Nature and Society* **2021**.
- Gottwald, G. A. and I. Melbourne, 2004 A new test for chaos in deterministic systems. *Proceedings of the Royal Society of London. Series A: Mathematical, Physical and Engineering Sciences* **460**: 603–611.
- Hu, Z., Z. Teng, and L. Zhang, 2014 Stability and bifurcation analysis in a discrete sir epidemic model. *Mathematics and computers in Simulation* **97**: 80–93.
- Ishaque, W., Q. Din, M. Taj, and M. A. Iqbal, 2019 Bifurcation and chaos control in a discrete-time predator–prey model with nonlinear saturated incidence rate and parasite interaction. *Advances in Difference Equations* **2019**: 1–16.
- Jiang, B., X. Han, and Q. Bi, 2010 Hopf bifurcation analysis in the t system. *Nonlinear Analysis: Real World Applications* **11**: 522–527.
- Kengne, J., Z. Njitacke, and H. Fotsin, 2016 Dynamical analysis of a simple autonomous jerk system with multiple attractors. *Nonlinear Dynamics* **83**: 751–765.
- Khan, A. and M. Javaid, 2021 Discrete-time phytoplankton–zooplankton model with bifurcations and chaos. *Advances in Difference Equations* **2021**: 1–30.
- Khan, M. S., M. Ozair, T. Hussain, J. Gómez-Aguilar, *et al.*, 2021 Bifurcation analysis of a discrete-time compartmental model for hypertensive or diabetic patients exposed to covid-19. *The European Physical Journal Plus* **136**: 1–26.
- Kuznetsov, Y. A., 2013 *Elements of applied bifurcation theory*, volume 112. Springer Science and Business Media, New York, USA.
- Li, B. and Q. He, 2019 Bifurcation analysis of a two-dimensional discrete hindmarsh–rose type model. *Advances in difference equations* **2019**: 1–17.

- Li, X.-F., Y.-D. Chu, J.-G. Zhang, and Y.-X. Chang, 2009 Nonlinear dynamics and circuit implementation for a new lorenz-like attractor. *Chaos, Solitons & Fractals* **41**: 2360–2370.
- Liu, Y. and X. Li, 2021 Dynamics of a discrete predator-prey model with holling-ii functional response. *International Journal of Biomathematics* p. 2150068.
- Lorenz, E. N., 1963 Deterministic nonperiodic flow. *Journal of atmospheric sciences* **20**: 130–141.
- Lü, J., G. Chen, and S. Zhang, 2002 Dynamical analysis of a new chaotic attractor. *International Journal of Bifurcation and chaos* **12**: 1001–1015.
- Luo, W., Q. Ou, F. Yu, L. Cui, and J. Jin, 2020 Analysis of a new hidden attractor coupled chaotic system and application of its weak signal detection. *Mathematical Problems in Engineering* **2020**.
- Pecora, L. M. and T. L. Carroll, 1991 Driving systems with chaotic signals. *Physical review A* **44**: 2374.
- Qin, S., J. Zhang, W. Du, and J. Yu, 2016 Neimark–sacker bifurcation in a new three–dimensional discrete chaotic system. *ICIC-EL* **10**: 1–7.
- Rabinovich, M. and H. Abarbanel, 1998 The role of chaos in neural systems. *Neuroscience* **87**: 5–14.
- Rana, S. M. S., 2019a Bifurcations and chaos control in a discrete-time predator-prey system of leslie type. *Journal of Applied Analysis & Computation* **9**: 31–44.
- Rana, S. M. S., 2019b Dynamics and chaos control in a discrete-time ratio-dependent holling-tanner model. *Journal of the Egyptian Mathematical Society* **27**: 1–16.
- Rössler, O. E., 1976 An equation for continuous chaos. *Physics Letters A* **57**: 397–398.
- Sachdev, P. and R. Sarathy, 1994 Periodic and chaotic solutions for a nonlinear system arising from a nuclear spin generator. *Chaos, Solitons & Fractals* **4**: 2015–2041.
- Singh, A. and P. Deolia, 2021 Bifurcation and chaos in a discrete predator–prey model with holling type-iii functional response and harvesting effect. *Journal of Biological Systems* **29**: 451–478.
- Sparrow, C., 2012 *The Lorenz equations: bifurcations, chaos, and strange attractors*, volume 41. Springer Science and Business Media.
- Sundarapandian, V., 2011 Global chaos anti-synchronization of tigan and lorenz systems by nonlinear control. *Int J Math Sci Appl* **1**: 679–690.
- Tang, S. and L. Chen, 2003 Quasiperiodic solutions and chaos in a periodically forced predator–prey model with age structure for predator. *International Journal of Bifurcation and Chaos* **13**: 973–980.
- Tigan, G., 2005 Analysis of a dynamical system derived from the lorenz system. *Sci. Bull. Politehnica Univ. Timisoara Tomu* **50**: 61–72.
- Ueta, T. and G. Chen, 2000 Bifurcation analysis of chen’s equation. *International Journal of Bifurcation and Chaos* **10**: 1917–1931.
- Vaidyanathan, S. and K. Rajagopal, 2011 Anti-synchronization of li and t chaotic systems by active nonlinear control. In *Advances in Computing and Information Technology: First International Conference, ACITY 2011, Chennai, India, July 15-17, 2011. Proceedings*, pp. 175–184, Springer.
- Wen, G., 2005 Criterion to identify hopf bifurcations in maps of arbitrary dimension. *Physical Review E* **72**: 026201.
- Xin, B., T. Chen, and J. Ma, 2010 Neimark-sacker bifurcation in a discrete-time financial system. *Discrete Dynamics in Nature and Society* **2010**.
- Xin, B. and Y. Li, 2013 0-1 test for chaos in a fractional order financial system with investment incentive. In *Abstract and Applied Analysis*, volume 2013, Hindawi.
- Xin, B. and Z. Wu, 2015 Neimark–sacker bifurcation analysis and 0–1 chaos test of an interactions model between industrial production and environmental quality in a closed area. *sustainability* **7**: 10191–10209.
- Yang, T. and L. O. Chua, 1997 Impulsive stabilization for control and synchronization of chaotic systems: theory and application to secure communication. *IEEE Transactions on Circuits and Systems I: Fundamental Theory and Applications* **44**: 976–988.
- Yao, S., 2012 New bifurcation critical criterion of flip-neimark-sacker bifurcations for two-parameterized family of-dimensional discrete systems. *Discrete Dynamics in Nature and Society* **2012**.
- Yong, C. and Y. Zhen-Ya, 2008 Chaos control in a new three-dimensional chaotic t system. *Communications in Theoretical Physics* **49**: 951.
- Yuan, L.-G. and Q.-G. Yang, 2015 Bifurcation, invariant curve and hybrid control in a discrete-time predator–prey system. *Applied Mathematical Modelling* **39**: 2345–2362.
- Zhang, Y., Q. Cheng, and S. Deng, 2022 Qualitative structure of a discrete predator-prey model with nonmonotonic functional response. *Discrete & Continuous Dynamical Systems-S*.
- Zhao, M., 2021 Bifurcation and chaotic behavior in the discrete bvp oscillator. *International Journal of Non-Linear Mechanics* **131**: 103687.

How to cite this article: Rana, S., S. Bifurcation Analysis and 0-1 Chaos Test of a Discrete T System. *Chaos Theory and Applications*, 5(2), 90-104, 2023.

Prediction of Gender and Age Period from Periorbital Region with VGG16

Omer Faruk Akmeşe¹, Huseyin Cizmeci², Selim Ozdemir³, Fikri Ozdemir⁴, Emre Deniz⁵, Rabia Mazman⁶, Murat Erdogan⁷ and Esmâ Erdogan⁸

¹Department of Computer Engineering, Hitit University, Corum, Türkiye, ²Department of Computer Technology, Hitit University, Corum, Türkiye, ³Department of Anatomy, Hitit University, Corum, Türkiye, ⁴Department of Forensic Sciences, Hitit University, Corum, Türkiye.

ABSTRACT Using deep learning methods, age and gender estimation from people's facial area has become popular. Recently, with the increase in the use of masks due to Covid-19, only the eye area of people is seen. The periorbital region can give an idea about the person's characteristics, such as age and gender. This study it is aimed to predict gender and age from images obtained by cutting the eye area from facial photographs of people using Visual Geometry Group-16 (VGG16). With the transfer learning method for age group (male, female) and gender group (child, youth, adults, and old) classification, 5714 images in the data set were used for the age group, and 3280 images were used for the gender group. As a result of this study, 99.41% success in age estimation and 95.73% in gender estimation was achieved.

KEYWORDS

Deep learning
Age and gender prediction
VGG16
Periorbital area

INTRODUCTION

Humans are social beings that interact with the environment they live in. Gender plays a fundamental role in social life. With the gender difference situation, people's speech, form of address, and behavior also differ. These differences are just a few of the gender commitments in social interactions (Gündüz and Cedimoğlu 2019).

The use of artificial intelligence and deep learning applications is becoming more and more common (Hinton and Salakhutdinov 2006; Solmaz et al. 2020). Artificial intelligence applications that make predictions about age and appearance on social media are frequently preferred by users. It is seen that many mobile applications make applications such as age estimation, aging, and rejuvenation on mobile platforms. These applications are generally used for entertainment purposes. Another important example is that the Xiaomi Mi 6 has an 8-megapixel front camera. In addition to the automatic facial beautification filter, this front camera also

offers the user a system that can predict gender and age with its artificial intelligence.

Artificial intelligence applications are becoming widespread in every field, and their applications have been seen in forensic cases recently (Zha et al. 2022; Aslan et al. 2022). The amount of data stored or transferred has increased with the intensive use of the Internet and information devices. As a result, there has been an increase in the crime rate. The amount of evidence obtained regarding the crimes committed has increased as the amount of data. Increasing evidence has made it difficult for experts in the field of forensic informatics to analyze the data with the available facilities. The disruptions experienced in the forensic informatics evidence and data analysis processes have caused negativities in the forensic trial processes (Dilber and Çetin 2021). In some forensic cases, the evidence is very insufficient. In such cases, artificial intelligence applications can come into play. This study developed models that predict gender and age group from photographs using deep learning methods. The study aimed to estimate the gender and age group using only eye photographs as evidence in a forensic case using deep learning algorithms. It is aimed to speed up the process of gender determination in the evidence related to this method and to facilitate data analysis.

Numerous studies have been conducted to improve and develop methods for assessing age and gender. In order to identify the gender and age of a single individual from their photo, Abu Nada et al. (2020) developed a double-check layer validator that makes use of deep learning methods, specifically a Convolutional

Manuscript received: 28 February 2023,

Revised: 31 May 2023,

Accepted: 7 June 2023.

¹ofarukakmese@hitit.edu.tr

²huseyincizmeci@hitit.edu.tr (Corresponding author)

³selimozdemir@hitit.edu.tr

⁴fikriozdemir@hitit.edu.tr

⁵emred Deniz@hitit.edu.tr

⁶rabiayasaroglu.1969@gmail.com

⁷muraterdogan41@gmail.com

⁸esnardgn19@gmail.com

tional Neural Network (CNN). In their investigation, they discovered that estimating age was 57% correct while estimating gender was 82% accurate. Duan *et al.* (2018) introduced a hybrid structure which includes CNN and Extreme Learning Machine to perform age and gender classification. They stated that the accuracy rate in the test results was 52.3% for age prediction and 88.2% for gender prediction. Oladipo *et al.* (2022) developed an age estimations system using genetic algorithm and backpropagation trained artificial neural network. Kumar *et al.* (2022) proposed a study, which is based on Seg-Net based architecture and machine learning algorithms to classify person's gender and age from diverse facial photos. Although it is seen that various age and gender estimation studies have been carried out for different application areas, it has been observed that these studies have not been studied sufficiently in the field of forensics.

MATERIAL AND METHOD

Artificial intelligence refers to systems or machines in which the human learning process is mathematically modeled. It imitates human intelligence to perform tasks and can gradually improve itself with the information it collects. Different techniques have emerged with the increase in artificial intelligence studies. Deep learning is one of the machine learning methods used in artificial intelligence studies that allow computers to learn from experience (Kim 2016). When the literature is scanned, it is seen that there are many areas where deep learning is used. Deep learning applications are being developed in various subjects, such as image and video processing, biomedical signal processing, object recognition, robotics, chemistry, finance, search engines, and autonomous vehicle systems (Şeker *et al.* 2017). VGG16 including deep learning, is an artificial neural network that is effective in prediction and classification (Zhu *et al.* 2023). Therefore, the VGG16 method was preferred in this study.

Deep Learning

Machine learning is the scientific study of statistical models for computer systems to perform a specific predefined task without specifying an explicit command or instruction by the user (Bingol *et al.* 2020). A sub-branch of artificial intelligence studies is machine learning. One of the most popular applications of machine learning is image and image recognition. In image recognition applications, machine-like images must be introduced for the machine to learn the image in question. As a result of this learning, the machine can easily distinguish different pictures from each other or detect the common points of similar pictures. VGG16 architecture is effective in computer vision tasks and is used in detail in the modeling of this study.

Many libraries are available in the Python programming language, each suitable for a different purpose. Selecting the appropriate libraries according to the data to be studied increases the accuracy rate. This study used Keras and TensorFlow libraries containing machine learning algorithms. In the study, images belonging to two classes (female and male) were used for gender estimation with the VGG16 model. Images belonging to four classes (child, young, adult, and old) were used for age estimation. In the study, age and gender classification was made with the VGG16 transfer learning model.

Dataset

The photos used in the dataset were taken from (Generated Photos 2022). These photos are artificial faces created by artificial intelligence methods, which are not in reality but are very realistic.

As seen in Figure 1, the eye parts of the photographs in the data set were cut to the same dimensions. Each of the images has a resolution of 120x280 pixels. The photographs used in the data set were divided into two classes, 1630 female and 1650 male. This dataset is also divided into four more classes, 1486 of which are children, 1354 are young, 1472 are adults, and 1402 are old. The application is written using the python programming language on the TUBITAK ULAKBIM, High Performance and Grid Computing Center (TRUBA resources).

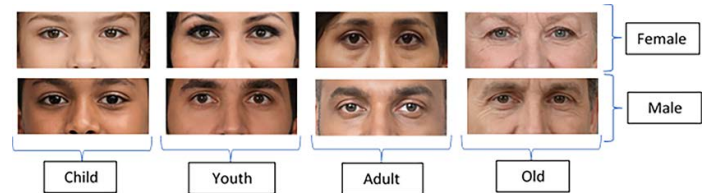


Figure 1 Examples of datasets compiled for the application.

Figure 2 shows the distribution of train, test, and train-test classes by age group. The distribution for train is 26% child, 23.9% youth, 25.5% adult, and 24.7% old. The distribution of each group for train-test is 80% as train and 20% as test.

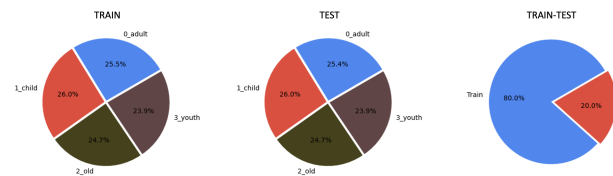


Figure 2 Train data set, test data set, train and test data set graphs for the age group.

In the study, data duplication was applied using the DataImageGenerator Function. The parameters used are shown in Table 1.

Regarding gender, Figure 3 shows the distribution of train, test, and train-test classes, respectively. For train, it is 49.7% female and 50.3% male. It was determined as 50% female and 50% male for the test. For the train test, 80% was reserved as train and 20% as test.

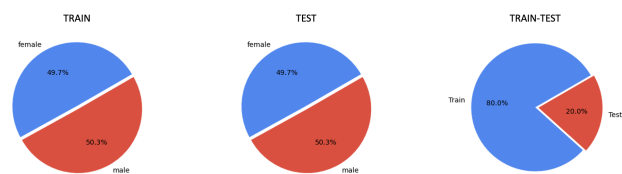


Figure 3 Graphs of train dataset, test dataset, train and test dataset for Gender.

Convolutional Neural Network

CNN, a deep learning algorithm, uses images as input data. It performs the classification process of images. CNN architecture consists of three layers. Convolutional Layer, Pooling Layer, and Fully Connected Layer (Bulut 2017). The features such as edge

■ **Table 1 Parameters of ImageDataGenerator Function.**

Parameter	Value
Rotation_range	10
Zoom_range	0.1
Width_shift_range	0.1
Height_shift_range	0.1

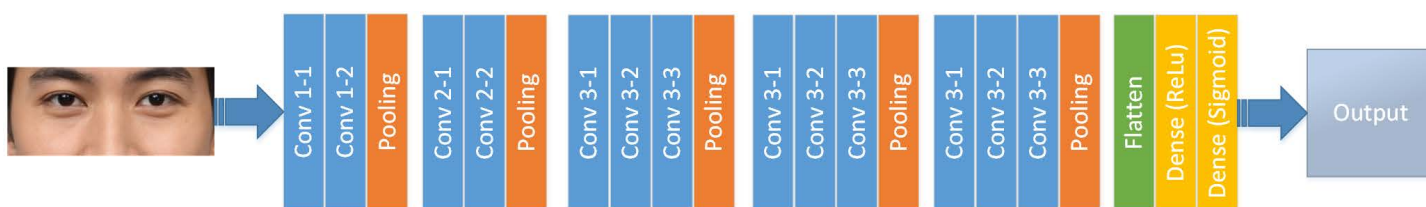


Figure 4 VGG16 model.

■ **Table 2 Parameters of Model.fit_generator Function.**

Parameter	Value
Batch_size	8
Epochs	15
Steps_per_epoch	8
Verbose	True

■ **Table 3 Gender Confusion Matrix.**

Accuracy : 95.73%	True Female	True Male	Total	Class Precision
Predicted Felame	230 (TP)	6 (FP)	236	94%
Predicted Male	15 (FN)	241 (TN)	256	98%
Total	245	247	492	96%
Class Recall	97%	94%	96%	

■ **Table 4 Age Group Confusion Matrix.**

Accuracy 99.41%	True Adult	True Child	True Old	True Youth	Total	Class Precision
Predicted Adult	216	0	0	1	217	100%
Predicted Child	0	221	0	4	225	100%
Predicted Old	0	0	211	0	211	100%
Predicted Youth	0	0	0	198	198	98%
Total	216	221	211	203	851	99%
Class Recall	100%	98%	100%	100%	99%	

■ **Table 5 Gender and Age Group Confusion Matrix.**

	Accuracy	F1-Score	Precision	Recall
Gender	96%	96%	96%	96%
Age Group	99%	99%	99%	99%

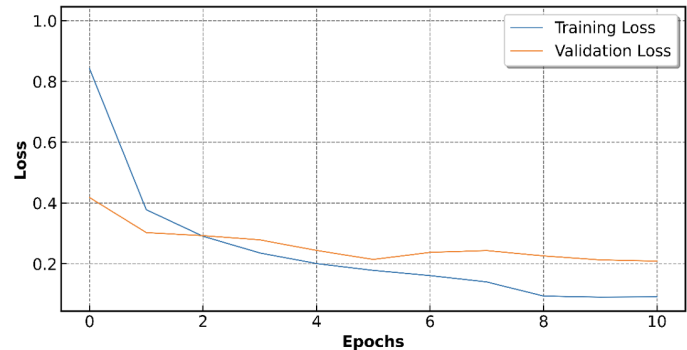
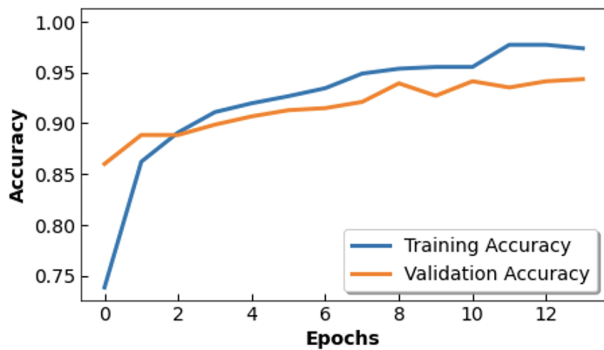


Figure 5 Gender classification success and loss graph.

and texture belonging to the features obtained from the image are found and transmitted to the other sublayers, respectively, and the values in the result layer are obtained (Metlek and Kayaalp 2020).

Convolutional Layer The Convolutional layer is the main layer of the CNN model. CNN extract features automatically in the convolution layer (Gündüz and Cedimoğlu 2019). Attributes are extracted using matrices whose input sizes are determined in the convolution layer (such as 11x11 in AlexNet, 5x5, 3x3, and 2x2 in VggNet). In our study, features were extracted using 2x2 matrices for the age group and 3x3 matrices for gender. With these extracted features, a new matrix was created, and data smaller than the input data were obtained. The matrix to be circulated on the image impacts the network's training and success (Metlek and Kayaalp 2020).

Pooling Layer The pooling layer usually comes after the activation process. In this layer, the data is reduced to smaller sizes. This process makes the network work faster and can lead to data loss. The preferred matrices for data reduction are the maximum (max pooling) value, the smallest (min pooling) value, and the average (average pooling) value matrices. A new matrix is obtained by circulating these matrices over the matrix obtained from the activation process. In our study, the softmax activation formula was used for the age group, and the sigmoid activation formula for gender. The equations of the functions are as follows:

$$softmax : y = \frac{e^{x_i}}{\sum_{j=1}^n e^{x_j}} \quad (1)$$

$$sigmoid : y = \frac{1}{1 + e^{-x}} \quad (2)$$

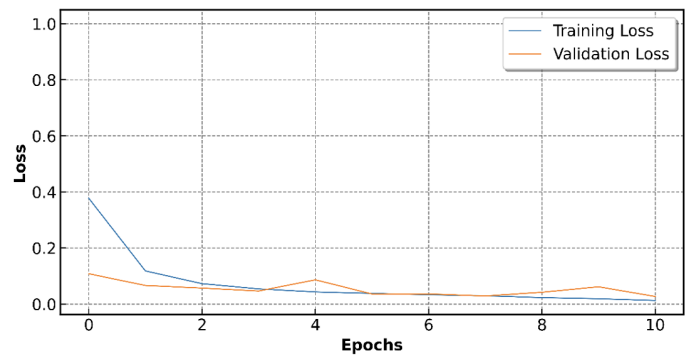
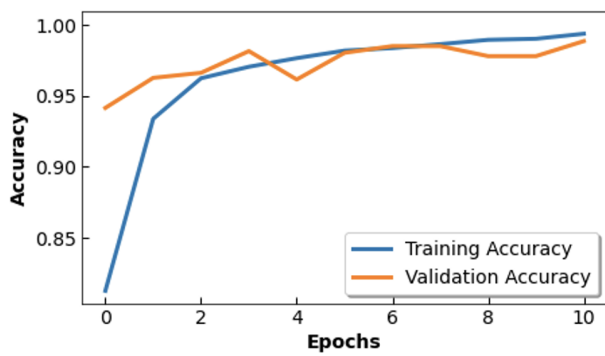


Figure 6 Age group classification success and loss graph.

Fully Connected Layer The fully connected layer is where all the connections in the previous layer are collected. The data from the fully connected layer is transferred to the result layer in one dimension (Metlek and Kayaalp 2020).

VGG16 Model

VGG16 is a deep learning model developed by the Visual Geometry Group at the University of Oxford. VGG16 represents a network architecture called VGGNet, an important milestone in the field of Convolutional Neural Networks. VGG16 is a convolutional neural network with 16 deep layers. These layers consist of convolutional layers, fully connected layers and activation layers. The VGG16 model differs from previous models in that it is deeper and has more parameters. The VGG16 model is specifically designed to be used in image classification tasks (Theckedath and Sedamkar 2020).

The model (Fig.4) was trained on the ImageNet dataset and achieved successful results in recognizing many different object classes. In addition, VGG16 can be used in different tasks with transfer learning methods, often using it as a pre-trained model. VGG16 is considered a milestone in the field of deep learning and convolutional neural networks and is used today as a basic model in many research and applications (Alkurdy et al. 2023).

The parameters used in the training of the model in the study are given in Table 2.

Performance Measurement Metrics

In classification models, the success rate is mostly determined by the relationships between the class values labeled by the practitioner and the actual class value (Aslan 2022). Accordingly, the performance is evaluated based on the TP (True Positive), TN (True Negative), FP (False Positive), and FN (False Negative) values in the complexity matrix. In scientific studies, values such as Accuracy, Precision, Recall, and F1 score are generally used for performance evaluation criteria (Bulut 2017). Accuracy is the overall correctness rate.

$$Accuracy = \frac{TP + TN}{TP + FP + TN + FN} \quad (3)$$

Precision is the proportion of correctly detected positive classes to all positives.

$$Precision = \frac{TP}{TP + FP} \quad (4)$$

Recall expresses the proportion of correctly identified Positive classes to true positives.

$$Recall = \frac{TP}{TP + FN} \quad (5)$$

The harmonic mean of sensitivity and precision is the F1-score.

$$F1 - score = \frac{2 \times Precision \times Recall}{Precision + Recall} \quad (6)$$

RESULTS

The training-validation accuracy and training-validation loss graphs of the VGG16 model are shown in Figure 5, respectively. As seen during the network training phase, the training process was completed with a data loss that could be considered insignificant, with a loss rate of 0.12.

The training-validation accuracy and training-validation loss graphs of the VGG16 model are shown in Figure 6, respectively. As seen during the network training phase, the training process was completed with a data loss that could be considered insignificant, with a loss rate of 0.015.

According to Table 3, the model correctly predicted gender at 96%. TP: true positives, TN: true negatives, FN: false negatives, and FP: false positives. Precision is the proportion of correctly detected positive classes to all positives. Recall expresses the proportion of correctly identified positive classes to true positives.

According to Table 4, Precision: Ratio of correctly detected Positive classes to all positives. Recall: Ratio of correctly detected Positive classes to true positives. Table 5 shows the model's accuracy, F1, precision, and recall values for gender and age group prediction. Accuracy is the overall correctness rate. F1-score: The harmonic mean of sensitivity and precision is the F1-score. Precision is the proportion of correctly detected positive classes to all positives. Recall expresses the proportion of correctly identified Positive classes to true positives.

CONCLUSION

This article it is aimed to estimate the gender and age group of individuals belonging to different gender and age groups, with photographs obtained by cutting the eye parts from the face area. A success rate of 95.73% was achieved in estimating gender and 99.41% in estimating age group. In the study, eye photographs of individuals wearing masks can be used to estimate their gender and age group information. As age and gender determination

can be important in revealing victim or suspect profiles, this and similar studies can support forensic processes. When the results obtained in the study were compared with those in the relevant literature, it was seen that more successful results were obtained for age and gender estimation. In future studies, new methods can be developed to enable us to reach faster, more accurate, and more reliable results using different data sets and models.

Conflicts of interest

The authors declare that there is no conflict of interest regarding the publication of this paper.

Acknowledgement

The numerical calculations reported in this paper were fully/partially performed at TUBITAK ULAKBIM, High Performance and Grid Computing Center (TRUBA resources).

Availability of data and material

Python code used in the study remains confidential as potential intellectual property.

LITERATURE CITED

- Abu Nada, A. M., E. Alajrami, A. A. Al-Saqqa, and S. S. Abu-Naser, 2020 Age and gender prediction and validation through single user images using cnn .
- Alkurdy, N. H., H. K. Aljobouri, and Z. K. Wadi, 2023 Ultrasound renal stone diagnosis based on convolutional neural network and vgg16 features. *Int J Electr Comput Eng* **13**: 3440–3448.
- Aslan, M., 2022 Derin öğrenme tabanlı otomatik beyin tümör tespiti. *Fırat Üniversitesi Mühendislik Bilimleri Dergisi* **34**: 399–407.
- Aslan, M. F., K. Sabanci, A. Durdu, and M. F. Unlarsen, 2022 Covid-19 diagnosis using state-of-the-art cnn architecture features and bayesian optimization. *Computers in Biology and Medicine* p. 105244.
- Bingol, K., A. E. Akan, H. T. Örmecioğlu, and A. Er, 2020 Artificial intelligence applications in earthquake resistant architectural design: Determination of irregular structural systems with deep learning and imageai method .
- Bulut, F., 2017 Örnek tabanlı sınıflandırıcı topluluklarıyla yeni bir klinik karar destek sistemi. *Gazi Üniversitesi Mühendislik Mimarlık Fakültesi Dergisi* **32**.
- Dilber, İ. and A. Çetin, 2021 Adli bilişim incelenme süreçlerinde yapay zeka kullanımı: Vgg16 ile görüntü sınıflandırma. *Düzce Üniversitesi Bilim ve Teknoloji Dergisi* **9**: 1695–1706.
- Duan, M., K. Li, C. Yang, and K. Li, 2018 A hybrid deep learning cnn-elm for age and gender classification. *Neurocomputing* **275**: 448–461.
- Generated Photos, 2022 AI Generated Photos. <https://generated.photos/faces/datasets>.
- Gündüz, G. and İ. H. Cedimoğlu, 2019 Derin öğrenme algoritmalarını kullanarak görüntüden cinsiyet tahmini. *Sakarya University Journal of Computer and Information Sciences* **2**: 9–17.
- Hinton, G. E. and R. R. Salakhutdinov, 2006 Reducing the dimensionality of data with neural networks. *science* **313**: 504–507.
- Kim, K. G., 2016 Book review: Deep learning. *Healthcare informatics research* **22**: 351–354.
- Kumar, S., S. Singh, J. Kumar, and K. Prasad, 2022 Age and gender classification using seg-net based architecture and machine learning. *Multimedia Tools and Applications* **81**: 42285–42308.
- Metlek, S. and K. Kayaalp, 2020 Derin öğrenme ve destek vektör makineleri ile görüntüden cinsiyet tahmini. *Düzce Üniversitesi Bilim ve Teknoloji Dergisi* **8**: 2208–2228.
- Oladipo, O., E. O. Omidiora, and V. C. Osamor, 2022 A novel genetic-artificial neural network based age estimation system. *Scientific Reports* **12**: 19290.
- Şeker, A., B. Diri, and H. H. Balık, 2017 Derin öğrenme yöntemleri ve uygulamaları hakkında bir inceleme. *Gazi Mühendislik Bilimleri Dergisi* **3**: 47–64.
- Solmaz, R., A. ALKAN, and M. GÜNAY, 2020 Mobile diagnosis of thyroid based on ensemble classifier. *Dicle Üniversitesi Mühendislik Fakültesi Mühendislik Dergisi* **11**: 915–924.
- Theckedath, D. and R. Sedamkar, 2020 Detecting affect states using vgg16, resnet50 and se-resnet50 networks. *SN Computer Science* **1**: 1–7.
- Zha, W., Y. Liu, Y. Wan, R. Luo, D. Li, *et al.*, 2022 Forecasting monthly gas field production based on the cnn-lstm model. *Energy* p. 124889.
- Zhu, F., J. Li, B. Zhu, H. Li, and G. Liu, 2023 Uav remote sensing image stitching via improved vgg16 siamese feature extraction network. *Expert Systems with Applications* p. 120525.

How to cite this article: Akmese, O.F., Cizmeci, H., Ozdem, S., Ozdemir, F., Deniz, E., Mazman, R., Erdogan, M., and Erdogan, E. Prediction of Gender and Age Period from Periorbital Region with VGG16. *Chaos Theory and Applications*, 5(2), 105-110, 2023.

Ocular Artifact Removal Method Based on the Wavelet and ICA Transform

Erdem Erkan¹ and Yasemin Erkan²

*Department of Computer Engineering, Bartin University, Bartin, Türkiye, ^aDepartment of Electrical and Electronics Engineering, Bartin University, Bartin, Türkiye.

ABSTRACT The electroencephalogram is a promising tool used to unravel the mysteries of the brain. However, such signals are often disturbed by ocular artifacts caused by eye movements. In this study, Independent Component Analysis and Wavelet Transform based ocular artifact removal method, which does not need reference signals, is proposed to obtain signals free from ocular artifacts. With our proposed method, firstly, the ocular artifact regions in the time domain of the signal are detected. Then the signal is decomposed into its components by independent component analysis and independent components containing artifacts are detected. Wavelet transform is only applied to these components with artifact. Zeroing is applied to the parts of the wavelet coefficients obtained as a result of the wavelet transform corresponding to the ocular artifact regions in the time domain. Finally, the clean signal is obtained by inverse Wavelet transform and inverse Independent Component Analysis methods, respectively. The proposed algorithm is tested on a real data set. The results are given in comparison with the method in which the zeroing is applied to the classical independent components. According to the results, it is seen that most of the signal is not affected by the zeroing and the neural part of the EEG signals is successfully preserved.

KEYWORDS

Electroencephalography
Electrooculogram
Independent
Component analysis
Brain computer
interface
Wavelet transform

INTRODUCTION

The investigation of psychophysiological signals has become an important research area by the desire for the human brain to be discovered. Researchers have been trying to understand psychophysiological signals and develop Brain Computer Interfaces (BCI) that can work in harmony with these signals in this area. Electroencephalography (EEG) the result of firing many neurons in the brain is the commonly used signal type in BCI studies (Wolpaw *et al.* 2006). The various types of artifacts could interfere with EEG signals such as ocular artifacts (OAs), cardiac artifacts and muscle artifacts. The OAs are the important sources of noise which make access to neural information difficult in EEG. The high amplitude of OAs are distorted the neural part of EEG signals (Yang *et al.* 2015).

The electrooculogram (EOG), which leads to OAs is the result of eye blinks and movements. These artifacts affect analysis of

EEG signals negatively. Therefore, EEG signals need to artefact removal process. In the literature, artifact removal methods have been proposed such as signal epoch rejection (Kirkove *et al.* 2014), regression (Krishnaswamy *et al.* 2016) and Blind Source Separation (BSS) methods (James and Hesse 2004; Vigario and Oja 2008). The Independent Component Analysis (ICA) which is a complex mathematical technique has been most commonly used to separate artifacts from EEG signals in many of these proposed methods (Bell and Sejnowski 1995; Jung *et al.* 2000; Hyvärinen and Oja 2000). Various studies have used visual inspection and manual artifact removal based methods (Akhtar *et al.* 2012; Mammone *et al.* 2011). Beside these methods, several studies that use ICA on the automatic artifacts removal method have been proposed (Sameni and Gouy-Pailler 2014; Judith *et al.* 2022). For example, it was reported an automatic method for ocular removal from simulated EEG signals based on ICA in a study (Romero *et al.* 2008, 2009). Sameni *et al.* used the ICA based automatic method to remove ocular artifacts from EEG signals (Sameni and Gouy-Pailler 2014). Çınar *et al.* presented OD-ICA method for determination of the OAs (Çınar and Acir 2017).

Manuscript received: 21 March 2023,

Revised: 22 May 2023,

Accepted: 1 July 2023.

¹eerkan@bartin.edu.tr

²yerkan@bartin.edu.tr (Corresponding author)

In the processes of artifact removal, it is important to recognize the properties which are decisive of the artifact such as amplitude and frequency. In order to determine these properties, different mathematical methods can be used in signal processing. Wavelet Transform (WT) is a very useful mathematical technique that allows to analyze signals, in the scale-time domain. The WT and ICA based OA removal methods are introduced in the literature. Nguyen et al. developed a real time neural network algorithm based on Wavelet for EEG artifact (Nguyen et al. 2012). Kelly et al. proposed a new method for use in high dimensional neural data based on Wavelet thresholding and ICA to localize artifacts (Kelly et al. 2010). Similarly, Ghandeharion et al. presented a new automatic artefact detection method which based on a combination of ICA and WT (Ghandeharion and Erfanian 2010). In the previous studies, ICA used for EEG decomposition. The artifactual Independent components (AICs) are rejected and the other ICs are used in reconstruction of artefact free EEG. The WT is also used for the focus of the signal to the frequency components containing artifacts by dividing the EEG signal into frequency components.

In this study, an eye artefact removal algorithm has been proposed. The eye artefact removal algorithm, unlike the studies in the literature, applies the zeroing operation only to the artifact-containing time segment of the relevant frequency component of the artifact. The proposed eye artefact removal algorithm apply a series of ICA decompositions to the EEG signal. The algorithm detects and extracts artifactual ICs (AICs) by selecting the best estimation with high correlation for automatic artifact detection. Thus, the proposed method, achieved much improvement in terms of removing OAs and preserving the neural part of EEG signals.

MATERIALS AND METHODS

EEG Acquisition

The data acquisition experiments is performed by 8 adult subjects. During the experiments, the subjects are imagined that they write Turkish syllables which are 'mer', 'ha', 'ba' and 'ar', 'ka', 'daş' on the screen. These syllables are the pieces of sound used to vocalize the 'hello' and 'friend' words in Turkish. The brain signals are recorded during the experiments by using 8 EEG gold-plated electrodes placed on scalp. Sampling rate is selected as 500 Hz. Electrodes placement is shown in Figure 1. The experimental procedure is also given in Figure 2. Before the recording, the subjects performed the experiment in a short training session. Each trial is recorded for 4 seconds duration which has rest period for one second. The EEG signals are obtained by use a Bioradio device which has been developed by Great Lakes NeuroTechnologies. The dataset is also published on Kaggle under the name "EEG Dataset with Ocular Artifact".

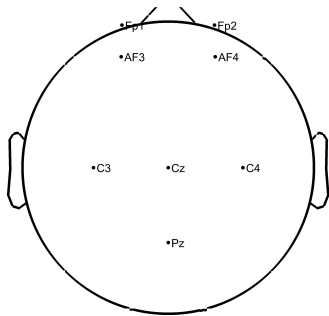


Figure 1 Electrodes placement.

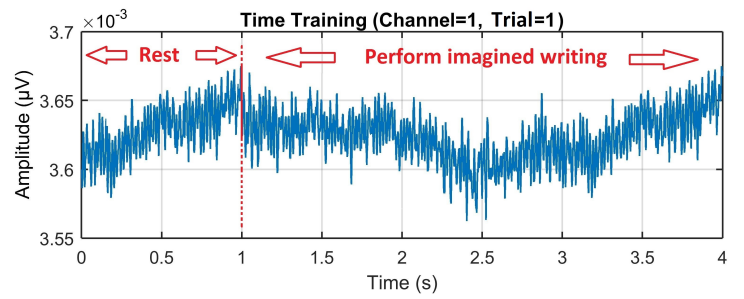


Figure 2 The experimental procedure.

Independent Component Analysis (ICA)

For BCI systems, it is essential to remove artifacts from the acquired signals as a result of eye movements, heartbeats, muscle activities and similar noises (Sahonero-Alvarez and Calderon 2017; McMenamin et al. 2011). The ICA method is used to convert a linearly mixed set of signals into another set that is independent of each other (Hyvärinen and Oja 2000; Stone 2002). The base of ICA relies on statistical independence. The general ICA approach is given by Equation 1. $x(t)$, A and $s(t)$ represent the signal vector received from the electrodes, the mixing matrix and the original source vector, respectively.

$$x(t) = \gamma s(t) \quad (1)$$

ICA method tries to determine unmixing matrix U that an approximately inverse of γ and given in Equation 2.

$$Ux(t) = O(t) \quad (2)$$

$O(t)$ is approximate original signal which separated from sources. The FastICA algorithm is preferred for the parallel implementation convenience in this paper (Behera 2009). The FastICA algorithm uses kurtosis for the independent components estimation (Langlois et al. 2010).

FastICA performs by the following procedure;

1. Initialize U_i (randomly)
2. $U_i^+ = E(\phi'(U_i^T X))U_i - E(x\phi(U_i^T))$
3. $U_i = \frac{U_i^+}{\|U_i^+\|}$
4. if $i = 1$, go to step 7. otherwise continue with step 5.
5. $U_i^+ = U_i - \sum_{j=1}^{i-1} U_j^T U_j U_i$
6. $U_i = \frac{U_i^+}{\|U_i^+\|}$
7. If converged go back to step 1 with $i = i + 1$ until all components are extracted else go back to step 2.

Wavelet Transformation (WT)

Wavelet transform is a very useful mathematical technique that allows to analyze EEG signals, in the scale-time domain. The WT is used to analyze in more detail the AICs. WT expresses the signal at different scales and time relative to the main wavelet. WC and ψ show Wavelet Coefficients and the mother wavelet respectively. The WCs are calculated in Equation 3 (Liu et al. 2023).

$$WC(Sca, Pos) = \int_{-\infty}^{+\infty} x(t)\psi(Sca, Pos, t)dt \quad (3)$$

Much more efficient WT, Discrete Wavelet Transform (DWT) which scaled and shifted by powers of two. The DWT calculation is given in Equation 4.

$$DWT(i, m) = \sum_i \sum_m x(m) 2^{-i/2} \psi(2^{-i}n - m) \quad (4)$$

The Daubechies mother wavelet which is the fundamental function to analyze the analog signals is used in DWT (He et al. 2007). 3 Level DWT decomposition is applied to the ICs by using Daubechies mother Wavelet. DWT levels of the ICs are given in Figure 3. The zeroing process is applied to only 3th level of the approximate DWT coefficients.

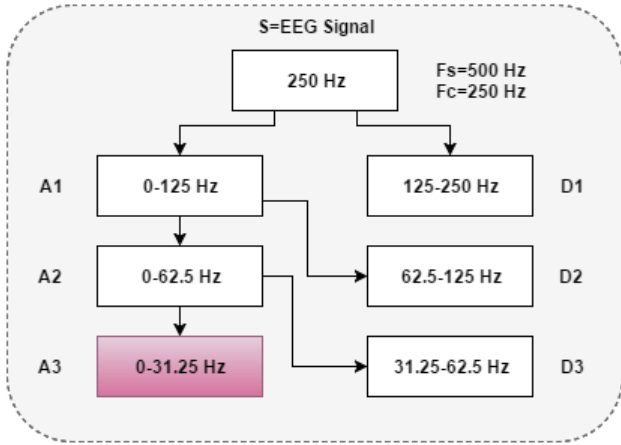


Figure 3 DWT levels of the ICs.

Eye Artefact Remover

In this section, the OA removal approach is given detailed.

Threshold Determination Determination of the threshold value is also important process in removal methods. The threshold value is determined according to each EEG signal by the proposed algorithm, although the value is usually fixed in existing studies (Kelly et al. 2010; Çınar and Acr 2017). Previous studies have found that blinking occurs in the 0.5 to 3.5 Hz frequency range. We used approximately this frequency range in our study (Nguyen et al. 2013). The threshold determination process is given in Figure 4.

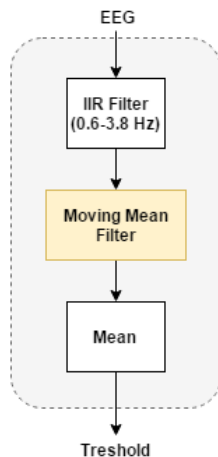


Figure 4 The threshold determination process.

The threshold value is obtained by the IIR and moving mean filtering. The frequency range is chosen as 0.6-3.8 Hz.

Artifact Detection OAs are components of lower frequency and higher amplitude than the neural part of the signal. The OAs are detected by using peak properties such as PPV and PDV which represent peak prominence value and peak distance value. The PPV that the minimum vertical distance that the signal must descend on either side of the peak before either climbing back to a level higher than the peak and the PDV that the distance between the two peaks are given in Figure 5. OAs create peaks in a certain band range in EEG signals. Determining the threshold value in this band range directly affects the OA detection success of the system. The minimum PPV and the minimum PDV are chosen as 0.3 s and $1.3e - 04 \mu V$ respectively. After determining the peak of the artifact by threshold, the bottoms of the artifact are determined by descending from both points of the artifact peak.

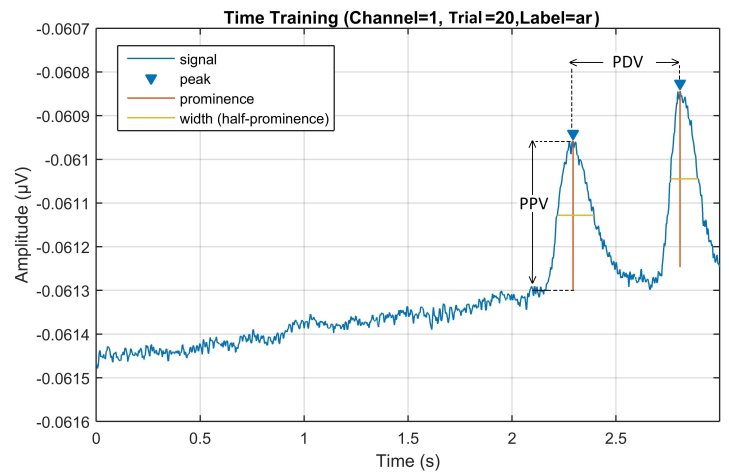


Figure 5 The sample EEG trial with OAs.

The height of descending point are determine the downward trend of the point. The bottom points of the artifact are reached, when the downward trend finish. The bottom points of the artifact determines the OA region which is on the wavelet coefficients of the AICs to use in the zeroing. However, Savitzky Golay filter was preferred for signal smoothing. The threshold value, smoothed signal, the OA region and peak bottoms are shown in Figure 6.

The artifact detection process is also applied to the ICs which obtained by ICA decomposition. Thus, AICs which are related with OAs are obtained. The result of a sample ICA decomposition is given in Figure 7. The OA regions, which given in Figure 6 and Figure 7 are suppressed by the zeroing process. The estimated AICs by the eye artefact removal algorithm are shown by yellow triangle marker in Figure 7.

Artifact Removal Process The block diagram of eye artefact removal is given in Figure 8. In Figure 8, first, It is applied ICA decomposition to the trials OA-containing by the eye artefact removal. After performing the ICA decomposition, the AICs are automatically identified by eye artefact removal and WT is applied to the AICs. The zeroing is applied only to the OA regions of AICs' third level approximate wavelet coefficients. Thus, the neural part of EEG signals is more successfully protected. Finally, the OAs free EEG signal is obtained by the inverse WT and ICA composition. The original EEG signal, training of the OA extraction process and

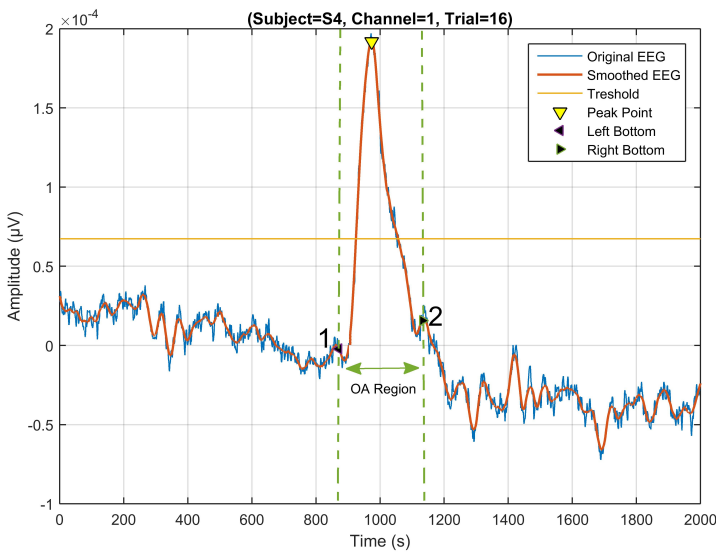


Figure 6 Sample EEG signal.

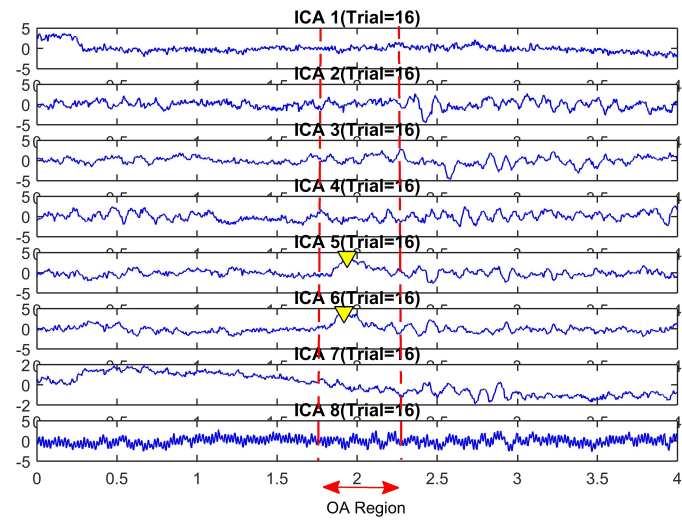


Figure 7 The result of a sample ICA decomposition.

clean EEG signal are given in a, b, c of Figure 9 which is the eye artefact removal application screenshot respectively.

The FastICA method is used for signal separation. The eye artefact removal obtains the best possible separation result by six iterations for one EEG trial.

Performance Evaluation

There is no general performance evaluation for artifact removal methods. As is known, EEG includes OA from a separate source such as eye muscles. These signals are highly inconsistent due to volumetric differences in their source. Therefore, after applying a perfect OA removal algorithm, the originally artifact-free portions of the signal should remain the same after EOG removal. This situation can best be expressed with the CC and STD parametrics (Kelly et al. 2010). For artifact removal evaluation has been used EEG experts or synthetic EEG data in the literature (Islam et al. 2016). Beside the non objective methods, Correlation Coefficient (CC), standard deviation difference (STD D.) and exterior standard

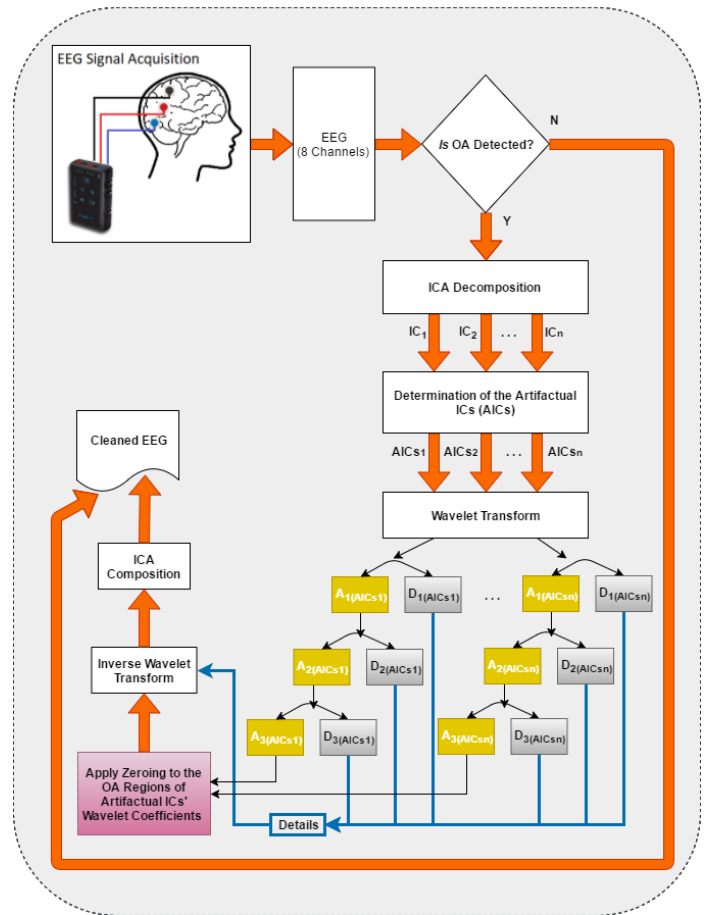


Figure 8 The general block diagram of the eye artefact removal algorithm.

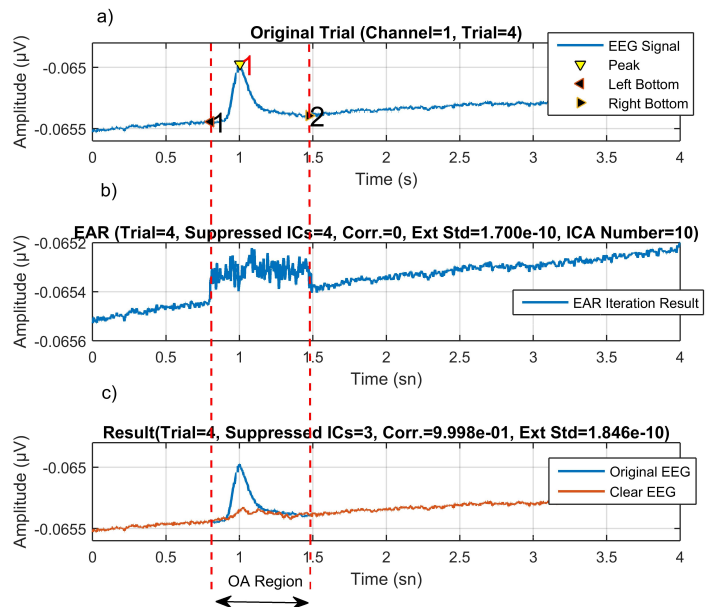


Figure 9 The eye artefact removal application screenshot.

deviation difference (E. STD) can be used to conduct a comparison. The CC and E. STD are given in Equations 5 and 6 respectively:

$$CC(x, y) = \frac{\sum(S_o - \bar{S}_o)(S_c - \bar{S}_c)}{\sqrt{\sum(S_o - \bar{S}_o)^2(S_c - \bar{S}_c)^2}} \quad (5)$$

$$E.STD(x, y) = \sqrt{\frac{1}{N} \sum_{i=1}^N (S_o - S_c)^2} \quad (6)$$

where \bar{S}_o and \bar{S}_c represents mean of the original EEG S_o and clean EEG S_c . The N represents length of the selected window in Equation 4. The CC and STD respectively, show how well the shape of the result signal is preserved and how much the signal power is affected. The high CC represents minimum changing between original and result EEG signal. Another evaluation criteria is the mean squared error between the STD of the original and result EEG signal. This is called as exterior STD (E. STD). (Kelly *et al.* 2010; Jafarifarmand *et al.* 2017). The CC, STD D. and E. STD are calculated for both original and result EEG signals.

RESULTS

Data were obtained from 8 healthy subjects. The number of trials, the number of trials containing OA, the mean number of AICs and the OA detection success are given in Table 1. The OA detection success is also confirmed by the expert.

■ **Table 1** The results of the experiments

Subject	Number of trials	Number of trials with OA	Mean number of AICs	OA detection success %
S ₁	227	108	3.07	96.30
S ₂	233	122	3.07	98.36
S ₃	230	125	3.24	95.20
S ₄	231	147	3.15	95.92
S ₅	231	158	3.01	98.73
S ₆	230	183	3.06	98.91
S ₇	118	28	3.26	96.43
S ₈	116	30	2.62	100

The mean number of AICs is observed about 3 in Table 1. It means that the zeroing process affects about 3 ICs for each EEG signal. The comparison of eye artefact removal and classical zeroing method results is given in Table 3.

■ **Table 2** OA removal by eye artefact removal-ICs zeroing

Subject	CC (x10 ⁻²)	STD (x10 ⁻⁶)	E. STD (x10 ⁻⁹)
S ₁	64.24±19.97	87.75±86.32	3.33±4.55
S ₂	57.43±19.71	75.67±90.07	3.99±6.78
S ₃	53.57±19.04	78.38±62.08	3.78±4.24
S ₄	55.75±19.20	67.52±56.17	2.13±2.34
S ₅	48.43±16.03	85.68±57.54	1.28±1.38
S ₆	55.18±16.76	66.78±48.86	0.93±0.84
S ₇	61.40±18.92	72.97±49.09	1.34±1.66
S ₈	79.87±19.73	53.04±66.23	0.86±2.30

■ **Table 3** OA removal by eye artefact removal

Subject	CC (x10 ⁻²)	STD (x10 ⁻⁶)	E. STD (x10 ⁻⁹)
S ₁	98.82±0.35	3.87±4.27	1.32±1.75
S ₂	98.70±0.39	5.37±6.22	1.74±1.92
S ₃	98.42±0.40	4.74±4.80	2.11±1.88
S ₄	98.05±0.44	4.76±6.09	1.38±1.27
S ₅	98.98±0.34	3.70±4.18	0.83±0.60
S ₆	99.34±0.19	2.92±3.06	0.68±0.45
S ₇	97.01±0.54	5.18±5.80	1.05±1.16
S ₈	98.22±0.49	5.10±5.46	0.38±0.65

The success of the eye artefact removal algorithm is shown in Table 3 and a,b of Figure 10. The comparison of three signals which original, cleared by eye artefact removal and cleared by classic ICA zeroing is also given in b of Figure 10. The values are given in Table 2 and Table 3 as mean ± standard deviation.

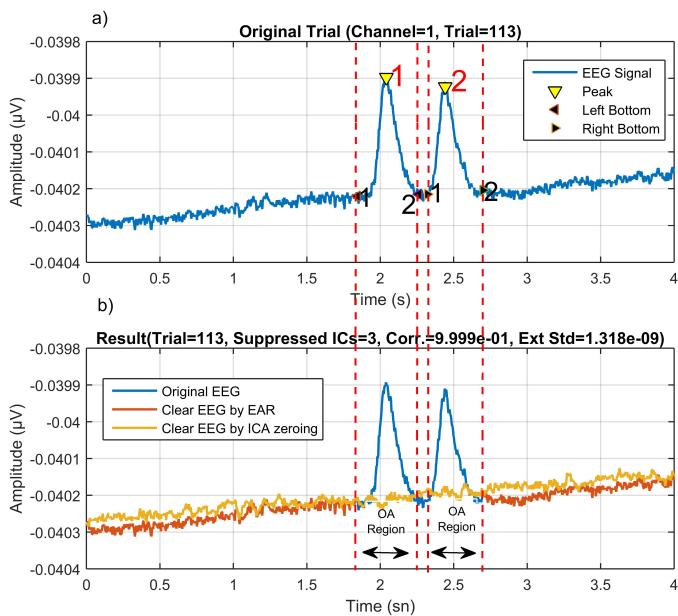


Figure 10 Visual comparison of eye artefact removal.

CONCLUSION

According to the experimental results, we have obtained that the proposed eye artefact removal algorithm shows superior performance over several commonly-used ICA based methods on OA removal. As seen from Table 2 and Table 3, the proposed method is better than classical zeroing method. As given in Table 3, 99.34 ± 0.19 CC value is achieved with Subject 6. The eye artefact removal algorithm never disturb any part of the signal except the OA regions which are shown as sample in Figure 7.

The eye artefact removal obtains the best possible separation result by six iterations for one EEG trial. The algorithm is used the FastICA method for signal separation. The selected separation method is also suitable for parallel programming. In the future, it is intended to increase of the eye artefact removal algorithm effectiveness with the parallel program version and analyze of the results of the eye artefact removal on classification.

In this paper, the eye artefact removal algorithm is proposed to remove OAs full automatically from OA contaminated EEG signals without any reference signals and user intervention. The performance of the eye artefact removal algorithm is tested on a real EEG dataset. The results are shown that the proposed algorithm could successfully eliminate OAs from real EEG signals and protect neural information with minimum loss. And also, the proposed algorithm is superior to the classical ICs zeroing method. The WT ensured that the signal was better separated and focused on the responsible frequency domain. The proposed algorithm, similar to the studies in the literature, detects OA on the EEG signal and performs OA reset. However, unlike the studies in the literature, applies the zeroing only to the artifact-containing time segment of the relevant frequency component of the artifact. By the applying of the zeroing to the OA regions of AICs' wavelet coefficients with a novel approach, a large amount of the EEG signal is not affected by the zeroing and the neural part of EEG signals was successfully protected.

Acknowledgments

The acquisition of EEG signals is approved by the Non-Interventional Clinical Research Ethics Committee at the University of Karabuk in Turkey.

Availability of data and material

The dataset used in the study is available on Kaggle under the name "EEG Dataset with Ocular Artifact".

Conflicts of interest

The authors declare that there is no conflict of interest regarding the publication of this paper.

LITERATURE CITED

- Akhtar, M. T., W. Mitsuhashi, and C. J. James, 2012 Employing spatially constrained ica and wavelet denoising, for automatic removal of artifacts from multichannel eeg data. *Signal processing* **92**: 401–416.
- Behera, S. K., 2009 *Fast ICA for Blind Source Separation and Its Implementation*. Ph.D. thesis.
- Bell, A. J. and T. J. Sejnowski, 1995 An information-maximization approach to blind separation and blind deconvolution. *Neural computation* **7**: 1129–1159.
- Çınar, S. and N. Acır, 2017 A novel system for automatic removal of ocular artefacts in eeg by using outlier detection methods and independent component analysis. *Expert Systems with Applications* **68**: 36–44.
- Ghandeharion, H. and A. Erfanian, 2010 A fully automatic ocular artifact suppression from eeg data using higher order statistics: Improved performance by wavelet analysis. *Medical engineering & physics* **32**: 720–729.
- He, Z., Y. Zi, X. Chen, and X. Wang, 2007 Transform principle of inner product for fault diagnosis. *Journal of vibration engineering* **20**: 528–533.
- Hyvärinen, A. and E. Oja, 2000 Independent component analysis: algorithms and applications. *Neural networks* **13**: 411–430.
- Islam, M. K., A. Rastegarnia, and Z. Yang, 2016 Methods for artifact detection and removal from scalp eeg: A review. *Neurophysiologie Clinique/Clinical Neurophysiology* **46**: 287–305.
- Jafarifarmand, A., M.-A. Badamchizadeh, S. Khanmohammadi, M. A. Nazari, and B. M. Tazehkand, 2017 Real-time ocular artifacts removal of eeg data using a hybrid ica-anc approach. *Biomedical signal Processing and control* **31**: 199–210.
- James, C. J. and C. W. Hesse, 2004 Independent component analysis for biomedical signals. *Physiological measurement* **26**: R15.
- Judith, A. M., S. B. Priya, and R. K. Mahendran, 2022 Artifact removal from eeg signals using regenerative multi-dimensional singular value decomposition and independent component analysis. *Biomedical Signal Processing and Control* **74**: 103452.
- Jung, T.-P., S. Makeig, C. Humphries, T.-W. Lee, M. J. Mckeown, *et al.*, 2000 Removing electroencephalographic artifacts by blind source separation. *Psychophysiology* **37**: 163–178.
- Kelly, J. W., D. P. Siewiorek, A. Smalagic, J. L. Collinger, D. J. Weber, *et al.*, 2010 Fully automated reduction of ocular artifacts in high-dimensional neural data. *IEEE Transactions on Biomedical Engineering* **58**: 598–606.
- Kirkove, M., C. François, and J. Verly, 2014 Comparative evaluation of existing and new methods for correcting ocular artifacts in electroencephalographic recordings. *Signal Processing* **98**: 102–120.

- Krishnaswamy, P., G. Bonmassar, C. Poulsen, E. T. Pierce, P. L. Purdon, *et al.*, 2016 Reference-free removal of eeg-fmri ballisto-cardiogram artifacts with harmonic regression. *Neuroimage* **128**: 398–412.
- Langlois, D., S. Chartier, and D. Gosselin, 2010 An introduction to independent component analysis: Infomax and fastica algorithms. *Tutorials in Quantitative Methods for Psychology* **6**: 31–38.
- Liu, J., S.-l. Liu, M. Medhat, and A. Elsayed, 2023 Wavelet transform theory: The mathematical principles of wavelet transform in gamma spectroscopy. *Radiation Physics and Chemistry* **203**: 110592.
- Mammone, N., F. La Foresta, and F. C. Morabito, 2011 Automatic artifact rejection from multichannel scalp eeg by wavelet ica. *IEEE Sensors Journal* **12**: 533–542.
- McMenamin, B. W., A. J. Shackman, L. L. Greischar, and R. J. Davidson, 2011 Electromyogenic artifacts and electroencephalographic inferences revisited. *NeuroImage* **54**: 4–9.
- Nguyen, H.-A. T., J. Musson, F. Li, W. Wang, G. Zhang, *et al.*, 2012 Eog artifact removal using a wavelet neural network. *Neurocomputing* **97**: 374–389.
- Nguyen, T., T. Nguyen, K. Truong, and T. Van Vo, 2013 A mean threshold algorithm for human eye blinking detection using eeg. In *4th international conference on biomedical engineering in Vietnam*, pp. 275–279, Springer.
- Romero, S., M. Mañanas, and M. J. Barbanoj, 2009 Ocular reduction in eeg signals based on adaptive filtering, regression and blind source separation. *Annals of biomedical engineering* **37**: 176–191.
- Romero, S., M. A. Mañanas, and M. J. Barbanoj, 2008 A comparative study of automatic techniques for ocular artifact reduction in spontaneous eeg signals based on clinical target variables: a simulation case. *Computers in biology and medicine* **38**: 348–360.
- Sahonero-Alvarez, G. and H. Calderon, 2017 A comparison of sobi, fastica, jade and infomax algorithms. In *Proceedings of the 8th International Multi-Conference on Complexity, Informatics and Cybernetics*, pp. 17–22.
- Sameni, R. and C. Gouy-Pailler, 2014 An iterative subspace denoising algorithm for removing electroencephalogram ocular artifacts. *Journal of neuroscience methods* **225**: 97–105.
- Stone, J. V., 2002 Independent component analysis: an introduction. *Trends in cognitive sciences* **6**: 59–64.
- Vigario, R. and E. Oja, 2008 Bss and ica in neuroinformatics: from current practices to open challenges. *IEEE reviews in biomedical engineering* **1**: 50–61.
- Wolpaw, J. R., G. E. Loeb, B. Z. Allison, E. Donchin, O. F. do Nascimento, *et al.*, 2006 Bci meeting 2005-workshop on signals and recording methods. *IEEE Transactions on neural systems and rehabilitation engineering* **14**: 138–141.
- Yang, B.-h., L.-f. He, L. Lin, and Q. Wang, 2015 Fast removal of ocular artifacts from electroencephalogram signals using spatial constraint independent component analysis based recursive least squares in brain-computer interface. *Frontiers of Information Technology & Electronic Engineering* **16**: 486–496.

How to cite this article: Erkan, E., and Erkan, Y. Ocular Artifact Removal Method Based on the Wavelet and ICA Transform. *Chaos Theory and Applications*, 5(2), 111-117, 2023.

Design of a New Chaotic System with Sine Function: Dynamic Analysis and Offset Boosting Control

Rameshbabu Ramar ^{*},¹

^{*}Department of Electronics and Communication Engineering, VSB Engineering College, Tamilnadu, India.

ABSTRACT A new chaotic system is presented in this research work. The proposed system has three nonlinear terms and one sine term which improves the complexity of the system. The basic properties of new system such as Lyapunov exponent, equilibrium point and stability are analyzed in detail. The dynamic analysis is conducted using classic tools such as bifurcation diagram and Lyapunov exponent plot to verify the chaotic nature in the proposed system. The changes in the states of the system is verified using bifurcation diagram and Lyapunov exponent plot. The proposed system presents some special features such as two wing attractors, forward and reverse periodic doubling bifurcation, and dc offset boosting control. The dc offset boosting behavior can be used to diagnosis the multistability behaviour in the dynamical system and to reduce the number of components in the communication system. This special feature converts the bipolar signal in to unipolar signal which can be used in many engineering applications. The theoretical study and the simulation results show that the proposed system has wealthy chaotic behaviour itself. Furthermore, the adaptive synchronization of identical new system is achieved for the application of secure communication system.

KEYWORDS

Chaotic system
Sine function
Dynamic analysis
Offset boosting
Adaptive synchronization

INTRODUCTION

Since Lorenz discovered a chaotic system in 1963, the generation of chaotic system becomes hot research topic due to their complex behaviour such as unpredictability, variation due to initial conditions etc. The chaotic systems have wide range of applications in crypto systems (Zia *et al.* 2022; El-Latif *et al.* 2022; Lin *et al.* 2022), secure communication (Kumar and Singh 2022; Zhou and Tan 2019) mobile robots (Nwachiona and Pérez-Cruz 2021; Cetina-Denis *et al.* 2022), Circuit applications (Lai *et al.* 2021; Wang *et al.* 2015), IOT applications (Li *et al.* 2022a; Trujillo-Toledo *et al.* 2021) etc. Due to these applications, recently many researchers introduced new 3D chaotic systems (Veeman *et al.* 2022; Hu *et al.* 2022a; Ablay 2022; Ramakrishnan *et al.* 2022).

The traditional chaotic system has low degree of complexity and it leads to the limitation of usage of chaotic system to solve some practical problems. The complex dynamic behaviour of chaotic system is required for various engineering applications such as image encryption, voice encryption, DCSK, particle motion

and secure communication etc. Therefore, the construction of chaotic system using trigonometry function is hot research topic and many researchers proposed chaotic systems based on product trigonometric function (Yu and Yu 2020; Yu and Gong 2022; Sriram *et al.* 2023), hyperbolic sine (Liu *et al.* 2018; Mobayen *et al.* 2020; Hu *et al.* 2022b; Joshi and Ranjan 2020), hyperbolic cosine (Signing *et al.* 2019; Signing and Kengne 2018), cosine function (Yan *et al.* 2022) and tangent and cotangent (Guo and Liang 2021).

Recently, many researchers introduced sine function based chaotic systems for example, Zhou *et al.* (2021) proposed a new autonomous chaotic system with sine function and analysed co-existing nested multiple attractors behaviour for different initial conditions. Kuate and Fotsin (2020) described a new five term chaotic system with one sine nonlinearity term which produces one scroll and double scroll attractor and also analysed its co-existing attractor using dc offset boosting method. Yang *et al.* (2021) presented a sine chaotic system which generates multi - scroll attractors and observed both homogeneous and heterogeneous multi stability in the proposed system. Hua *et al.* (2018) introduced a one-dimensional sine chaotification model (SCM) and improved the complexity of three existing systems. Bao *et al.* (2020) proposed a 2D sine map and investigated initials - boosted coexisting attractors in the proposed system. Sahoo and Roy (2022) introduced a new technique to generate multi wing attractors from two wing

Manuscript received: 24 December 2022,

Revised: 11 June 2023,

Accepted: 21 July 2023.

¹rrameshbabu15@gmail.com (Corresponding author)

existing chaotic attractors. The proposed technique uses a nonlinear function with sine term to generate multi wing attractors from existing Lu and Chen system. Volos *et al.* (2021) proposed a dynamical system with sine function and observed hidden attractors in the proposed system.

In the past few decades, the chaos synchronization has great attention since it can be used to solve many issues in secure communication system. Recently, various adaptive synchronization scheme Rahman and Jasim (2022); Roldán-Caballero *et al.* (2023); Pal *et al.* (2022); Li *et al.* (2022b) have been developed for the application of secure communication system.

This motivates me in this study to construct another trigonometry function based chaotic system. The proposed system presents offset boosting control property which means the position of the attractor can be easily controlled by adding a controller with any one of the state signals of the system. The offset boosting control method can also be used to identify the multistability of the dynamical system.

The proposed system has the following features:

- The proposed system produces two wing attractors.
- The proposed system is constructed using sine term which presents complex behaviour.
- The system presents both forward and reverse periodic doubling bifurcation.
- It presents dc offset boosting property that is the attractor of proposed system is position controllable.

INTRODUCTION OF SINE FUNCTION BASED NEW CHAOTIC SYSTEM

In 2017, Lai *et al.* (2017) introduced a new chaotic system as given in Equation. (1).

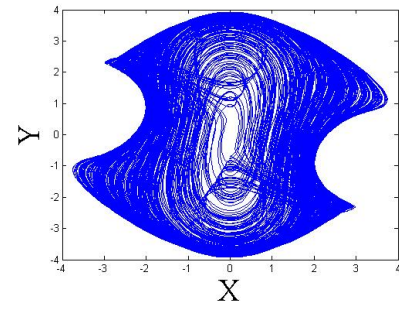
$$\begin{aligned} \dot{x} &= ax - yz \\ \dot{y} &= -by + xz \\ \dot{z} &= xyz - cz + d \end{aligned} \quad (1)$$

where, $(a, b, c, d) = (4, 9, 4, 4)$. The Lyapunov exponents of the system (1) are calculated as $l_1 = 1.7729$, $l_2 = 0$, $l_3 = -7.5549$. The Lyapunov dimension is $D_L = 2.2334$. The system (1) presents one scroll attractors. In this paper, the new chaotic system is designed by replacing the term y by $\sin(x)$ in second equation and the term xyz by xy in third equation of system (1). The new system (2) produces two scroll attractors while the old system (1) produces one scroll attractor and infinitely many shifted attractors.

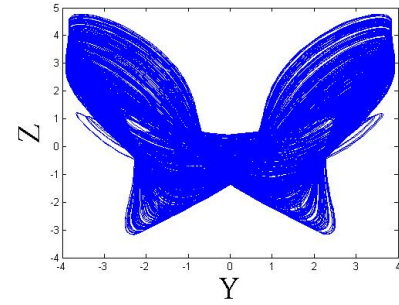
Thus, the new chaotic system with sine term can be modelled as in Equation. (2).

$$\begin{aligned} \dot{x} &= ax - kyz \\ \dot{y} &= b\sin x + xz \\ \dot{z} &= gxy - cz + d \end{aligned} \quad (2)$$

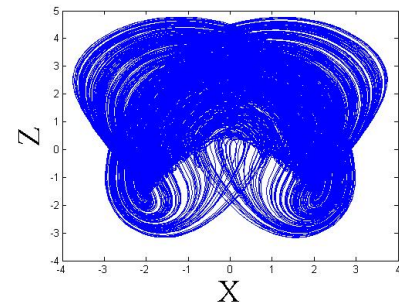
Here x , y , and z are the signal variables of new system (2) and a, b, c, d, g and k are the positive and non-zero parameters. The system (2) has the parameter values as, $a = 1.5$, $b = 10$, $c = 4$, $d = 2$, $g = 4$ and $k = 2$.



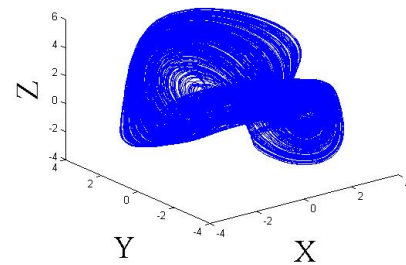
(a) xy plane



(b) yz plane



(c) xz plane

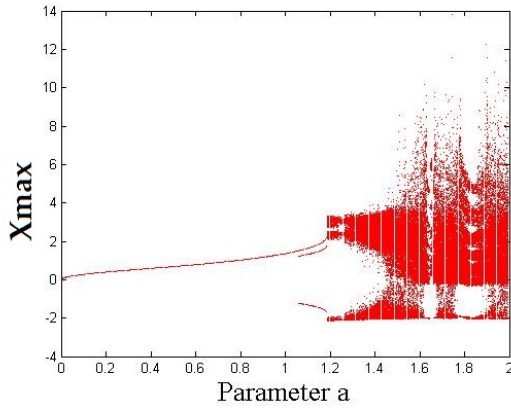


(d) xyz plane

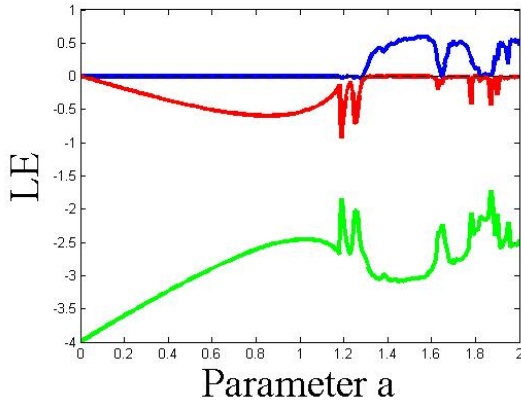
Figure 1 The two wing attractors of new chaotic system with sine term.

BASIC INFORMATION ABOUT THE NEW CHAOTIC SYSTEM WITH SINE TERM

In this section, the basic information about the proposed chaotic system such as, Lyapunov exponents, dissipative, equilibrium points, stability and the sensitivity to the initial conditions are discussed in detail.



(a) Bifurcation diagram



(b) Lyapunov exponent spectrum

Figure 2 (a) Bifurcation diagram (b) Lyapunov exponent spectrum of system (2) under parameter a with initial condition $(-1, 0, 1)$.

Lyapunov Exponents (LE) are calculated numerically using Wolf algorithm and MATLAB with the initial conditions $(-1, 0, 1)$ and simulation time 10000 sec. The system (2) has Lyapunov exponent value as, $(LE_1, LE_2, LE_3) = (0.561522, 0, -3.061664)$. Since, the proposed system satisfies the conditions that $LE_1 > 0, LE_2 = 0$ and $LE_3 < 0$, it is found that the system (2) has the chaotic behaviour itself.

Lyapunov dimension (D_L) of system (2) can be calculated using (3) as,

$$D_L = 2 + \frac{LE_1 + LE_2}{|LE_3|} = 2.183 \quad (3)$$

which indicates that the system (2) has fractional dimension. The dissipative nature of the system (2) can be verified using (4) as,

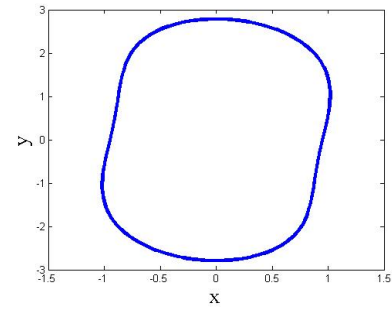
$$\nabla V = \frac{\partial V}{\partial x} + \frac{\partial V}{\partial y} + \frac{\partial V}{\partial z} = a - c = -2.5 \quad (4)$$

The dissipative nature of the dynamic system can also be verified by adding all their Lyapunov exponent values as (5),

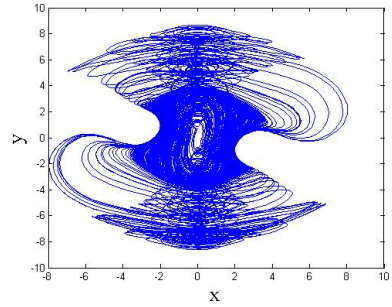
$$LE_T = LE_1 + LE_2 + LE_3 = -2.5 \quad (5)$$

The negative values of LE_T indicates that the proposed system (2) is dissipative.

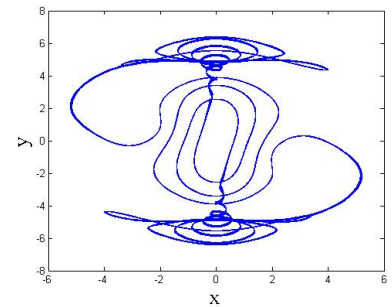
The equilibrium (E) points are calculated by letting $\dot{x}=\dot{y}=\dot{z}=0$ in the proposed system (2) and by solving those equations. Thus the



(a) $a = 0.8$



(b) $a = 1.6$



(c) $a = 1.8$

Figure 3 Various periodic and chaotic attractors of system (2) under the parameter $a \in [0, 2]$.

system (2) can be written as in (6) and the solution of (6) gives the equilibrium point as, $E = (0, 0, 0.5)$.

$$\begin{aligned} ax - kyz &= 0 \\ b \sin x + xz &= 0 \\ gxy - cz + d &= 0 \end{aligned} \quad (6)$$

Now, Jacobian Matrix (J) of the system (2) can be written as in (7),

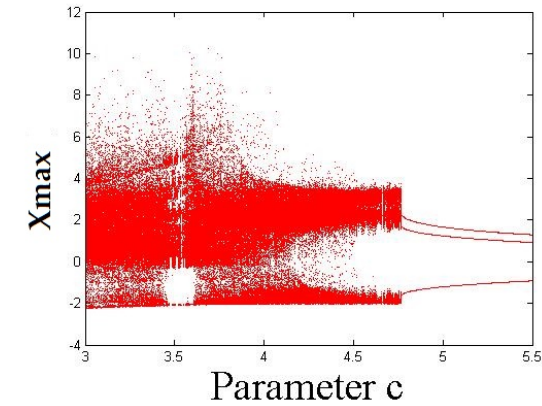
$$J = \begin{vmatrix} a & -kz & -ky \\ z + b \cos x & 0 & x \\ gy & gx & -c \end{vmatrix} \quad (7)$$

By substituting the equilibrium point (E) and the corresponding

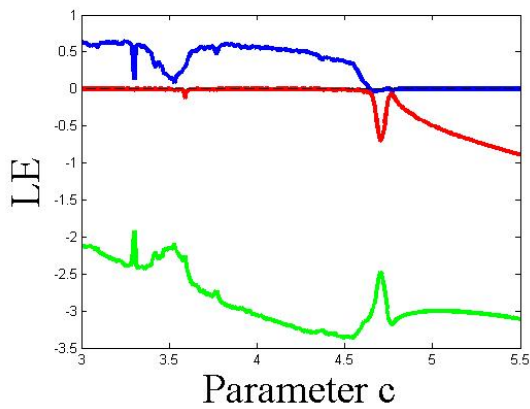
parameter values in (7),

$$J(E) = \begin{vmatrix} 1.5 & -1 & 0 \\ 10.5 & 0 & 0 \\ 0 & 0 & -4 \end{vmatrix} \quad (8)$$

The eigen values (λ) can be calculated from (8) as $\lambda_{1,2} = 0.75 \pm j3.152$, $\lambda_3 = -4$ which indicates that the equilibrium point (E) is saddle which is always unstable. The attractors of proposed system (2) in 2D and 3D plane are displayed in Figure 1.



(a) Bifurcation diagram

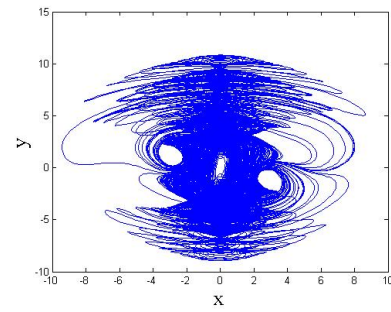


(b) Lyapunov exponent spectrum

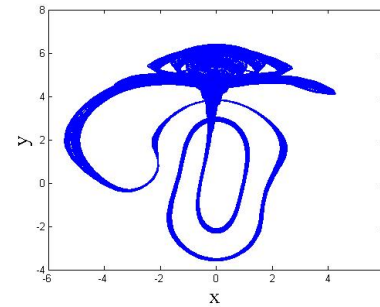
Figure 4 (a) Bifurcation diagram (b) Lyapunov exponent spectrum of system (2) under parameter c with initial condition $(-1, 0, 1)$.

DYNAMIC ANALYSIS OF NEW CHAOTIC SYSTEM WITH SINE FUNCTION

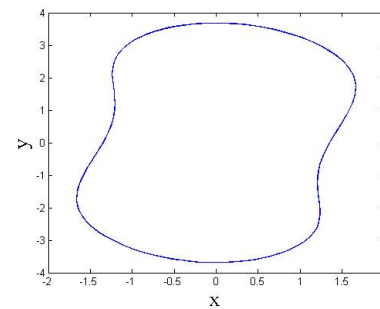
In this section, the bifurcation diagram and Lyapunov spectrum are investigated in order to prove the rich dynamics in the new system. Both plots can be obtained by varying any one of the system parameters and keeping remaining parameters with constant values. The state of the chaotic system may change from periodic to chaotic or chaotic to period depends on the system parameter values. This change in the states can be observed using bifurcation diagram and Lyapunov exponent spectrum plot under various



(a) $c = 3$



(b) $c = 3.5$



(c) $c = 5$

Figure 5 Various periodic and chaotic attractors of system (2) under the parameter $c \in [3, 5.5]$.

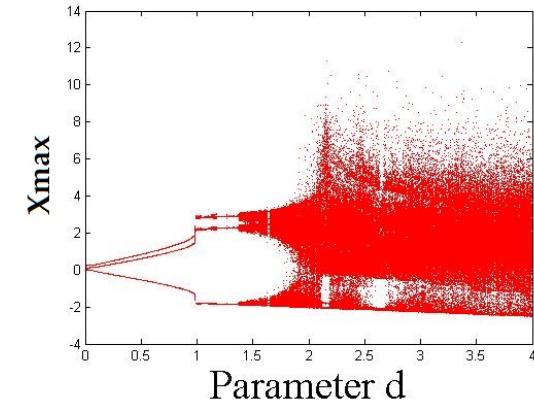
system parameters. In Lyapunov exponent spectrum, the positive Lyapunov exponents region indicates the chaotic attractor and other regions indicate the periodic attractor. The LE_1 , LE_2 and LE_3 are represented using blue, red and green colours respectively.

Figure 2 shows the bifurcation diagram and corresponding Lyapunov exponents spectrum for parameter a in the region $a \in [0, 2]$ and indicates that the system has periodic attractor up to $a = 1.3$ and chaotic attractor for the region $a \in [1.4, 1.6]$. Figure 3 represents the periodic and chaotic attractors of system (2) under the parameter $a \in [0, 2]$ and $(b, c, d, g, k) = (10, 4, 2, 4, 2)$.

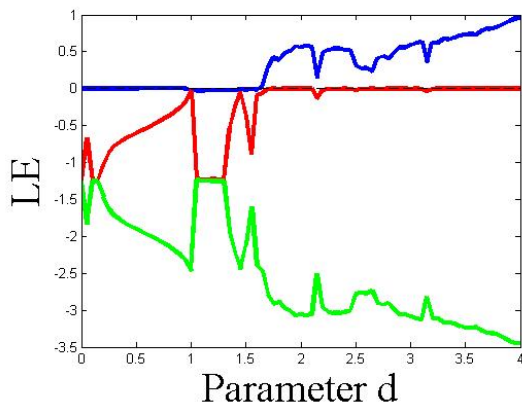
Figure 4 shows the bifurcation diagram and Lyapunov exponent spectrum for the parameter c in the region $c \in [3, 5.5]$. The state of the system is changed from chaotic to periodic beyond $c = 4.5$ when the parameter value is increased. Figure 5 represents some of the periodic and chaotic attractors of system (2) under the parameter $c \in [3, 5.5]$ and $(a, b, d, g, k) = (1.5, 10, 2, 4, 2)$.

Figure 6 shows the bifurcation diagram and Lyapunov exponent spectrum for another parameter d in the region $d \in [0, 4]$ and also shows that the system has chaotic flow beyond $d = 1.75$. Figure 7 represents the periodic and chaotic attractors of system (2) under

the parameter $d \in [0, 4]$ and $(a, b, c, g, k) = (1.5, 10, 4, 4, 2)$.



(a) Bifurcation diagram



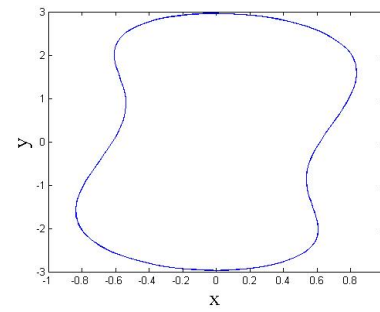
(b) Lyapunov exponent spectrum

Figure 6 (a) Bifurcation diagram (b) Lyapunov exponent spectrum of system (2) under parameter d with initial condition $(-1, 0, 1)$.

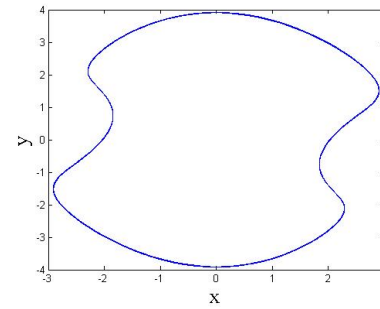
Figure 8 shows the bifurcation diagram and Lyapunov exponent spectrum for the parameter g in the region $g \in [3, 5.5]$. Figure 8 indicates that the system has chaotic attractors in the region $g \in [3, 4.2]$ and then periodic attractors. It is evident from Figures 6 and 8 that the proposed system experiences both forward and reverse periodic doubling behaviour. Figure 9 represents the periodic and chaotic attractors of system (2) under the parameter $g \in [2, 6]$ and $(a, b, c, d, k) = (1.5, 10, 4, 2, 2)$.

OFFSET BOOSTING CONTROL

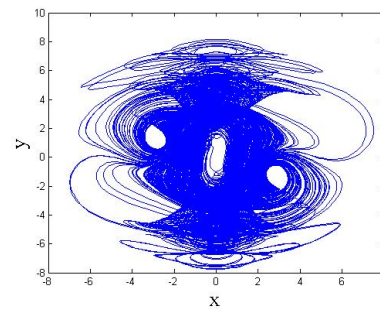
Offset boosting control [Chunbiao et al. \(2021\)](#); [Ma et al. \(2021\)](#); [Wen et al. \(2021\)](#) is the important property of chaotic system which is used to find the multistability of the system. It is observed in the system (2) when we introduce the offset booster m in the state signal y as given in Equation. (9). When the value of the booster m is varied, the proposed attractor becomes bipolar to unipolar as shown in Figure 10. Figures (10a - 10b) show the offset boosted attractor of system (2) in xy and yz plane for $m = -10$ (Red), $m = 0$ (Blue) and $m = 10$ (Green) respectively. Figure 10c represents the Lyapunov exponent plot of system (9) in the region $m \in [-20, 20]$. Figure 10c also represents that the system (9) has constant Lyapunov exponent in the specified region and the offset



(a) $d = 0.5$



(b) $d = 1.4$

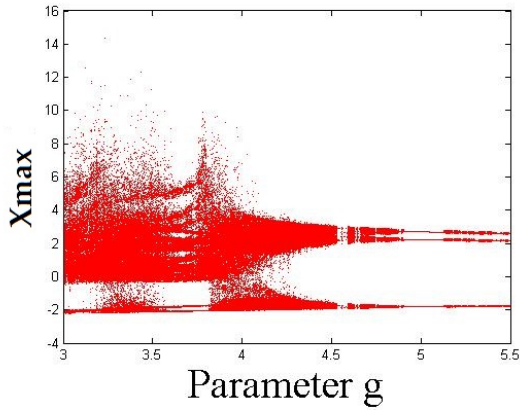


(c) $d = 3.5$

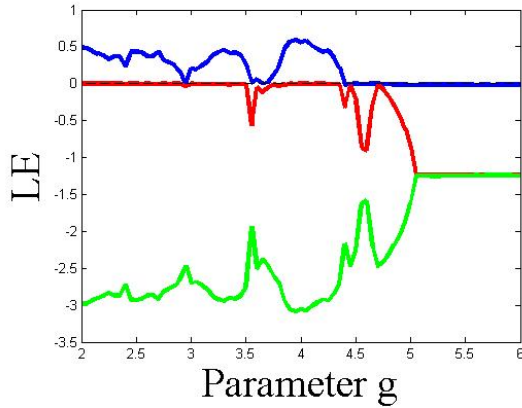
Figure 7 Various periodic and chaotic attractors of system (2) under the parameters $d \in [0, 4]$.

booster m does not modify the chaotic behavior of the proposed system (2).

$$\begin{aligned} \dot{x} &= ax - k(y + m)z \\ \dot{y} &= b \sin x + xz \\ \dot{z} &= gx(y + m) - cz + d \end{aligned} \quad (9)$$



(a) Bifurcation diagram



(b) Lyapunov exponent spectrum

Figure 8 (a) Bifurcation diagram (b) Lyapunov exponent spectrum of system (2) under parameter g with initial condition $(-1, 0, 1)$.

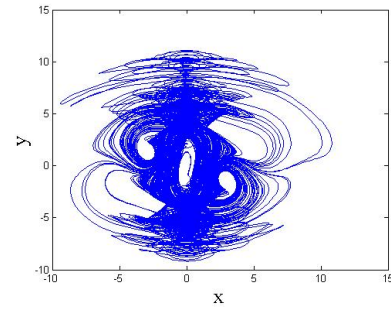
ADAPTIVE SYNCHRONIZATION

In this section, the adaptive synchronization between the proposed system is achieved using nonlinear feedback control methodology and master - slave scheme. The adaptive synchronization results are verified using Lyapunov stability theorem. The master and slave systems are considered as in (10) and (11) respectively.

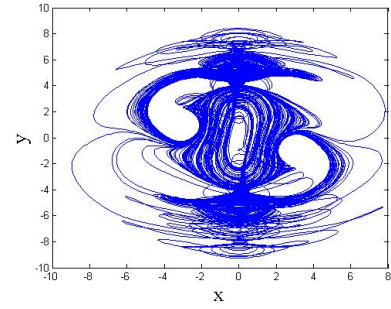
$$\begin{aligned} \dot{x}_1 &= ax_1 - ky_1z_1 \\ \dot{y}_1 &= b\sin x_1 + x_1z_1 \\ \dot{z}_1 &= gx_1y_1 - cz_1 + d \end{aligned} \quad (10)$$

$$\begin{aligned} \dot{x}_2 &= ax_2 - ky_2z_2 + u_x \\ \dot{y}_2 &= b\sin x_2 + x_2z_2 + u_y \\ \dot{z}_2 &= gx_2y_2 - cz_2 + d + u_z \end{aligned} \quad (11)$$

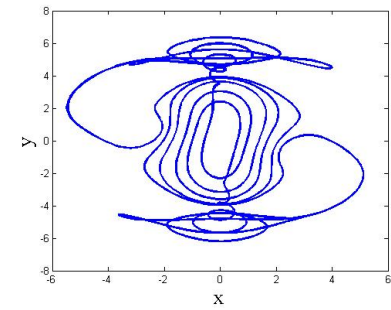
Here x_1, y_1, z_1 are the signal variables of master system, x_2, y_2, z_2 are the signal variables of slave system, u_x, u_y and u_z are the adaptive controllers to be designed. The adaptive synchronization errors can be written as, $e_x = x_2 - x_1, e_y = y_2 - y_1$ and $e_z = z_2 - z_1$. By



(a) $g = 2.5$



(b) $g = 3.5$



(c) $g = 3.6$

Figure 9 Various periodic and chaotic attractors of system (2) under the parameter $g \in [2, 6]$.

simple calculation, the adaptive controllers and the estimates of error dynamics can be obtained as given in (12) and (13) respectively.

$$\begin{aligned} u_x &= -\hat{a}e_x - \hat{k}(y_1z_1 - y_2z_2) - k_x e_x \\ u_y &= -\hat{b}(\sin x_2 - \sin x_1) - x_2z_2 + x_1z_1 - k_y e_y \\ u_z &= -\hat{g}(x_2y_2 - x_1y_1) + \hat{c}e_z - k_z e_z \end{aligned} \quad (12)$$

$$\begin{aligned} \dot{e}_x &= e_a e_x + e_k [y_1z_1 - y_2z_2] - k_x e_x \\ \dot{e}_y &= e_b [\sin x_2 - \sin x_1] - k_y e_y \\ \dot{e}_z &= e_g [x_2y_2 - x_1y_1] - e_c e_z - k_z e_z \end{aligned} \quad (13)$$

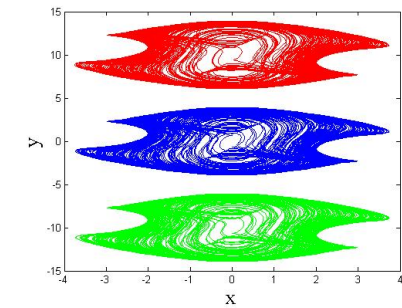
Here, $e_a = a - \hat{a}, e_b = b - \hat{b}, e_c = c - \hat{c}, e_g = g - \hat{g}, e_k = k - \hat{k}$ are the parameter errors, $\hat{a}, \hat{b}, \hat{c}, \hat{g}$ and \hat{k} are the estimates of unknown parameters a, b, c, g and k respectively and k_x, k_y and k_z are the gains of the controllers.

Now, consider Lyapunov stability function as given in (14),

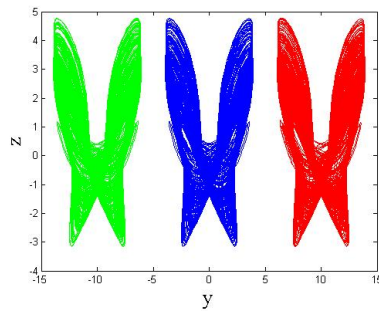
$$\begin{aligned} \dot{V} &= e_x \dot{e}_x + e_y \dot{e}_y + e_z \dot{e}_z + e_a \dot{e}_a + e_b \dot{e}_b + e_c \dot{e}_c + e_g \dot{e}_g + e_k \dot{e}_k \\ &= e_a [(e_x)^2 - \hat{a}] + e_k [e_x (y_1 z_1 - y_2 z_2) - \hat{k}] + \\ &e_b [e_y (\sin x_2 - \sin x_1) - \hat{b}] + e_g [e_z (x_2 y_2 - x_1 y_1) - \hat{g}] + \\ &e_c [-(e_z)^2 - \hat{c}] - [k_x (e_x)^2 + k_y (e_y)^2 + k_z (e_z)^2] \quad (14) \end{aligned}$$

The Eqn. (14) is a negative function when $\hat{a}=(e_x)^2$, $\hat{b} = e_y (\sin x_2 - \sin x_1)$, $\hat{c}=- (e_z)^2$, $\hat{k}=e_x (y_1 z_1 - y_2 z_2)$ and $\hat{g}=e_z (x_2 y_2 - x_1 y_1)$. The negative value of (14) represents that the system (2) is globally synchronized and the synchronization errors are globally bounded.

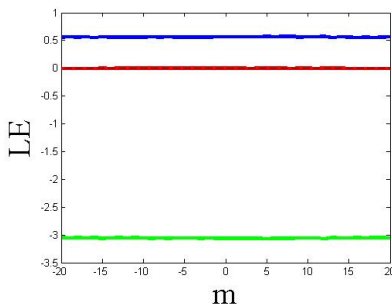
The results obtained for adaptive synchronization are verified using MATLAB software with the assumptions that the initial conditions for master and slave systems are $(-1, 0, 1)$ and $(1, -1, 1)$ respectively and gain of the controllers are $k_{x,y,z}=0.8$. Figure 11 shows the synchronization results obtained in this work. The state signals are synchronized after the time period $t = 11\text{sec}$ and hence the error signals reach zero after the time period $t = 11\text{sec}$.



(a) xy plane

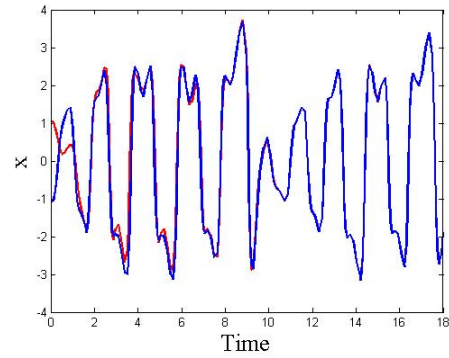


(b) yz plane

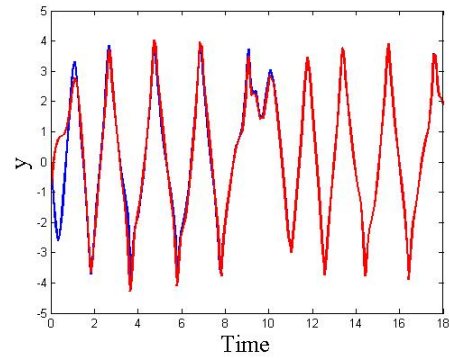


(c) Lyapunov exponent plot

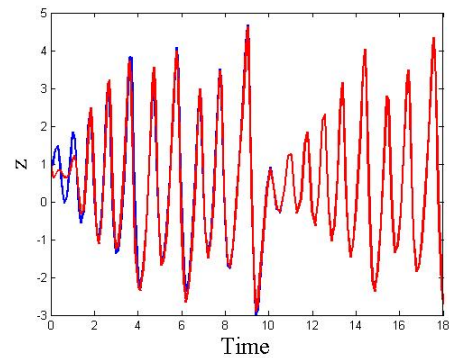
Figure 10 (a-b) Offset boosted attractors of system (2) with initial condition $(-1, 0, 1)$, (c) Lyapunov exponent plot of system (9).



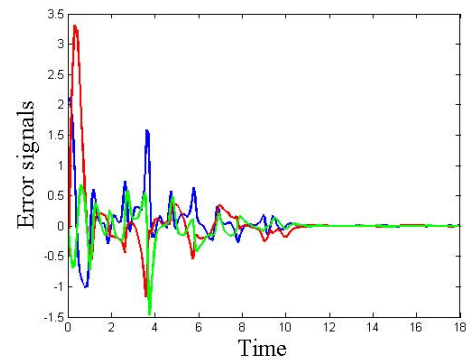
(a) Synchronized x signal



(b) Synchronized y signal



(c) Synchronized z signal



(d) Synchronized error signal

Figure 11 (a-c) Synchronized state variables of master (Blue) and slave (Red) system, (d) Synchronized error signals e_x (Blue), e_y (Red) and e_z (Green).

CONCLUSION

A new chaotic system with two wing attractor is developed. The proposed system satisfies the basic conditions required to be a chaotic such as unstable equilibrium point and at least one positive Lyapunov value. The chaotic nature in the proposed system is also verified using the bifurcation diagram, Lyapunov exponent plot and attractor diagram. The offset boosting control behavior of the new system is verified by means of attractor diagram and Lyapunov exponent plot. The offset boosted system has constant Lyapunov exponent values which means that the system maintain its chaotic nature for the various values of booster parameter. The adaptive controllers are designed for the adaptive synchronization of proposed system using feedback control method. All the state signal of proposed system can be synchronized and the synchronization errors become zero after the small time period. Due to these properties, the proposed system has complex dynamic behaviour, infinitely multiple attractors which can be used in many engineering applications.

Availability of data and material

Not applicable.

Conflicts of interest

The author declares that there is no conflict of interest regarding the publication of this paper.

LITERATURE CITED

- Ablay, G., 2022 New 4d and 3d models of chaotic systems developed from the dynamic behavior of nuclear reactors. *Chaos: An Interdisciplinary Journal of Nonlinear Science* **32**: 113108.
- Bao, H., Z. Hua, N. Wang, L. Zhu, M. Chen, *et al.*, 2020 Initials-boosted coexisting chaos in a 2-d sine map and its hardware implementation. *IEEE Transactions on Industrial Informatics* **17**: 1132–1140.
- Cetina-Denis, J. J., R. M. López-Gutiérrez, C. Cruz-Hernández, and A. Arellano-Delgado, 2022 Design of a chaotic trajectory generator algorithm for mobile robots. *Applied Sciences* **12**: 2587.
- Chunbiao, L., Y. Jiang, and M. Xu, 2021 On offset boosting in chaotic system. *Chaos Theory and Applications* **3**: 47–54.
- El-Latif, A. A. A., J. Ramadoss, B. Abd-El-Atty, H. S. Khalifa, and F. Nazarimehr, 2022 A novel chaos-based cryptography algorithm and its performance analysis. *Mathematics* **10**: 2434.
- Guo, H. and W. Liang, 2021 Existence of chaos for partial difference equations via tangent and cotangent functions. *Advances in Difference Equations* **2021**: 1–15.
- Hu, C., Q. Wang, X. Zhang, Z. Tian, and X. Wu, 2022a A new chaotic system with novel multiple shapes of two-channel attractors. *Chaos, Solitons & Fractals* **162**: 112454.
- Hu, X., B. Sang, and N. Wang, 2022b The chaotic mechanisms in some jerk systems. *AIMS Mathematics* **7**: 15714–15740.
- Hua, Z., B. Zhou, and Y. Zhou, 2018 Sine chaotification model for enhancing chaos and its hardware implementation. *IEEE Transactions on Industrial Electronics* **66**: 1273–1284.
- Joshi, M. and A. Ranjan, 2020 An autonomous simple chaotic jerk system with stable and unstable equilibria using reverse sine hyperbolic functions. *International Journal of Bifurcation and Chaos* **30**: 2050070.
- Kuate, P. D. K. and H. Fotsin, 2020 Complex dynamics induced by a sine nonlinearity in a five-term chaotic system: Fpga hardware design and synchronization. *Chaos: An Interdisciplinary Journal of Nonlinear Science* **30**: 123107.
- Kumar, A. and P. P. Singh, 2022 Synchronisation of unified chaotic systems using modified nonlinear active control: Circuit design, implementation, and secure communication. *IETE Journal of Research* pp. 1–17.
- Lai, Q., A. Akgul, C. Li, G. Xu, and Ü. Çavuşoğlu, 2017 A new chaotic system with multiple attractors: Dynamic analysis, circuit realization and s-box design. *Entropy* **20**: 12.
- Lai, Q., B. Bao, C. Chen, J. Kengne, and A. Akgul, 2021 Circuit application of chaotic systems: modeling, dynamical analysis and control.
- Lai, Q., Z. Wan, and P. D. Kamdem Kuate, 2020 Modelling and circuit realisation of a new no-equilibrium chaotic system with hidden attractor and coexisting attractors. *Electronics Letters* **56**: 1044–1046.
- Li, L., A. El-Latif, A. Ahmed, S. Jafari, K. Rajagopal, *et al.*, 2022a Multimedia cryptosystem for iot applications based on a novel chaotic system around a predefined manifold. *Sensors* **22**: 334.
- Li, S., Y. Wu, and G. Zheng, 2022b Adaptive synchronization for hyperchaotic liu system. *Frontiers in Physics* p. 745.
- Lin, C.-H., G.-H. Hu, J.-S. Chen, J.-J. Yan, and K.-H. Tang, 2022 Novel design of cryptosystems for video/audio streaming via dynamic synchronized chaos-based random keys. *Multimedia Systems* **28**: 1793–1808.
- Liu, J., J. Clinton Sprott, S. Wang, and Y. Ma, 2018 Simplest chaotic system with a hyperbolic sine and its applications in dcsk scheme. *IET Communications* **12**: 809–815.
- Ma, C., J. Mou, L. Xiong, S. Banerjee, T. Liu, *et al.*, 2021 Dynamical analysis of a new chaotic system: asymmetric multistability, offset boosting control and circuit realization. *Nonlinear Dynamics* **103**: 2867–2880.
- Mamia, S. B., W. Puech, and K. Bouallegue, 2022 Generation of chaotic attractors using neurons with multidentrines. *International Journal of Modelling, Identification and Control* **40**: 92–104.
- Mobayen, S., C. Volos, Ü. Çavuşoğlu, and S. S. Kaçar, 2020 A simple chaotic flow with hyperbolic sinusoidal function and its application to voice encryption. *Symmetry* **12**: 2047.
- Nwachiona, C. and J. H. Pérez-Cruz, 2021 Analysis of a new chaotic system, electronic realization and use in navigation of differential drive mobile robot. *Chaos, Solitons & Fractals* **144**: 110684.
- Pal, P., G. G. Jin, S. Bhakta, and V. Mukherjee, 2022 Adaptive chaos synchronization of an attitude control of satellite: A backstepping based sliding mode approach. *Heliyon* **8**: e11730.
- Pallav and H. Handa, 2022 Simple synchronization scheme for a class of nonlinear chaotic systems using a single input control. *IETE Journal of Research* pp. 1–14.
- Rahman, Z.-A. S. and B. H. Jasim, 2022 Hidden dynamics investigation, fast adaptive synchronization, and chaos-based secure communication scheme of a new 3d fractional-order chaotic system. *Inventions* **7**: 108.
- Ramakrishnan, B., H. Natiq, K. Rajagopal, S. Jafari, and F. Nazarimehr, 2022 A novel megastable system: Cloud, kite, and arrow-like attractors and their dynamics. *International Journal of Bifurcation and Chaos* **32**: 2250152.
- Roldán-Caballero, A., J. H. Pérez-Cruz, E. Hernández-Márquez, J. R. García-Sánchez, M. Ponce-Silva, *et al.*, 2023 Synchronization of a new chaotic system using adaptive control: Design and experimental implementation. *Complexity* **2023**.
- Sahoo, S. and B. K. Roy, 2022 Design of multi-wing chaotic systems with higher largest lyapunov exponent. *Chaos, Solitons & Fractals* **157**: 111926.

- Signing, V. F. and J. Kengne, 2018 Coexistence of hidden attractors, 2-torus and 3-torus in a new simple 4-d chaotic system with hyperbolic cosine nonlinearity. *International Journal of Dynamics and Control* **6**: 1421–1428.
- Signing, V. F., J. Kengne, and J. M. Pone, 2019 Antimonotonicity, chaos, quasi-periodicity and coexistence of hidden attractors in a new simple 4-d chaotic system with hyperbolic cosine nonlinearity. *Chaos, Solitons & Fractals* **118**: 187–198.
- Sriram, B., A. Ghaffari, K. Rajagopal, S. Jafari, and E. Tlelo-Cuautle, 2023 A chaotic map with trigonometric functions: Dynamical analysis and its application in image encryption based on sparse representation and convolutional filters. *Optik* **273**: 170379.
- Trujillo-Toledo, D., O. López-Bonilla, E. García-Guerrero, E. Tlelo-Cuautle, D. López-Mancilla, *et al.*, 2021 Real-time rgb image encryption for iot applications using enhanced sequences from chaotic maps. *Chaos, Solitons & Fractals* **153**: 111506.
- Veeman, D., M. Mehrabbeik, H. Natiq, K. Rajagopal, S. Jafari, *et al.*, 2022 A new chaotic system with coexisting attractors. *International Journal of Bifurcation and Chaos* **32**: 2230007.
- Volos, C., J.-O. Maaita, V.-T. Pham, and S. Jafari, 2021 Hidden attractors in a dynamical system with a sine function. *Chaotic Systems with Multistability and Hidden Attractors* pp. 459–487.
- Wang, R., H. Sun, J.-Z. Wang, L. Wang, and Y.-C. Wang, 2015 Applications of modularized circuit designs in a new hyperchaotic system circuit implementation. *Chinese Physics B* **24**: 020501.
- Wen, J., Y. Feng, X. Tao, and Y. Cao, 2021 Dynamical analysis of a new chaotic system: Hidden attractor, coexisting-attractors, offset boosting, and dsp realization. *Ieee Access* **9**: 167920–167927.
- Yan, S., B. Gu, Y. Ren, X. Sun, and E. Wang, 2022 Dynamical analysis of four-dimensional chaotic system and its application in image encryption. *Multimedia Tools and Applications* pp. 1–26.
- Yang, Y., L. Huang, J. Xiang, and Q. Guo, 2021 Three-dimensional sine chaotic system with multistability and multi-scroll attractor. *IEEE Transactions on Circuits and Systems II: Express Briefs* **69**: 1792–1796.
- Yu, W. and S. Gong, 2022 Chaotic system constructed by product trigonometric function and polynomial and applied to color image encryption. *Modern Physics Letters B* **36**: 2150534.
- Yu, W. and T. Yu, 2020 Analysis of chaotic characteristics of trigonometric function system. *Modern Physics Letters B* **34**: 2050210.
- Zhou, L. and F. Tan, 2019 A chaotic secure communication scheme based on synchronization of double-layered and multiple complex networks. *Nonlinear Dynamics* **96**: 869–883.
- Zhou, L., Z. You, and Y. Tang, 2021 A new chaotic system with nested coexisting multiple attractors and riddled basins. *Chaos, Solitons & Fractals* **148**: 111057.
- Zia, U., M. McCartney, B. Scotney, J. Martinez, M. AbuTair, *et al.*, 2022 Survey on image encryption techniques using chaotic maps in spatial, transform and spatiotemporal domains. *International Journal of Information Security* **21**: 917–935.

How to cite this article: Ramar, R. Design of a New Chaotic System with Sine Function: Dynamic Analysis and Offset Boosting Control. *Chaos Theory and Applications*, 5(2), 118-126, 2023.

Dynamical Analysis and Electronic Circuit Implementation of Fractional-order Chen System

Abdullah Gokyildirim ^{*,1}

*Department of Electrical and Electronics Engineering, Bandirma Onyedi Eylul University, Bandirma, Balıkesir, 10200, Türkiye.

ABSTRACT In the last decade, there has been a notable increase in research focus on fractional calculus and its applications. Fractional-order analysis shows promise in enriching the dynamic behavior of chaotic systems. This paper focuses on the dynamic analysis of the Chen system with low fractional-order values and its fractional-order electronic circuit. Notably, there is a lack of studies about chaotic electronic circuits in the literature with a fractional-order parameter value equal to 0.8, which makes this study pioneering in this regard. Moreover, necessary numerical analyses are presented to investigate the system's dynamic characteristics and complexity, such as chaotic phase planes, Lyapunov spectra, and bifurcation diagrams. As expected, oscilloscope views of the electronic circuit realization align with the numerical analysis and PSpice simulation results.

KEYWORDS

Chaos
Chen system
Fractional-order system
Bifurcation
Electronic circuit implementation

INTRODUCTION

Fractional calculus offers greater dynamic richness for chaotic systems. Even a small change in the fractional order of a chaotic system can lead to entirely new bifurcation diagrams. Therefore, in recent years, researchers have studied numerous implementations of chaotic systems in both digital and analog domains, considering different fractional-order values (Yang and Wang 2021; Wang *et al.* 2021; Li *et al.* 2020; Gokyildirim *et al.* 2023; Liu *et al.* 2021; Chen *et al.* 2013; Pham *et al.* 2017). Gokyildirim presented an electronic circuit for the Sprott K system using discrete circuit elements with a fractional-order value of 0.8 (Gokyildirim 2023).

Altun presented research that involved studying numerical computations of fractional-order Rössler and Sprott H systems, as well as their hardware implementations using field-programmable analog array (FPAA) technology (Altun 2021a). In reference (Silva-Juárez *et al.* 2020), FPAA-based applications of fractional-order chaotic systems were realized with active filters, particularly for a fractional-order parameter q value equal to 0.9. Moreover, the fractional-order Sprott H system was utilized to generate a multi-scroll attractor exhibiting hyperchaotic behavior, and its implementation utilizing FPAA was illustrated in (Altun 2022). In another study (Altun 2021b), a field-programmable gate array (FPGA) is

used for the implementation of a fractional-order system. The works of Dang focused on studying the fractional-order designs of E (Dang 2014b) and N (Dang 2014a) systems presented by Julien Sprott in 1994 (Sprott 1994). Digital designs of chaotic systems present various benefits in terms of high performance and cost-effectiveness. However, when integrating fractional-order chaotic systems, the limited memory capacity of microcontrollers can potentially impact their overall performance. This limitation arises because the parameter of fractional-order serves as an indicator of memory (Du *et al.* 2013).

Some researchers have focused their studies on the fractional-order analysis of the Chen system and its engineering applications (Li and Peng 2004; Lu and Chen 2006). In their research, Nuñez-Perez *et al.* introduced the use of different optimization algorithms to amplify the chaotic behavior of the fractional-order chaotic Chen system (FOCHEN) (Nuñez-Perez *et al.* 2021). The outcomes demonstrate that the optimized FOCHEN systems exhibit higher maximum Lyapunov exponents compared to the non-optimized system. Ozkaynak *et al.* designed a new since substitution box (S-box) using the Fractional-order Chen system with a predictor-corrector scheme (Özkaynak *et al.* 2017). The study indicates that utilizing the FOCHEN system can enhance the performance of the S-box. Zouad *et al.* designed a secure communication electronic circuit using the delayed FOCHEN system with the Multisim simulation program (Zouad *et al.* 2019). Wang *et al.* present the development of a nonstandard finite discretization scheme for the FOCHEN system's numerical solutions (Wang *et al.* 2020). All the

Manuscript received: 12 July 2023,

Revised: 28 July 2023,

Accepted: 30 July 2023.

¹agokyildirim@bandirma.edu.tr (Corresponding author)

studies mentioned above have successfully achieved analog or digital implementations of chaotic systems with fractional orders. However, a common characteristic observed in analog implementation studies is their focus on fractional-order parameters that are greater than 0.8. The primary contribution of this paper is the construction of the FOCHEN system's electronic circuit for using standard components. Notably, this study focuses on achieving the lowest feasible value ($q = 0.8$) of fractional-order, which has only had a few examples in the literature. For this purpose, the fractional-order values of the FOCHEN system that exhibit chaotic behavior are decided through bifurcation analyses.

The organization of this study is as follows: Section 2 presents the dynamical equations of the FOCHEN system and provides a concise introduction to fractional calculus. In Section 3, some dynamics of the fractional-order system are presented, such as phase planes, Lyapunov spectra, and bifurcation diagrams. Section 4 presents the construction of an electronic circuit for the fractional-order system on a breadboard, along with a comparison between oscilloscope outputs and PSpice simulation results. The final section contains the conclusion.

CHEN CHAOTIC SYSTEM WITH LINEAR SCALING AND FRACTIONAL CALCULUS

In 1999, Chen and Ueta presented a chaotic attractor that is a special case of the Lorenz system (Chen and Ueta 1999). The system has seven terms and three constant parameters, as shown in the following equation:

$$\begin{aligned}\dot{x} &= a(y - x) \\ \dot{y} &= (c - a)x - xz + cy \\ \dot{z} &= xy - bz\end{aligned}\quad (1)$$

To enable the implementation of an electronic circuit, linear scaling is required in the original Chen system, as the output values of state variables x , y , and z exceed the necessary limitations. If the system is linearly scaled to maintain the output voltages of the electronic circuit between -5V and +5V, the differential equations of the system (1) are rewritten as follows:

$$\begin{aligned}\dot{x} &= a(y - x) \\ \dot{y} &= (c - a)x - 10xz + cy \\ \dot{z} &= 10xy - bz\end{aligned}\quad (2)$$

In this form, the variables are rescaled as $x = 10v_x/V$, $y = 10v_y/V$, and $z = 10v_z/V$. The system (2) produces chaotic signals when a , b and c are 35, 3 and, 28, respectively, with initial conditions $x(0) = 0$, $y(0) = 1$, and $z(0) = 0$.

In fractional calculus, the concept of non-integer differentiation and integration is introduced, allowing us to analyse and model complex phenomena with non-integer dynamics. The fractional-order derivatives and integrals are represented using The fractional-order elementary operator ${}_a D_t^q$, where t and a are the limits of the operation, and q is a real number representing the fractional-order. Depending on the value of q , these operators can act as fractional-order differentiators (fractional derivatives) or fractional-order integrators (fractional integrals). Fractional calculus provides a powerful mathematical tool to describe complex processes that cannot be fully captured by classical integer-order calculus. The continuous-time fractional-order operator is expressed as follows:

$${}_a D_t^q = \begin{cases} \frac{d^q}{dt^q}; & \text{Re}(q) > 0, \\ 1; & \text{Re}(q) = 0, \\ \int_a^t (d\tau)^{-q}; & \text{Re}(q) < 0. \end{cases}\quad (3)$$

Equivalent definitions for the fractional operator ${}_a D_t^q$ are various mathematical representations used to describe the behavior of fractional calculus. Some of these definitions include Grünwald-Letnikov, Riemann-Liouville, Caputo, Grünwald-Letnikov Matrix, Marchaud, and Weyl definitions. Among these, the initial conditions of the Caputo fractional definition resemble those of differential equations with integer order. As a result, Caputo's definition is selected for the fractional derivative calculations of bifurcation diagrams and phase portraits in this study. The Caputo method is defined as follows:

$${}_a D_t^q f(t) = \left\{ \frac{1}{\Gamma(n-q)} \left(\frac{d}{dt} \right)^n \int_a^t (t-\tau)^{n-q-1} f^n(\tau) d\tau \right. \quad (4)$$

where $n - 1 < q < 1$. The Laplace transform of the Caputo definition is represented as follows:

$$H(s) = L \left\{ \frac{d^q f(t)}{dt^q} \right\} = s^q L \{ f(t) \} \quad (5)$$

Under the assumption of zero initial conditions, the transfer function $H(s)$ is established as a linear fractional-order integrator with $H(s) = 1/s^q$. Moreover, eq. (6) provides fractional derivatives' generalized Laplace transform with order $q > 0$.

$$L \left\{ {}_0 D_t^q f(t) \right\} = s^q F(s) \quad (6)$$

Thus, the differential equations of the FOCHEN system are written as follows:

$$\begin{aligned}D_t^{q_1} x &= a(y - x) \\ D_t^{q_2} y &= (c - a)x - 10xz + cy \\ D_t^{q_3} z &= 10xy - bz\end{aligned}\quad (7)$$

THE FOCHEN SYSTEM'S DYNAMICAL ANALYSES

In this Section, the required dynamical analyses of the FOCHEN system, including Lyapunov spectra, bifurcation diagrams, and phase planes, are thoroughly investigated. In this manner, the chaotic behavior and dynamic properties of the system (7) can be observed. However, solving a nonlinear fractional-order system analytically presents challenges. As a consequence, various methods have emerged to address these systems, including the utilization of MATLAB-based tools such as FOMCON (Tepljakov and Tepljakov 2017), fde12 (Garrappa 2018), and ninteger (Valerio and Da Costa 2004). In this section, the fde12 toolbox is used to perform all dynamical analyses and simulations, excluding the Lyapunov spectra analysis.

Bifurcation diagrams are used to understand and analyze the behaviors of complex systems. Especially in chaotic systems, bifurcation diagrams are essential tools to explore and analyze the system's different behaviors. On the other hand, Lyapunov exponents are valuable analysis tools used to understand and predict the nature of chaotic systems and the transitions between order and disorder. Figures 1, 2, and 3 illustrate the Lyapunov Exponents and corresponding bifurcation diagrams for both the fractional-order and integer-order versions of Chen system for $b = 3$ and

$c = 28$. In the figures, initial conditions are $x(0) = 0, y(0) = 1$, and $z(0) = 0$. Additionally, Figure 4 displays the phase planes of the Chen system (2) and the FOCHEN system (7) based on the bifurcation diagrams. In contrast to other numerical analyses in this study, the Lyapunov exponents are calculated using the Grünwald-Letnikov method (Li et al. 2023; Hosny et al. 2022).

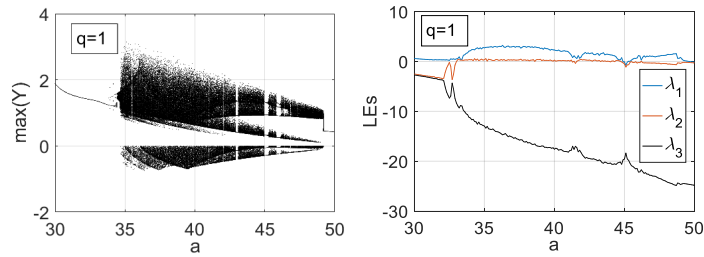


Figure 1 Integer-order Chen system's Bifurcation diagram and Lyapunov spectra.

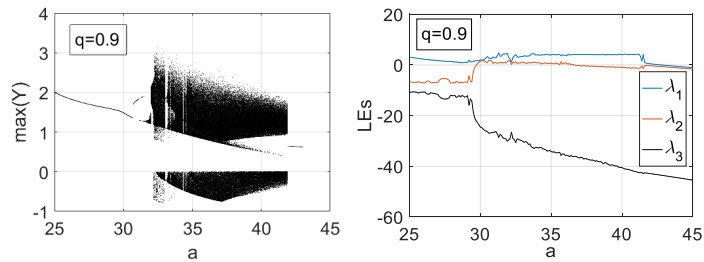


Figure 2 Bifurcation diagram and Lyapunov spectra of FOCHEN system for $q = 0.9$.

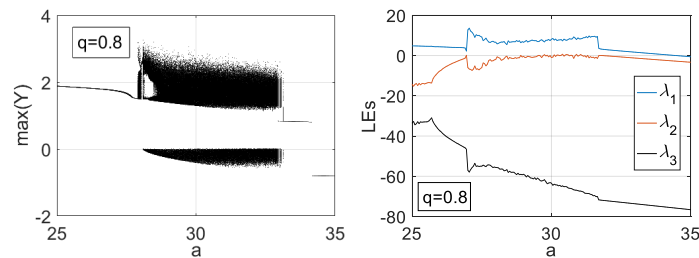


Figure 3 Bifurcation diagram and Lyapunov spectra of FOCHEN system for $q = 0.8$.

ELECTRONIC CIRCUIT IMPLEMENTATION OF THE FOCHEN SYSTEM

The implementation of fractional-order chaotic systems in electronic circuits is important for analyzing system behaviors and controlling complex dynamics. The electronic circuits of fractional-order chaotic systems refer to the electronic implementations of systems with complex dynamics represented by differential equations with fractional degrees (q). These systems offer more versatility and diversity compared to traditional integer-order differential equations. The realization of electronic circuits for fractional-order chaotic systems provides significant advantages in various engineering applications. These systems exhibit nonlinear and random behaviors, making them suitable for randomization and security-based applications. Additionally, fractional-order chaotic systems

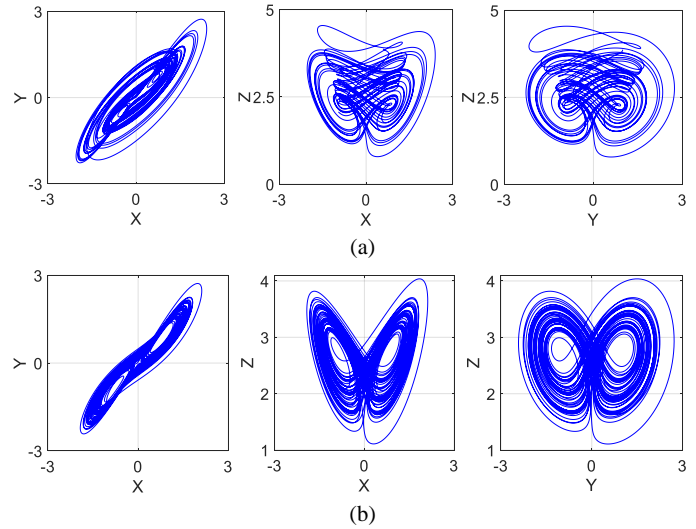


Figure 4 Phase planes of integer-order and fractional-order chaotic systems for $t(s) \in [0.1, 20]$: (a) $q = 1, a=35, b = 3, c = 28$, and $t(s) \in [0.6, 20]$, (b) $q = 0.8, a = 30, b = 3, c = 28$, and $t(s) \in [0.1, 20]$.

can be used as functions that randomly mix signals and increase entropy.

In electronic circuits, the basic elements of fractional-order chaotic systems are fractional-order circuit components. These components have different mathematical properties compared to traditional resistors, capacitors, and inductors and are expressed by the fractional degree (q). Fractional-order circuit elements are used for the electronic implementations of fractional-order differential equations.

An electronic circuit of the FOCHEN for (q)=0.8 is implemented with standard components, in this section. According to circuit theory (Podlubny 1999), an electronic circuit that exhibits dynamics of non-integer order is referred to as a "fractance". To realize a chaotic system's electronic circuit implementation, resistor-capacitor (RC) systems obtained from the approximate transfer function are utilized. Researchers commonly use three approaches, namely chain fractance, domino ladder, and binary tree in their studies. In this research, the chain fractance approach is employed for fractional-order circuits. In this approach, there are N serial RC pairs, where N denotes the number of layers. The transfer function of the chain fractance in the Laplace domain is expressed as following equation, based on the two-port network theory (Yao et al. 2020; Ahmad and Sprott 2003):

$$H^{RC}(s) = \frac{1}{C_1s + \frac{1}{R_1}} + \frac{1}{C_2s + \frac{1}{R_2}} + \dots + \frac{1}{C_Ns + \frac{1}{R_N}} \quad (8)$$

By utilizing eq. (5), the transfer function of the chain fractance for $q = 0.8$ is written as follows:

$$\frac{1}{s^{0.8}} \approx \frac{5.3088(s + 0.1333)(s + 2.371)(s + 42.17)(s + 750)}{(s + 0.01333)(s + 0.2371)(s + 4.217)(s + 75)(s + 1333)} \quad (9)$$

Considering eq. (9), Table 1 depicts the values of passive circuit elements for the fractional-order module with $q = 0.8$

Table 1 The values of passive circuit elements required for the fractional-order module of the FOCHEN system

Component	Value
R_a	17.9 k Ω
R_b	17.075 k Ω
R_c	170.6 k Ω
R_d	1.756 M Ω
R_e	37.865 M Ω
C_a	418.83 pF
C_b	780.955 pF
C_c	1.39 nF
C_d	2.4 nF
C_e	1.98 nF

Taking into account Table 1, the fractional-order module's electronic circuit is constructed as shown in Figure 5.

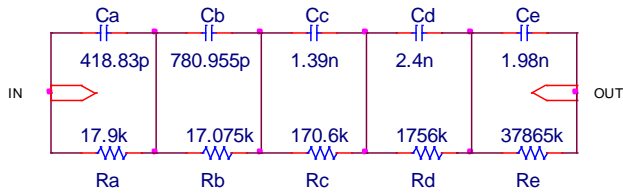


Figure 5 The electronic circuit of integrator for $q = 0.8$.

The circuit schematic of the integer-order Chen system for $a = 35$ is illustrated in Figure 6, with initial conditions $x(0) = 0$, $y(0) = 1$, and $z(0) = 0$.

Referring to Figure 6, the dimensionless equations of the system (2) can be expressed as follows:

$$\begin{aligned}
 RC_1 \frac{dv_x}{dt} &= \frac{Rv_y}{10R_2} - \frac{Rv_x}{R_1}, \\
 RC_2 \frac{dv_y}{dt} &= \frac{Rv_x}{R_4} - \frac{Rv_x v_z}{10R_5} + \frac{Rv_y}{R_3}, \\
 RC_3 \frac{dv_z}{dt} &= \frac{Rv_x v_y}{10R_6} - \frac{Rv_z}{R_7},
 \end{aligned} \tag{10}$$

where the component values are $C_{1,2,3} = 2.5\text{nF}$, $R_{1,2} = 11.4\text{k}\Omega$, $R_3 = 14.286\text{k}\Omega$, $R_4 = 51.14\text{k}\Omega$, $R_{5,6} = 4\text{k}\Omega$, $R_7 = 133\text{k}\Omega$, and $R_{8,9} = 10\text{k}\Omega$. RC is the time scale factor and is set to 1ms. DC voltage sources are also $V_p = -V_N = 15\text{V}$. The plot in Figure 7 displays the voltage values on the X, Y, and Z terminals in relation to one another.

As shown in Figure 8, the electronic circuit realization of the integer-order Chen system is constructed on a breadboard. When considered together with Figure 7, the oscilloscope outputs of the PSpice simulation and electronic circuit realization of the integer-order Chen system are similar.

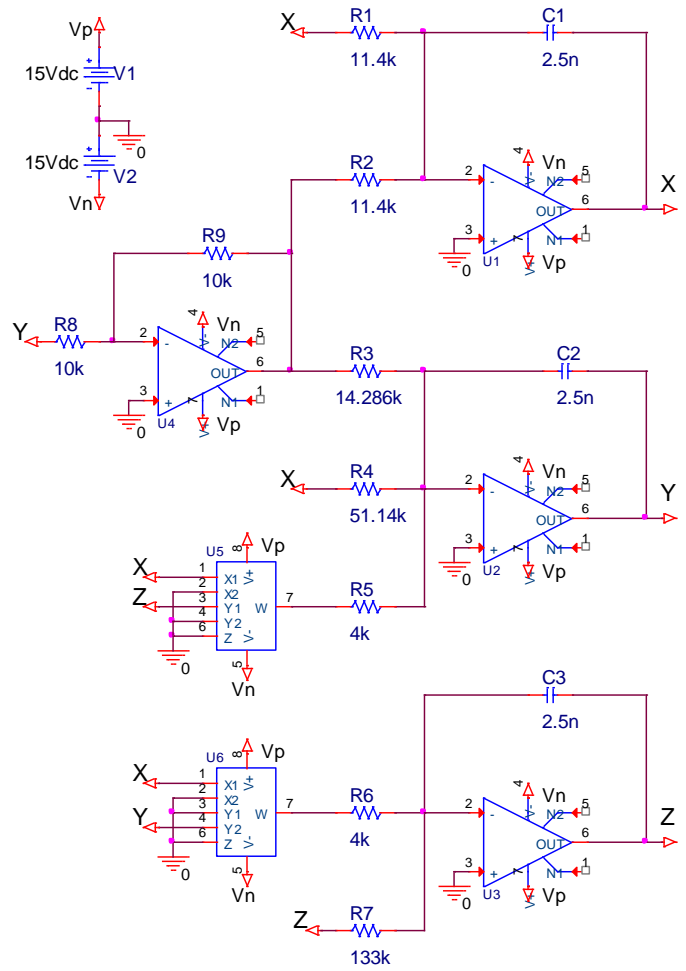


Figure 6 The circuit of the original Chen system (2) with linear scaling in PSpice program.

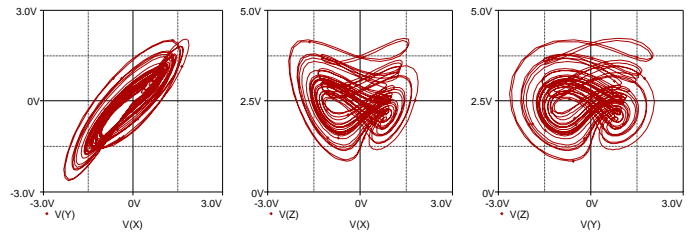


Figure 7 Phase portraits of integer-order Chen chaotic system in PSpice simulation.

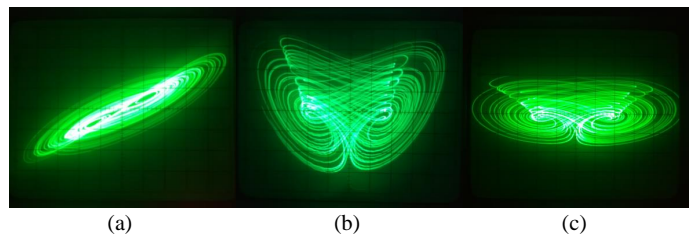


Figure 8 Integer-order Chen chaotic system's oscilloscope views: (a) $v_x(0.5\text{V/div})$ - $v_y(1\text{V/div})$, (b) $v_x(0.5\text{V/div})$ - $v_z(0.5\text{V/div})$, (c) $v_y(0.5\text{V/div})$ - $v_z(1\text{V/div})$.

The primary challenge in implementing an electronic circuit lies in modeling a fractional-order system using standard components. Considering Figure 3, it is observed that the suitable parameter values for $q = 0.8$ are $a = 30$, $b = 3$, and $c = 28$. The electronic circuit implementation of the FOCHEN system employing the chain fractances for $q = 0.8$ is shown in Figure 9.

The initial conditions are chosen as $x(0) = 0$, $y(0) = 1$, and $z(0) = 0$. Note that the fractional integral operator is transformed into a chain fractance with $N=5$. The circuits depicted in Figures 6 and 9 consist of passive and active circuit elements, including TL081 (operational amplifiers) and AD633 (multipliers), which are readily available in the market. Component values of the fractional-order electronic circuit are as follows: $C_{1,6,11} = 418.83\text{pF}$, $C_{2,7,12} = 780,955\text{pF}$, $C_{3,8,13} = 1.39\text{nF}$, $C_{4,9,14} = 2.4\text{nF}$, $C_{5,10,15} = 1.98\text{nF}$, $R_1 = 13.3\text{k}\Omega$, $R_2 = 13.3\text{k}\Omega$, $R_3 = 14.286\text{k}\Omega$, $R_{5,6} = 4\text{k}\Omega$, $R_7 = 133\text{k}\Omega$, $R_{8,9} = 10\text{k}\Omega$, $R_{10,15,20} = 17.9\text{k}\Omega$, $R_{11,16,21} = 17.075\text{k}\Omega$, $R_{12,17,22} = 170.6\text{k}\Omega$, $R_{13,18,23} = 1.756\text{M}\Omega$, $R_{14,19,24} = 37.865\text{M}\Omega$. The DC voltage sources are $V_p = -V_n = 15\text{V}$. The oscilloscope views of the voltages on the terminals (X, Y, and Z) of the FOCHEN system's electronic circuit, plotted against each other, are shown in Figure 10.

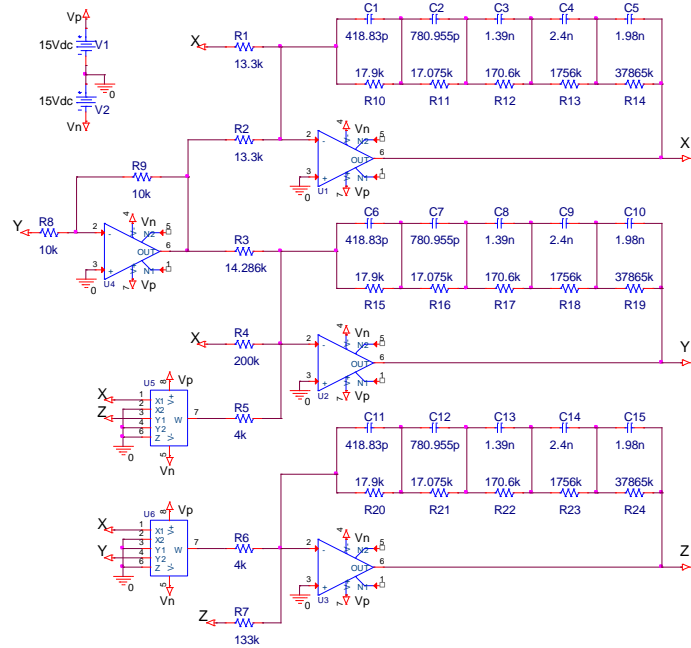


Figure 9 Circuit schematic of FOCHEN system for $q = 0.8$.

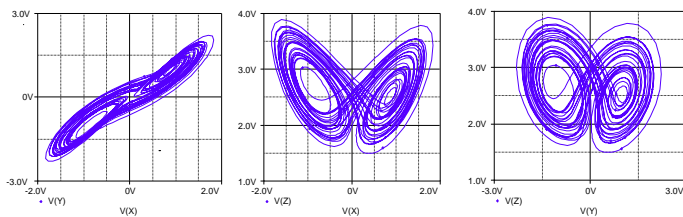


Figure 10 Phase planes of FOCHEN system in PSpice simulation for $q = 0.8$.

As presented in Figure 11, the electronic circuit realization of the FOCHEN system is constructed on a breadboard. When considered together with Figure 10, the oscilloscope views of PSpice

simulation and electronic circuit realization of the fractional-order system are very similar.

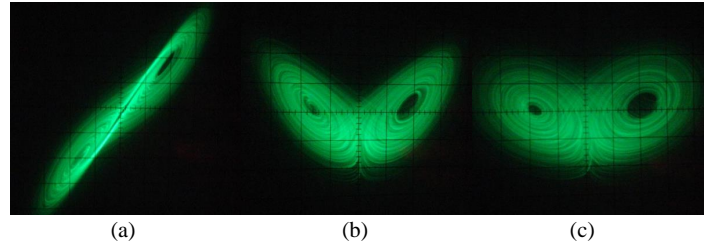


Figure 11 The FOCHEN system's oscilloscope views: (a) $v_x(0.5\text{V/div})-v_y(0.5\text{V/div})$, (b) $v_x(0.5\text{V/div})-v_z(0.5\text{V/div})$, (c) $v_y(0.5\text{V/div})-v_z(0.5\text{V/div})$.

Finally, it is observed that the results of PSpice simulations and electronic circuit implementations are consistent with the numerical analysis results conducted in the previous section. This confirms the applicability and consistency of the fractional-order modules. The electronic circuit of the FOCHEN system, along with the fractional-order modules, constructed on a breadboard, is shown in Figure 12.

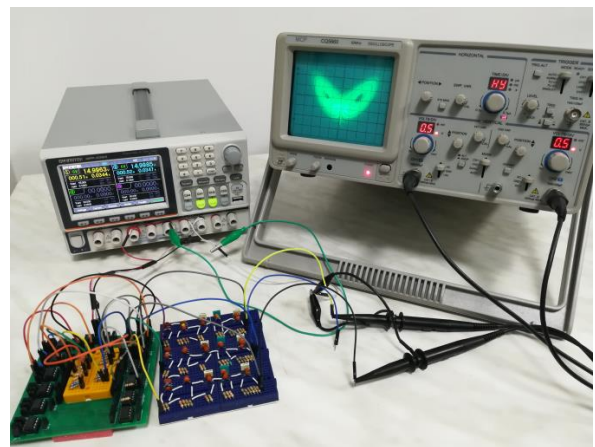


Figure 12 The electronic circuit of the FOCHEN system with the fractional-order modules.

CONCLUSION

Fractional-order analysis offers a means to enhance the diversity of dynamics in chaotic systems. This study presents an electronic circuit realization for the Chen system, incorporating a low-value fractional order and utilizing standard electronic components. The dynamic characteristics of the FOCHEN system are examined by conducting various analyses, such as phase portraits, Lyapunov spectra, and calculations of bifurcation diagrams. Additionally, the system's chaotic behavior for different fractional-order values is revealed through bifurcation diagrams and Lyapunov exponents analyses. Based on the numerical analyses and PSpice simulations, the minimum applicable fractional-order value (q) for the electronic circuit implementation of the FOCHEN system is found to be 0.8. The electronic circuit of the fractional-order system is constructed on a breadboard using discrete circuit elements, which are easily available in the market. The electronic circuit realization's voltage outputs, as observed in oscilloscope images, align with

numerical analyses and PSpice simulation program results. As a result, through fractional-order calculus, the dynamic diversity of the Chen system is enhanced. Thus, the FOCHEN system is a potentially chaotic system for use in data security applications where applicability and complexity are crucial. As expected, oscilloscope views of the electronic circuit realization align with the numerical analysis and PSpice simulation results.

Availability of data and material

Not applicable.

Conflicts of interest

The author declares that there is no conflict of interest regarding the publication of this paper.

LITERATURE CITED

- Ahmad, W. M. and J. C. Sprott, 2003 Chaos in fractional-order autonomous nonlinear systems. *Chaos, Solitons & Fractals* **16**: 339–351.
- Altun, K., 2021a Fpaa implementations of fractional-order chaotic systems. *Journal of Circuits, Systems and Computers* **30**: 2150271.
- Altun, K., 2021b Kesir dereceli sprott-k kaotik sisteminin dinamik analizi ve fpga uygulaması. *Avrupa Bilim ve Teknoloji Dergisi* pp. 392–399.
- Altun, K., 2022 Multi-scroll attractors with hyperchaotic behavior using fractional-order systems. *Journal of Circuits, Systems and Computers* **31**: 2250085.
- Chen, D., C. Wu, H. H. Iu, and X. Ma, 2013 Circuit simulation for synchronization of a fractional-order and integer-order chaotic system. *Nonlinear Dynamics* **73**: 1671–1686.
- Chen, G. and T. Ueta, 1999 Yet another chaotic attractor. *International Journal of Bifurcation and chaos* **9**: 1465–1466.
- Dang, H. G., 2014a Adaptive synchronization of the fractional-order sprott n system. *Advanced Materials Research* **850**: 872–875.
- Dang, H. G., 2014b Dynamics and synchronization of the fractional-order sprott e system. *Advanced Materials Research* **850**: 876–879.
- Du, M., Z. Wang, and H. Hu, 2013 Measuring memory with the order of fractional derivative. *Scientific reports* **3**: 3431.
- Garrappa, R., 2018 Numerical solution of fractional differential equations: A survey and a software tutorial. *Mathematics* **6**: 16.
- Gokyildirim, A., 2023 Circuit realization of the fractional-order sprott k chaotic system with standard components. *Fractal and Fractional* **7**: 470.
- Gokyildirim, A., H. Calgan, and M. Demirtas, 2023 Fractional-order sliding mode control of a 4d memristive chaotic system. *Journal of Vibration and Control* p. 10775463231166187.
- Hosny, K. M., S. T. Kamal, and M. M. Darwish, 2022 Novel encryption for color images using fractional-order hyperchaotic system. *Journal of Ambient Intelligence and Humanized Computing* **13**: 973–988.
- Li, C. and G. Peng, 2004 Chaos in chen's system with a fractional order. *Chaos, Solitons & Fractals* **22**: 443–450.
- Li, H., Y. Shen, Y. Han, J. Dong, and J. Li, 2023 Determining lya-punov exponents of fractional-order systems: A general method based on memory principle. *Chaos, Solitons & Fractals* **168**: 113167.
- Li, X., Z. Li, and Z. Wen, 2020 One-to-four-wing hyperchaotic fractional-order system and its circuit realization. *Circuit World* **46**: 107–115.
- Liu, T., H. Yan, S. Banerjee, and J. Mou, 2021 A fractional-order chaotic system with hidden attractor and self-excited attractor and its dsp implementation. *Chaos, Solitons & Fractals* **145**: 110791.
- Lu, J. G. and G. Chen, 2006 A note on the fractional-order chen system. *Chaos, Solitons & Fractals* **27**: 685–688.
- Nuñez-Perez, J.-C., V.-A. Adeyemi, Y. Sandoval-Ibarra, F.-J. Perez-Pinal, and E. Tlelo-Cuautle, 2021 Maximizing the chaotic behavior of fractional order chen system by evolutionary algorithms. *Mathematics* **9**: 1194.
- Özkaynak, F., V. Çelik, and A. B. Özer, 2017 A new s-box construction method based on the fractional-order chaotic chen system. *Signal, Image and Video Processing* **11**: 659–664.
- Pham, V.-T., S. T. Kingni, C. Volos, S. Jafari, and T. Kapitaniak, 2017 A simple three-dimensional fractional-order chaotic system without equilibrium: Dynamics, circuitry implementation, chaos control and synchronization. *AEU-international Journal of Electronics and Communications* **78**: 220–227.
- Podlubny, I., 1999 Fractional differential equations, mathematics in science and engineering.
- Silva-Juárez, A., E. Tlelo-Cuautle, L. G. De La Fraga, and R. Li, 2020 Fpaa-based implementation of fractional-order chaotic oscillators using first-order active filter blocks. *Journal of advanced research* **25**: 77–85.
- Sprott, J. C., 1994 Some simple chaotic flows. *Physical review E* **50**: R647.
- Tepljakov, A. and A. Tepljakov, 2017 Fomcon: fractional-order modeling and control toolbox. *Fractional-order modeling and control of dynamic systems* pp. 107–129.
- Valerio, D. and J. S. Da Costa, 2004 Ninteger: a non-integer control toolbox for matlab. *Proceedings of fractional differentiation and its applications, Bordeaux* .
- Wang, B., L. Li, and Y. Wang, 2020 An efficient nonstandard finite difference scheme for chaotic fractional-order chen system. *IEEE Access* **8**: 98410–98421.
- Wang, J., L. Xiao, K. Rajagopal, A. Akgul, S. Cicek, *et al.*, 2021 Fractional-order analysis of modified chua's circuit system with the smooth degree of 3 and its microcontroller-based implementation with analog circuit design. *Symmetry* **13**: 340.
- Yang, F. and X. Wang, 2021 Dynamic characteristic of a new fractional-order chaotic system based on the hopfield neural network and its digital circuit implementation. *Physica Scripta* **96**: 035218.
- Yao, J., K. Wang, P. Huang, L. Chen, and J. T. Machado, 2020 Analysis and implementation of fractional-order chaotic system with standard components. *Journal of Advanced Research* **25**: 97–109.
- Zouad, F., K. Kemih, and H. Hamiche, 2019 A new secure communication scheme using fractional order delayed chaotic system: design and electronics circuit simulation. *Analog Integrated Circuits and Signal Processing* **99**: 619–632.

How to cite this article: Gokyildirim, A. Dynamical Analysis and Electronic Circuit Implementation of Fractional-order Chen System. *Chaos Theory and Applications*, 5(2), 127-132, 2023.